Matter waves in reduced dimensions : dipolar-induced resonances and atomic artificial crystals

Nicola Bartolo

Collège Doctoral du Languedoc-Roussillon

THÈSE

Pour obtenir le grade de

Docteur

Délivré en *cotutelle* par

UNIVERSITÀ DI TRENTO

UNIVERSITÉ MONTPELLIER 2

Dottorato di Ricerca in **Fisica** – XXVII ciclo

Presso **INO-CNR BEC Center**

Préparée au sein de l'école doctorale **I2S**

Et de l'unité de recherche **Lab. C. Coulomb – UMR 5221**

Spécialité : **Physique**

Présentée par **Nicola BARTOLO**

Matter Waves in Reduced Dimensions:

Dipolar-Induced Resonances and Atomic Artificial Crystals

Ondes de Matière en Dimensions Réduites :

Resonances Dipolaires et Cristaux Atomiques Artificiels

Soutenue le 01/12/2014 devant le Jury composé de

M. Mauro ANTEZZA, Mcf. Univesité Montpellier 2	Directeur de Thèse
M. Stefano GIORGINI, Ass. Prof. Università di Trento	Directeur de Thèse
M. Brahim GUIZAL, Pr. Université Montpellier 2	Président
Mme Chiara MENOTTI, Cherch. Università di Trento	Co-Directeur de Thèse
M. Luis SANTOS, Full Prof. Universität Hannover	Rapporteur
Mme Patrizia VIGNOLO, Pr. Université Nice	Rapporteur

UNIVERSITÉ MONTPELLIER 2
SCIENCES ET TECHNIQUES

Abstract

The experimental achievement of Bose-Einstein condensation and Fermi degeneracy with ultracold gases boosted tremendous progresses both in theoretical methods and in the development of new experimental tools. Among them, intriguing possibilities have been opened by the implementation of optical lattices: periodic potentials for neutral atoms created by interfering laser beams. Degenerate gases in optical lattices can be forced in highly anisotropic traps, reducing the effective dimensionality of the system. From a fundamental point of view, the behavior of matter waves in reduced dimensions sheds light on the intimate properties of interparticle interactions. Furthermore, such reduced-dimensional systems can be engineered to quantum-simulate fascinating solid state systems, like bidimensional crystals, in a clean and controllable environment. Motivated by the exciting perspectives of this field, we devote this Thesis to the theoretical study of two systems where matter waves propagate in reduced dimensions.

The long-range and anisotropic character of the dipole-dipole interaction critically affects the behavior of dipolar quantum gases. The continuous experimental progresses in this flourishing field might lead very soon to the creation of degenerate dipolar gases in optical potentials. In the first part of this Thesis, we investigate the emergence of a single dipolar-induced resonance in the two-body scattering process in quasi-one dimensional geometries. We develop a two-channel approach to describe such a resonance in a highly elongated cigar-shaped harmonic trap, which approximates the single site of a quasi-one-dimensional optical lattice. At this stage, we develop a novel atom-dimer extended Bose-Hubbard model for dipolar bosons in this quasi-one-dimensional optical lattice. Hence we investigate the $T = 0$ phase diagram of the model by exact diagonalization of a small-sized system, highlighting the effects of the dipolar-induced resonance on the many-body behavior in the lattice.

In the second part of the Thesis, we present a general scheme to realize cold-atom quantum simulators of bidimensional atomic crystals, based on the possibility to independently trap two different atomic species. The first one constitutes a two-dimensional matter wave which interacts only with the atoms of the second species, deeply trapped around the nodes of a two-dimensional

optical lattice. By introducing a general analytic approach, we investigate the matter-wave transport properties. We propose some illustrative applications to both Bravais (square, triangular) and non-Bravais (graphene, kagomé) lattices, studying both ideal periodic systems and experimental-sized, eventually disordered, ones. The features of the artificial atomic crystal critically depend on the two-body interspecies interaction strength, which is shown to be widely tunable via 0D-2D mixed-dimensional resonances.

Keywords: matter waves, reduced dimensions, dipolar-induced resonances, mixed-dimensional resonances, extended Bose-Hubbard model, atomic artificial crystals.

Riassunto

La realizzazione sperimentale della condensazione di Bose-Einstein e della degenerazione di Fermi con gas ultrafreddi ha catalizzato enormi progressi sia nei metodi teorici sia nello sviluppo di nuove tecniche sperimentali. Tra queste, affascinanti prospettive nascono dall'implementazione di reticoli ottici: potenziali periodici per atomi neutri generati dall'interferenza tra raggi laser. Un gas degenere in un reticolo ottico può essere confinato in trappole fortemente anisotrope, sino a ridurne l'effettiva dimensionalità. Da un punto di vista fondamentale, il comportamento delle onde di materia in dimensioni ridotte fa luce sulle proprietà intrinseche delle interazioni tra particelle. Inoltre, questi sistemi a dimensionalità ridotta possono essere manipolati per creare simulatori quantistici della materia condensata, come ad esempio di cristalli bidimensionali, in un ambiente più precisamente controllabile. Motivati dalle appassionanti prospettive offerte da questo ambito, abbiamo dedicato questa Tesi allo studio teorico di due sistemi in cui delle onde di materia si propagano in dimensionalità ridotte.

Il carattere a lungo range e anisotropo dell'interazione dipolo-dipolo ha un forte impatto sul comportamento dei gas quantistici dipolari. Gli incessanti progressi sperimentali in questo fiorente ambito rendono plausibile l'imminente realizzazione di gas dipolari degeneri in potenziali ottici. Nella prima parte di questa Tesi analizziamo l'insorgenza di una singola risonanza dipolare nell'interazione tra due corpi in geometrie quasi unidimensionali. Sviluppando un approccio a due canali, descriviamo questa risonanza in una trappola armonica "a sigaro" fortemente allungata, che approssima un singolo sito di un reticolo ottico quasi unidimensionale. A questo punto sviluppiamo un nuovo modello esteso di Bose-Hubbard atomo-dimero, valido per bosoni dipolari in questo reticolo ottico quasi unidimensionale. Studiamo, quindi, il diagramma di fase del modello per $T = 0$ tramite diagonalizzazione esatta per un sistema di piccole dimensioni, sottolineando gli effetti della risonanza dipolare sulla fisica a molti corpi del reticolo.

Nella seconda parte della Tesi, presentiamo uno schema generale per la realizzazione di simulatori quantistici di cristalli bidimensionali con atomi freddi, basato sulla possibilità di intrappolare indipendentemente differenti specie atomiche. La prima forma un'onda di materia bidimensionale

che interagisce esclusivamente con gli atomi della seconda specie, fortemente intrappolati intorno ai nodi di un reticolo ottico bidimensionale. Introducendo un approccio analitico del tutto generale, studiamo le proprietà di trasporto dell'onda di materia. Proponiamo alcuni esempi di applicazioni sia a reticoli di Bravais (quadrato e rettangolare) che di non-Bravais (grafene e kagomé), analizzando sia sistemi periodici ideali sia sistemi sperimentalmente realistici, eventualmente affetti da disordine. Le caratteristiche di un cristallo atomico artificiale dipendono in maniera critica dall'interazione inter-specie a due corpi, che mostriamo essere manipolabile tramite risonanze a dimensionalità mista di carattere 0D-2D.

Parole chiave: onde di materia, dimensionalità ridotta, risonanze dipolari, risonanze a dimensionalità mista, modello esteso di Bose-Hubbard, cristalli atomici artificiali.

Résumé

La réalisation de condensats de Bose-Einstein et de gaz de Fermi dégénérés ont déclenché d'énormes progrès dans les méthodes théoriques ainsi que dans la mise en place de nouvelles techniques expérimentales. Parmi celle-ci, de fascinantes possibilités viennent de l'implémentation de réseaux optiques : potentiels périodiques pour atomes neutres créés à travers l'interférence de rayons laser. Un gaz dégénéré dans un réseau optique peut être forcé dans des pièges fortement anisotropes, jusqu'à réduire la dimensionalité du système physique. Du point de vue fondamental, le comportement des ondes de matière en dimensions réduites éclaircit les propriétés intrinsèques des interactions entre particules. En outre, ces systèmes à dimensionalité réduite peuvent être manipulés afin de créer des simulateurs quantiques de la matière condensée, comme par exemple des réseaux à deux dimensions, dans un environnement pur et contrôlable. Motivé par les passionnantes perspectives de ce domaine, on a consacré cette Thèse à l'étude théorique de deux systèmes dans lesquels une onde de matière se propage en dimensions réduites.

L'interaction dipôle-dipôle, à longue portée et anisotrope, affecte fortement le comportement des gaz quantiques. Les progrès expérimentaux dans ce domaine florissant permettront bientôt de piéger dans des réseaux optiques un gaz dégénéré de dipôles. Dans la première partie de cette Thèse, on considère l'apparition d'une seule résonance dipolaire dans l'interaction entre deux particules pour différents systèmes quasi-unidimensionnels. On propose une approche à deux canaux qui décrit cette résonance dans un piège harmonique fortement allongé "en forme de cigare", qui représente l'approximation d'un site d'un réseau optique quasi-unidimensionnel. À ce stade on développe un nouveau modèle étendu de Bose-Hubbard atome-dimère, qui est valable pour des bosons dipolaires dans un réseau optique quasi-unidimensionnel. On étudie donc le diagramme de phase du modèle pour $T = 0$ par la diagonalisation exacte de systèmes de petite taille, en soulignant les effets de la résonance dipolaire sur la physique à plusieurs corps dans le réseau.

Dans la seconde partie de la Thèse, on propose un modèle pour réaliser des simulateurs quantiques de cristaux bidimensionnels avec des atomes froids, basé sur le piégeage indépendant de deux espèces atomiques. La première constitue une onde de matière bidimensionnelle qui inter-

agit exclusivement avec les atomes de la seconde espèce, piégés aux nœuds d'un réseau optique bidimensionnel. En introduisant une approche théorique générale, on examine les propriétés de transport de l'onde de matière. On propose des exemples d'application pour réseaux soit de Bravais (carré, triangulaire), soit de non-Bravais (graphène, kagomé), en étudiant soit des systèmes périodiques idéaux, soit des systèmes de taille expérimentale et désordonnés. Les caractéristiques d'un réseau atomique artificiel dépendent de l'intensité de l'interaction entre les deux espèces, qu'on montre être largement réglable grâce à des résonances à dimensionalité mixte de type 0D-2D.

Mots clés : ondes de matière, dimensionalité réduite, résonances dipolaires, résonances à dimensionalité mixte, model étendu de Bose-Hubbard, cristaux atomiques artificiels.

Acknowledgments
Ringraziamenti
Remerciements

Montpellier, December 9th, 2014

Before illustrating the scientific results of my work, I think it is worth, more than owed, to acknowledge the important role of those who marked this three-year-long road named PhD, which represented a path of undeniable professional and personal growth.

Let me start by thanking those who, by sharing with me their expertise, made it possible to realize this work. I thank my supervisors Chiara Menotti and Mauro Antezza. They constantly encouraged me, from my first steps into the world of cold gases to the defense of this Thesis. They helped me in recognizing, training and developing my own research abilities, overtaking the obstacles due to my geographical delocalization. I also thank Alessio Recati, important source of fruitful advice and scientific discussions.

I wish to thank Stefano Giorgini, Brahim Guizal, Luis Santos, and Patrizia Vignolo for their careful reading of this manuscript, for their precious comments and for their kind appreciations on the work I realized during the last three years.

I thank David Papoular for the intense teamwork we carried on in Trento. I thank Diego Dalvit who in the delicate transition from Master to PhD student first addressed me to this joint Italian-French program, encouraging and supporting my application. A general but not less significant thank goes to all the members of the BEC Center in Trento and to those of the équipe PEPS of the L2C in Montpellier, who assured a stimulating and enjoyable environment for the advancement of my PhD.

Please, allow me a small digression in Italian.

Ringrazio di cuore i miei genitori, che sono rimasti incondizionatamente al mio fianco lungo qualunque mio cammino, professionale e personale. Ringrazio anche mia sorella, inestimabile fonte di conforto, distrazione e risate.

Un sentito ringraziamento a coloro che non cessano di incoraggiarmi con un affetto immutato dallo spazio e dal tempo. Grazie alle mie nonne ed i miei zii. Ringrazio con profondo affetto le mie incrollabili amiche Francesca e Simona, compagne in questo viaggio a tratti accidentato.

Before concluding, some words also in French.

Déménager en France a été pour moi un pari vraiment risqué. Il y a presque deux ans, je suis parti vers un pays dans lequel s'adapter est réputé être difficile, surtout en connaissant à peine la langue de Molière. Au bout de cette expérience je peux dire que la France a été une des meilleures découvertes de ma Thèse.

Si ça a été le cas, c'est grâce aux amis français qui ont croisé mon chemin à Montpellier. Merci à Riccardo, élément fondamental de cette expérience française. Conseiller de confiance, copain macaronier, prof de français, bref, un véritable nouvel ami.

Un merci spécial à toi, Yann, qui armé de patience as accueilli cet italien dans ta vie.

To be brief, thanks also to the many others that made this experience valuable. Friends and colleagues met in Trento, in Montpelier or in the wonderful places I had the chance to visit during these years of study, schools, workshops and amusements.

In summary, there have been people I brought with me on this path, people who shepherd me, people I will hopefully come across again, people I met that I intend to keep by my side along the upcoming portions of road. All of them paved in a different but fundamental way this path. All of them deserve my authentic gratitude.

Many thanks, Grazie mille, Merci beaucoup

Contents

List of Acronyms

0D ..... zero-dimensional

1D ..... one-dimensional

2D ..... two-dimensional

3D ..... three-dimensional

AAC ..... atomic artificial crystal

AAG ..... atomic artificial graphene

AASL ..... atomic artificial square lattice

AATL ..... atomic artificial triangular lattice

BEC ..... Bose-Einstein condensate

BHM ..... Bose-Hubbard model

DDI ..... dipole-dipole interaction

DIR ..... dipolar-induced resonance

EBHM ..... extended Bose-Hubbard model

FBZ ..... first Brillouin zone

HI ..... Haldane insulator

MDW ..... mass density wave

MI ..... Mott insulator

MW ..... matter wave

OL ..... optical lattice

SF ..... superfluid

List of Publications

Publications on dipolar-induced resonances:

- N. Bartolo, D. J. Papoular, L. Barbiero, C. Menotti, and A. Recati,
  Dipolar-induced resonance for ultracold bosons in a quasi-one-dimensional optical lattice,
  Phys. Rev. A **88**, 023603 (2013).
- N. Bartolo, D. J. Papoular, A. Recati, and C. Menotti,
  A toy model for the dipolar-induced resonance in quasi-one-dimensional systems,
  arXiv:1410:2483 (2014), submitted to EPJ Special Topics, Levico BEC 2014.

Publications on atomic artificial crystals:

- N. Bartolo and M. Antezza,
  Matter waves in atomic artificial graphene, Europhys. Lett. **107**, 30006 (2014).
- N. Bartolo and M. Antezza,
  Matter waves in two-dimensional arbitrary atomic crystals,
  Phys. Rev. A **90**, 033617 (2014), selected for Phys. Rev. A - Kaleidoscope, Sep. 2014.
- N. Bartolo and M. Antezza,
  Scattering in mixed and reduced dimensions: 0D-2D, in preparation.

Publications on subjects not treated in this Thesis:

- N. Bartolo and R. Passante,
  Electromagnetic-field fluctuations near a dielectric-vacuum boundary and surface divergences in the ideal conductor limit, Phys. Rev. A **86**, 012122 (2012).
- N. Bartolo, S. Butera, M. Lattuca, R. Passante, L. Rizzuto, and S. Spagnolo,
  Vacuum Casimir energy densities and field divergences at boundaries, arXiv:1410:1492 (2014), submitted to J. Phys.: Condens. Matter, special issue on Casimir Physics.

Introduction

Different fields of modern physics overlap in the domain of condensed-matter physics. Quantum mechanics, statistical mechanics, and electromagnetism together contribute to the understanding of solid-state systems. Historically, the leading subject of condensed-matter physics has been the study of crystals. These are solid materials whose building block is a microscopic elementary cell, periodically repeated in space until reaching a macroscopic scale. In a natural crystal, a lattice of ions kept together by chemical bounds creates a periodic potential landscape in which a shared electronic cloud propagates. The ionic structure also scatters light, creating interference patterns in diffracted x-rays. The connection between the crystalline structure and the transport properties of charge carriers has been widely investigated, relating the macroscopic behavior of a material to the quantum behavior of its elementary constituents [1, 2]. In a real solid, several unavoidable factors concur with the lattice periodicity in determining its physical properties, such as defects in the crystalline structure, impurities and disorder. Shortly, condensed-matter systems are complex quantum objects. It is thus useful to follow Feynman's suggestion and look for a "quantum simulator": an easily controllable and manipulable system, able to reproduce the quantum behavior of the complex one [3]. Cold gases in tailored potentials turn out to be a good candidate to this aim. With them, one naturally obtains ideal systems, clean from impurities and disorder, which can be both introduced in a controllable way. Furthermore, the lattice constant is much larger than in real materials, being in the micrometer range, and allows to control and image the system up to the single-site level.

When a dilute gas is cooled down to few nK, the de Broglie wavelength associated to each of its particles becomes much larger than the average interparticle distance. Then, the quantum nature of the gas emerges in a series of intriguing phenomena. As predicted by Bose and Einstein in 1924 [4–6], a gas of bosons, below a critical temperature T_c, can behave as a macroscopic matter wave, made of a large number of atoms coherently participating in the same wave function: a Bose-Einstein condensate (BEC) [7]. Similarly, a cold gas of fermions reaches the quantum regime of filled Fermi sea, in which the Pauli exclusion principle plays a crucial role [8]. The first

realizations of BECs in 1995 [9–11] and the achievement of degeneracy with fermions in 1999 [12] are considered milestones of 20th-century physics. Since then the number of groundbreaking theories and experiments in the field of cold gases grew constantly. One of the reasons of this success is the versatility of cold gases. The properties of a quantum degenerate gas are, indeed, strongly connected to the way in which particles interact. Typically, as we recall in Chap. 1, the interatomic interactions can be modeled by a contact potential, whose strength turns out to be tunable through several experimental techniques, such as the application of an external magnetic field [13], or by changing the shape of the trapping potential [14–16].

A fundamental property of neutral atoms is their sensitivity to optical potentials. When immersed in the electromagnetic field, atoms get polarized and the Stark effect shifts their energy levels. A field-intensity gradient results in a force on the atoms [17]. Therefore, one can exploit the interference of counterpropagating laser beams to create a spatially modulated light pattern, an optical lattice, which results in a modulated potential energy landscape for the atoms. Within such a lattice, the atoms perceive a periodic potential, likewise electrons in a solid, and can be used to quantum simulate a solid-state system [18–20]. In this case, the interplay between lattice potential and interatomic interactions is modeled by effective Hamiltonians, able to predict, for instance, the occurrence of quantum phase transitions between insulating and superfluid phases [21–23], which have been experimentally detected [24]. To summarize the main features of matter waves and their behavior in optical lattices, we present a short and non-comprehensive review on the topic in Chap. 1. Briefly, the optical lattice can be modeled as an array of microtraps among which cold atoms can tunnel. Weakly-interacting particles get delocalized along the lattice and the ground state of the system is represented by a superfluid (SF) phase, in which atoms behave as a coherent matter wave in the lattice. Contact-interacting particles contribute to the system energy only when they occupy the same lattice site. Then, a strong interatomic repulsion can inhibit tunneling, since the system tends to avoid large number fluctuations at each lattice site. If the number of atoms and sites in the system is equal (unitary filling factor), this phase correspond to a Mott insulator (MI) in which there is exactly one atom per site. This scenario is enriched in the presence of long ranged interactions. In this case also atoms sitting in adjacent sites contribute to the energy, and new insulating phases with a density modulation different than the one of the optical lattice can arise. In the unitary-filling scenario, if the nearest-neighbor interaction dominates the on-site interaction, atoms prefer to multiply occupy a site and leave empty the nearest ones, ending up in a mass density wave (MDW) phase. While the different phases of the model can be pictured intuitively, advanced numerical techniques are required to provide exact phase diagrams. Moreover, the dependence of the model parameters on real physical quantities requires a detailed study of the lattice geometry and of the elementary two-body scattering process in the periodic potential.

The long range and anisotropic character of the dipole-dipole interaction [25, 26], together with the advances in the manipulation of dipolar particles [27–31], makes dipolar systems suitable to implement lattice Hamiltonians with nearest and further-neighbor interactions [32]. With this motivation, in Chap. 2 we investigate in detail the interplay between dipole-dipole interaction and trapping geometry in a one-dimensional (1D) array of elongated cigar-shaped traps, forming a quasi-1D optical lattice. We start by analyzing the two-body scattering at the single-site level, replacing the dipole-dipole interaction with an effective interaction for quasi-1D systems [33]. We point out the emergence of a single dipolar-indiced resonance (DIR) in a quasi-1D tube, which is a low-energy resonance occurring when the dipole strength is varied. The occurrence of the DIR in a cigar-shaped harmonic trap is demonstrated both by numerical investigations and by means of an analytically solvable toy-model potential [34]. The DIR is reproduced by a two-channel model [35], where the channels correspond to a bi-atomic state and a two-body bound state. In the lattice, this two-channel approach translates in a two-band model, which we introduce under the name of atom-dimer extended Bose-Hubbard model [35]. The $T = 0$ phase diagram of the system is then investigated, as a function of the optical lattice depth and of the dipole-dipole interaction strength, which are both tunable parameter in an experimental system. We point out the effects of the DIR on the phase diagram. In particular, SF, MI, and MDW phases appear in regions of the phase diagram different from those predicted in the absence of the DIR. Interestingly, we also predict the occurrence of a collapse phase for strong dipolar interactions in a geometry where two classical dipoles would just repel each other.

A central role in the condensed matter realm is entitled to two-dimensional (2D) materials. This branch received a significant boost in 2004, due to the experimental isolation of graphene [36]: a monolayer of carbon atoms arranged in a honeycomb lattice. In this material, conduction and valence bands touch in isolated points of k space, the Dirac points, around which the energy-momentum dispersion relation is conical and a Dirac-like equation for massless fermions replaces the Schrödinger equation to describe the quantum motion of the charge carriers [37, 38]. In parallel to the analysis on graphene and other 2D materials, a number of proposal for quantum simulators of 2D crystals flourished [39], among which the idea of using single-species matter waves in optical lattices. For an honeycomb lattice, the appearence of Dirac cones in the energy-momentum dispersion was expected, a phenomenon experimentally observed in 2012 [40].

Following these ideas, we introduce in Chap. 3 a new model for the realization of artificial bidimensional crystals of arbitrary geometry based on the use of two atomic species [41, 42]. In our proposal, a 2D matter wave made up of A atoms interacts only with point-like scatterers of the second atomic species, denoted by B, independently trapped around the nodes of a 2D optical lattice. Since the periodic potential felt by the matter wave is generated by atom-atom interactions, and not by an optical potential, we name this system atomic artificial crystal (AAC). The

experimental realization of our model relies on the use of species-selective optical lattices, that are trapping potentials engineered to act on one atomic species (B in the present case) being at the same time invisible to a second one (for us, A) [43, 44]. By tuning the $B-B$ interaction, one can reach the MI phase in the optical lattice, ending up with an artificial crystal with the lattice periodicity. With respect to one-species models, disorder can be naturally introduced in AACs: it appears in the form of randomly distributed empty sites if the lattice filling is lower than one. We investigate the crystal properties starting by a brief analysis of the elementary scattering process between an atom of the matter wave and a trapped scatterer, which amounts to a problem of scattering in reduced *and* mixed dimensions [45]. Then, we present a theoretical model for the entire AAC, valid for ideal periodic structures, as well as for finite-sized and disordered systems. Our approach allows to determine the Green's function of the matter wave and, hence, its transport properties. We specify the model to some paradigmatic cases, among which the atomic artificial graphene [41], discussing features and tunability of the AAC band structure, such as omnidirectional gaps, Dirac cones, and non-dispersive flat bands.

CHAPTER 1

Matter Waves in Optical Lattices

This first, introductive chapter is thought as a brief and non-comprehensive review of the physics of matter waves in optical lattices. The combination of cold gases and periodic potentials revealed as a powerful tool to quantum simulate condensed-matter systems in highly controllable models. A fundamental role is played by the coaction of inter-particle and optical potentials, respectively discussed in Secs. 1.2 and 1.3, which leads to the emergence of many-body quantum phase transitions. In Sec. 1.4, we consider how the external potential affects the two-body scattering properties when the applied trapping reduces the effective dimensionality of the matter wave. Finally, we resume in Sec. 1.5 some relevant features of the dipolar interaction, a long-ranged and anisotropic potential which allows to mimic more general Hamiltonians than those obtained by using contact-interacting particles.

Contents

1.1 Ultracold gases as waves of matter

After centuries devoted to the investigation of macroscopic phenomena, 20th-century physicists focused on the nature and behavior of the elementary constituents of matter. The Bohr model for electrons' orbits in hydrogen atoms and Eistein's conjectures on the photoelectric effect showed that something was missing in the classical distinction between particles and waves. The gap was filled in 1924 by Louis de Broglie, that postulated in his Thesis the wave-particle duality [46]. Nowadays we know that a light wave of angular frequency ω transports energy in "packets" of $\hbar\omega$, $\hbar$ being the Planck's constant on 2π, and that a particle with momentum modulus p has an associated wavelength $\lambda_{\mathrm{dB}} = 2\pi\hbar/p$, known as de Broglie wavelength. But when does the wave nature of particles emerge? If one considers a gas at temperature T, from the Maxwell-Boltzmann distribution one gets that the average momentum of one particle is $\langle p\rangle \simeq \sqrt{mk_{\mathrm{B}}T}$, where m is the particle mass and k_{B} the Boltzmann constant. At room temperature, λ_{dB} is smaller than the atomic radius, so that the particles of an everyday gas do not act as quantum objects, but rather as billiard balls. Fortunately, the technological advances of the last decades allowed to develop experimental techniques which permit to reach temperatures down to few nK, at which λ_{dB} is not only larger that the particle radius, but also exceeds the average inter-particle distance.

The low-temperature behavior of bosons, particles with integer spin, was theoretically investigated in 1924 by Bose and Einstein [4, 5]. They predicted a low-temperature phase transition for noninteracting particles, the so-called Bose-Einstein condensation, in which all the bosons condense in the ground state of the system, sharing the same wave function and behaving as a coherent matter wave. The first experimental observations of this new phase of matter were realized in 1995 for dilute clouds of alkali atoms [9–11]. Fermions, particles with half-integer spin, cannot occupy the same quantum state due to Pauli exclusion principle. Hence, a quantum degenerate Fermi gas consists of N particles occupying the N lowest energy eigenstates of the system, a phase achieved by several experimental groups starting from 1999 [12, 47, 48].

Interactions are crucial in determining properties and stability of quantum-degenerate systems. A Bose gas, for instance, collapses if the particles attract each other, while strongly-interacting bosons can behave as impenetrable particles and act as fermions in low-dimensional systems. On the other hand, interacting fermions can build-up "pairs" and condense as composite bosons. Due to the fundamental role of interactions, we dedicate Sec. 1.2 to the analysis of the two-body scattering process between cold particles. In particular, in Sec. 1.2.1, we describe how isotropic, short-ranged interactions can be replaced by an effective contact potential, ruled by a single parameter: the s-wave scattering length. Remarkably, strength and sign of the contact potential can be experimentally adjusted in cold atomic system, through the mechanism of Feshbach resonances, discussed in Sec. 1.2.2.

The interaction between an induced dipole moment and an external electric field is the basic mechanism allowing to store ultracold quantum gases in artificial periodic potentials of light: the optical lattices [17]. As discussed in Sec. 1.3, this possibility paved the way to innovative control and manipulation techniques, earning to matter waves in optical lattices the title of quantum simulators of solid-state systems [18–20]. The interplay between lattice potential and interatomic interactions is modeled by effective Hamiltonians, able to predict the occurrence of quantum phase transitions. Furthermore, optical potentials allow to strongly confine cold gases in thin pancake- or cigar-shaped traps, making it possible to achieve of low-dimensional systems where new quantum phases can emerge. An overview on the scattering process in this kind of geometries is presented in Sec. 1.4.

Finally, more general Hamiltonians can be mimicked by resorting to interatomic potentials going beyond the contact approximation. In this direction a leading role is played by the dipolar interaction, which, as presented in Sec. 1.5, manifests both long-range and anisotropic character. The experimental realization of BECs of magnetic dipoles [27–29] and the recent progresses with the association of heteronuclear molecules [30, 31], boosted both theoretical and experimental investigations in this direction.

1.2 Two-body scattering of ultracold particles

The behavior and the experimental realization of ultracold quantum gases are strictly related to the way in which their elementary constituents interact between each other. Typically, the interatomic potential is isotropic and short ranged and, as we will see in Sec. 1.2.1, this allows to replace it with a contact pseudopotential, whose strength and sign depend on the *s*-wave scattering length a_{3D}. A Bose-Einstein condensate (BEC) counting a large number of atoms is stable only in the presence of interparticle repulsion. Instead, a condensate of attractive bosons collapses if the number of particles exceeds a critical threshold [49]. Pauli exclusion principle prevents two fermions in the same spin state to undergo *s*-wave scattering. However, if different internal states coexist, by tuning a_{3D} one can explore the crossover from a BEC of composite molecules to a superfluid of weakly-bound Cooper pairs, described by the Bardeen-Cooper-Schrieffer theory of superfluidity [50]. Thanks to the mechanism of Feshbach resonances, described in Sec. 1.2.2, a_{3D} actually becomes an experimental knob, adjustable via an external magnetic field.

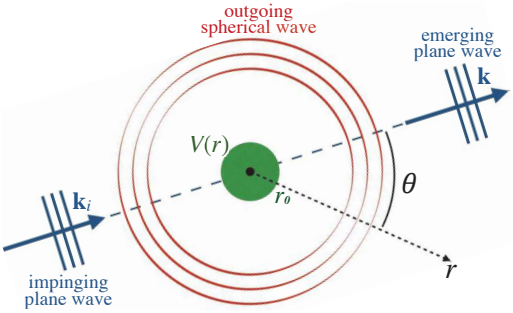

Figure 1.1 : Schematic of the three dimensional scattering from a central potential $V(r)$. In the relative coordinate frame an impinging plane wave of wave vector $\mathbf{k}_i$ enters in the region $|r| < r_0$ in which the central potential $V(r)$ is considerable. After the scattering process, and far from the scattering center, the wave function is the superposition of an emerging plane wave of wave vector $\mathbf{k}$ plus an outgoing spherical wave, whose amplitude is modulated in space depending on θ, the angle between $\mathbf{k}$ and the detection direction.

1.2.1 Contact pseudopotential for 3D scattering

Let us consider the elementary problem of two particles of mass m_1 and m_2 in a three-dimensional space, interacting via a relative potential $V(\mathbf{r}_1 - \mathbf{r}_2)$, where $\mathbf{r}_1$ and $\mathbf{r}_2$ are the particles' positions. In a wide range of circumstances the interaction is isotropic, so that the potential only depends on the relative distance $r = |\mathbf{r}_1 - \mathbf{r}_2|$. Usually, $V(r)$ decays fast with r, manifesting a finite-range character and being relevant only within a region of radius r_0. A well-known example violating these properties is given by the dipolar interaction, which will be extensively treated in Sec. 1.5. The solution of the two-body scattering problem for $V(r)$ comes from the relative-motion Schrödinger equation

$$\left[V(r) - \frac{\hbar^2}{2\mu}\nabla^2_{\mathbf{r}}\right]\Psi(\mathbf{r}) = E\Psi(\mathbf{r}), \tag{1.2.1}$$

in which we introduced the reduced mass $\mu = m_1 m_2/(m_1+m_2)$ and the relative coordinate $\mathbf{r} = \mathbf{r}_1 - \mathbf{r}_2$. In this frame of reference an incoming wave packet of wave vector $\mathbf{k}$ is scattered by the central potential $V(r)$, as schematically represented in Fig. 1.1. Far from the collision center, i.e. for $r \gg r_0$, the wave function takes the asymptotic form [51]

$$\Psi(\mathbf{r}) \propto e^{i\mathbf{k}\cdot\mathbf{r}} + f_{3D}(k,\theta)\frac{e^{ikr}}{r}, \tag{1.2.2}$$

that is, the superposition of an emerging plane wave of wave vector $\mathbf{k}$ plus an outgoing spherical wave, modulated by the 3D scattering amplitude f_{3D}. For low scattering energies, this amplitude takes the simple, θ-independent form

$$f_{3D} = \frac{1}{-1/a_{3D} + r_e k^2/2 - ik} \xrightarrow{k\to 0} -a_{3D} \tag{1.2.3}$$

where the parameter r_e is the effective interaction range, while a_{3D} is the s-wave scattering length for the three-dimensional system. The predominance of s-wave scattering at low temperatures appears from a proper rewriting of Eq. (1.2.1). Being $V(r)$ a central potential, the wave function Ψ can be factorized in its radial and angular contributions as $\Psi(\mathbf{r}) = \psi_\ell(r)Y^{\mathrm{m}}_\ell(\theta,\phi)$, where Y^{m}_ℓ is a

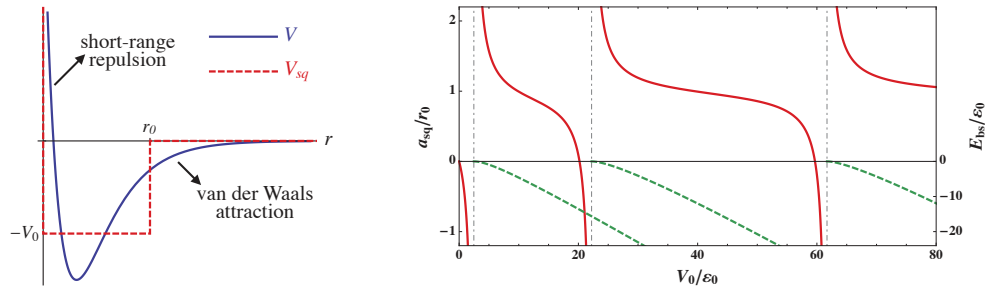

Figure 1.2 : Left: Sketch of the interaction potential V between two neutral atoms [solid (blue) curve]. The repulsive core interaction competes with the long-range attractive van der Waals potential, forming a potential well. The main features of V are caught by the square potential V_{sq} [dashed (red) line]. Right: 3D s-wave scattering length a_{3D} [solid (red)] and bound state energies E_{bs} [dashed (green)] for the potential V_{sq} introduced in the left panel. A divergence in a_{3D} occurs each time a new bound state is allowed in the system, i.e., when the resonant condition $E_{bs}=0$ is fulfilled. The unit of energy is $\varepsilon_0=\hbar^2/2\mu r_0$, μ being the reduced mass of the two-body system.

spherical harmonic with ℓ and m the angular momentum quantum numbers. The resulting radial equation is

$$\left[V(r)+\frac{\hbar^2\ell(\ell+1)}{2\mu r^2}-\frac{\hbar^2}{2\mu}\left(\frac{\partial^2}{\partial r^2}+\frac{2}{r}\frac{\partial}{\partial r}\right)\right]\psi_\ell(r)=E\psi_\ell(r). \tag{1.2.4}$$

For $\ell\neq 0$ a contribution $\propto 1/r^2$ adds to $V(r)$, forming a centrifugal barrier. Its height, converted in temperature, is typically of the order of 1mK so that in the micro- and nano-K regime the barrier freezes out the scattering in $\ell>0$ states. This approximation fails only in some special cases in which, beyond the centrifugal barrier, there exists a bound state resonant with the scattering energy, situations in which a so-called shape resonance occurs [52]. The value of the scattering length a_{3D} for a given potential $V(r)$ can be deduced by solving Eq. (1.2.4) for $\ell=0$ and $k\to 0$. From Eqs. (1.2.2) and (1.2.3) it follows that the asymptotic behavior of this zero-energy s-wave solution takes the simple form

$$\psi_s(r)\propto 1-\frac{a_{3D}}{r}, \tag{1.2.5}$$

from which a_{3D} is immediately defined. The low-k behavior of the scattering amplitude $f(k)=-(ik+1/a_{3D})^{-1}$ is exactly reproduced by the regularized contact pseudopotential

$$V_c^{3D}(r)\cdots=\frac{2\pi\hbar^2}{\mu}\,a_{3D}\,\delta(r)\,\frac{\partial}{\partial r}(r\cdots). \tag{1.2.6}$$

This means that, for low-energy scattering, one is allowed to replace the real potential $V(r)$ by the contact potential $V_{3D}(r)$. A useful quantity is the 3D coupling constant of the pseudopotential $g_{3D}=2\pi\hbar^2 a_{3D}/\mu$, which measures the strength of the regularized δ.

In order to predict the value of the s-wave scattering length for two cold particles, the knowledge of the relative potential $V(r)$ is of fundamental importance. Generally, two distant neutral

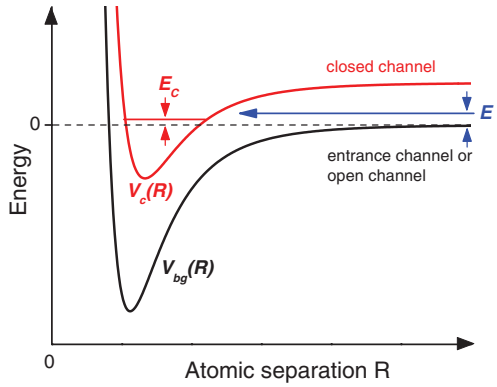

Figure 1.3 : Representation of the two-channel model for the Feshbach resonance. Two particles scatter with energy E in the open channel, characterized by the potential V_{bg}. Another scattering channel, corresponding, for instance, to a different spin configuration of the incoming particles, constitutes the closed channel. The corresponding interaction potential V_c admits a bound state of energy E_c. For $E \sim E_c$ the scattering cross section in the open channel is resonantly enhanced. Figure from [13].

particles attract each other via the van der Waals potential $V_{\mathrm{vdW}}(r) = -C_6/r^6$, for which the coefficient C_6 defines the characteristic length $a_c = (2\mu C_6/\hbar)^{1/4}$. For alkali atoms a_c is typically of the order of some nanometers [19]. When particles get extremely close, the short-range interaction prevails on V_{vdW}, resulting in a strong repulsion. A qualitative sketch of the inter-particle potential is presented in Fig. 1.2 (left), showing how the competition of short-range repulsion and long-range attraction gives rise to a potential well, which can support several bound states. To get a feeling of their fundamental role in determining $a_{3\mathrm{D}}$, one can consider the instructive toy potential V_{sq} shown in Fig. 1.2 (left): the long-range attraction is mimicked by a square well of depth V_0 for $|r| < r_0$, while the short-range repulsion is taken into account by a hard-wall in $r = 0$. For such a potential, Eq. (1.2.4) can be solved analytically, determining both a_{sq} and the energy of the bound states E_{bs}. Their behavior is shown in Fig. 1.2 (right) for increasing values of the well depth V_0. A series of resonances occurs in the scattering amplitude, which oscillates from $-\infty$ to $+\infty$. Even if V_{sq} has a deep attractive well, the corresponding pseudopotential (1.2.6) spans all the regimes from no interaction to strong attraction and repulsion. In particular the scattering amplitude a_{sq} diverges each time a new bound state is allowed in the system, i.e. when E_{bs} is resonant with zero. The behavior of $a_{3\mathrm{D}}$ for the real interatomic potential $V(r)$ [Fig. 1.2 (left)] is qualitatively the same. More refined toy models, like the one presented in [53], show that, far from the resonances, the lengthscale of $a_{3\mathrm{D}}$ is typically a_c, but an *ab initio* calculation of its exact value requires the knowledge of the short-range behavior. For this reason such calculations are a vary hard theoretical task. However, in many cases, the scattering length $a_{3\mathrm{D}}$ for a given pair of atomic states, determined experimentally, shows a remarkable agreement with the theoretical predictions [54].

1.2.2 Tuning the contact interaction: Feshbach resonances

The value of $a_{3\mathrm{D}}$ strongly affects the physics of an ultracold gas and it is interesting to find a way to tune experimentally its value. The simple example of V_{sq} (cf. Fig. 1.2) shows how, by

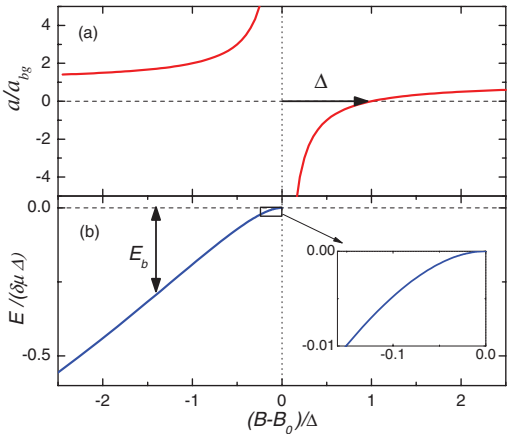

Figure 1.4 : Top: Scattering length a_{3D} as a function of the magnetic field in a Feshbach resonance, as presented in Eq. (1.2.7). The resonance occurs for $B = B_0$ and has width Δ. Bottom: Molecular state energy near the resonance. The behavior of E_b is linear far from B_0 and gets quadratic close to the resonance (region magnified in the inset). $\delta\mu$ is the difference in magnetic moment between open and closed channel. Figure from [13].

changing the shape of the potential, one can induce resonances in a_{3D}. Unfortunately, once the atomic species in play are fixed, their reciprocal scattering potential is in turn assigned and cannot be modified. On the other hand, in order to tune a_{3D} one can take advantage of the existence of different channels for the scattering process. This idea was introduced independently by Feshbach [55, 56] and Fano [57], respectively in the context of nuclear and atomic physics. The origin of the Fano-Feshbach resonance, or more commonly just Feshbach resonance, can be deduced by the simple picture depicted in Fig. 1.3. The actual scattering process takes place in the background channel, corresponding to the ground state spin configuration of the incoming particles. From $V_{bg}(r)$ one gets the background scattering length a_{bg}. If particles are in a different spin configuration they feel a different relative potential $V_c(r)$, which we assume admitting a bound state of energy E_c. Such a channel is commonly referred to as the closed one. If the scattering energy E is far from E_c, the existence of the closed channel is unperceived by the particles, so that $a_{3D} = a_{bg}$. But, if $E \sim E_c$, even a small coupling between the channels would result in a strong amplification of the scattering length, being the closed-channel bound state resonant with the scattering energy. The key to the experimental tuning of a_{3D} is that, having the two spin configurations different magnetic moments, the relative distance between the channels can be adjusted by a static magnetic field.

By tuning the applied magnetic field B, E_c crosses zero and, correspondingly, the scattering length diverges, similarly to the case of the square potential depicted in Fig. 1.2. A simple expression for the s-wave scattering length as a function of the applied field B has been introduced in [58]:

$$a_{3D}(B) = a_{bg}\left(1 - \frac{\Delta}{B - B_0}\right), \tag{1.2.7}$$

and its behavior is plotted in Fig. 1.4, together with the dependence on B of the binding energy E_b of the dimer state associated to the resonance. The value B_0 indicates the point at which the

resonance occurs, while Δ sets its width, a widely varying parameter which in average remains around 1G. For $B = B_0 + \Delta$ one finds $a_{3D} = 0$, i.e. the ideal limit of noninteraction. Far from B_0 the scattering length tends to its background value a_{bg}. The energy of the weakly bound state E_b is linear in the magnetic field, with a slope fixed by the difference in magnetic moment $\delta\mu$ between open and closed channel. Close to the resonance, the strong coupling between the two channels changes this linear into a quadratic behavior, with the typical dependence $E_b = -\hbar^2/2\mu a_{3D}^2$ (cf inset of Fig. 1.4). Note that both Δ and a_{bg} can be positive or negative. Since their first observation in a BEC [59], Feshbach resonances became a fundamental tool in cold-atoms experiments, allowing not only to set the interaction regime but also to dynamically change it during the experiment. For instance, when a resonance is adiabatically crossed from the negative- to the positive-a_{3D} side, the two separate atoms can be driven into the dimer state [13]. Feshbach resonances can be similarly obtained by optically coupling the open and closed channel [60, 61]. However, this method, although in principle more flexible, suffers of heating issues which makes it less suitable than the magnetic mechanism in cold-atoms experiments.

1.3 Many-body physics in optical lattices

A versatile and useful technique to trap cold atoms relies on the possibility of trapping neutral atoms with laser light. Exploiting the interference of different beams, it is possible to create a periodic light-induced potential, known as optical lattice (OL). These light potentials were originally conceived as convenient tools in the cooling of cold gases [62, 63]. Nevertheless, since their first realizations in the early '90s [64, 65], they turned out to be a useful tool to trap and study particles in periodic potentials. In the last years, the investigation of propagation of matter waves in ideal periodic, quasi-periodic, and disordered optical potentials has allowed to create a close link between cold atoms and solid-state physics [19].

In this section we review the origin and versatility of optical potentials, stressing the possibility to mimic condensed-matter systems by loading cold atoms in optical lattices (Sec. 1.3.1). Then, we introduce in Sec. 1.3.2 the Hamiltonian describing a system of contact-interacting bosons in a periodic potential: the Bose-Hubbard model. We point out the quantum phases of such a system, together with their experimental detection. Finally, we consider how the scenario is modified when the interparticle interaction is long-ranged, intoducing and discussing the extended Bose-Hubbard model in Sec. 1.3.3.

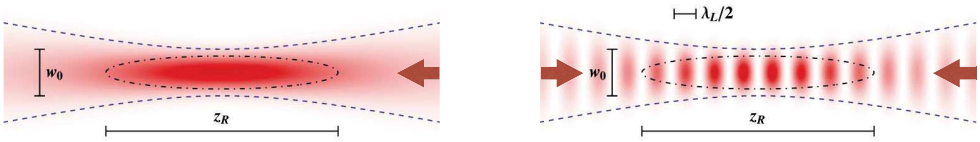

Figure 1.5 : Left: Schematics of a Gaussian-beam optical potential of central width w_0 and Rayleigh length z_R. For a beam red-detuned to the closest atomic transition, the optical potential creates a quasi-harmonic trapping around the beam focal point, in the region enclosed by the dot-dashed (black) line. Right: Same as left, but for two counterpropagating beams of wavelength λ_L. The interference light pattern results in a periodic optical potential along the lasers axis. This is the simplest configuration for a one-dimensional optical lattice. Atoms are trapped in a linear array of pancake-shaped micro trap. Lengths are in arbitrary units.

1.3.1 Origin and features of optical potentials

Under the action of an electric field the atoms develop an induced electric dipole moment proportional to the field intensity [66]. When immersed in a laser beam of frequency ω_L, an atom gets polarized by the electric component of radiation. The optical potential

$$V_o = -\frac{1}{2}\alpha(\omega_L)|\mathbf{E}(\mathbf{r})|^2 \tag{1.3.1}$$

arises from the interaction of the induced dipole with the polarizing field itself [17, 67]. The direction of the optical force crucially depends on the sign of the atomic polarizability $\alpha(\omega_L)$. In the vicinity of an atomic transition between a ground state $|g\rangle$ and an excited state $|e\rangle$, with $E_e - E_g = \hbar\omega_{eg}$, one can approximate

$$\alpha(\omega_L) \sim \frac{|\langle e|\hat{d}_{\mathbf{E}}|g\rangle|^2}{\hbar(\omega_{eg} - \omega_L)}, \tag{1.3.2}$$

being $\hat{d}_{\mathbf{E}}$ the dipole operator in the field direction. Since the intensity of the light field $I(\mathbf{r}) \propto |\mathbf{E}(\mathbf{r})|^2$, it follows that atoms are attracted at the intensity maxima if the laser light is red-detuned with respect to the atomic transition (i.e., $\omega_L < \omega_{eg}$), while they move towards intensity minima for blue-detuned beams (i.e., $\omega_L > \omega_{eg}$).

A stand-alone Gaussian beam is already sufficient to generate a trapping potential. In polar coordinates around its propagation axis z, its intensity profile is

$$I(\rho, z) \propto \frac{w_0^2}{w^2(z)}\, e^{-\frac{2\rho^2}{w^2(z)}}, \tag{1.3.3}$$

where the function $w(z) = w_0\sqrt{1 + z^2/z_R^2}$ accounts for the beam divergence far from its focal plane $z = 0$. Typically, the central beam waist $w_0 \sim 100\mu$m, while the Rayleigth length $z_R = \pi w_0^2/\lambda_L$ is in the millimeter or centimeter range. For a red-detuned beam, the optical potential (1.3.1) creates

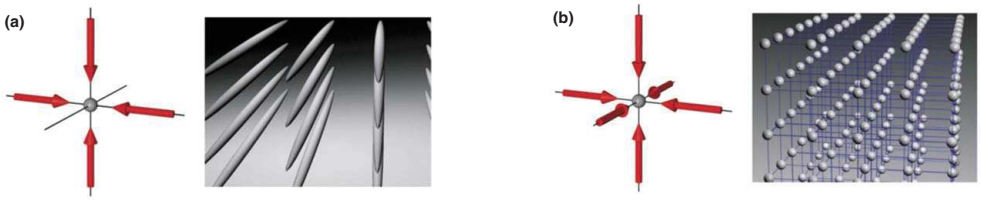

Figure 1.6 : (a) Two- and (b) three-dimensional optical lattices, obtained by superimposing two or three pairs of counterpropagating laser beams. In (a), atoms are confined along quasi-one-dimensional tubes. Figure from [19]

an attractive well along the beam axis and around its focal point, as represented in Fig. 1.5 (left). The realization of periodic potentials naturally comes by exploiting the interference of counter-propagating laser beams. If two equally polarized Gaussian beams of wavelength λ_L interfere, the resulting light intensity presents an interference pattern. Consequently, the optical potential is periodically modulated in space and, in the vicinity of the focal plane, it takes the form

$$V_{\mathrm{OL}}^{\mathrm{1D}} = -V_0 \sin^2(2\pi z/\lambda_L)\, e^{-\frac{2\rho^2}{w^2(z)}}, \tag{1.3.4}$$

where V_0 represents the maximum depth of the the optical potential. This example of 1D OL is sketched in Fig. 1.5 (right). An atomic cloud in a deep potential of this kind gets "sliced" into pancake-shaped traps of radius $\sim w_0$ and thickness $\sim \lambda_L/2$, which provides the lattice constant.

The interference mechanism can be immediately extended to higher-dimensions. Bidimensional OLs result from the interference of two pairs of counterpropagating beams, as depicted in Fig. 1.6 (a). In this case atoms form a collection of highly elongated cigar-shaped traps in which the axial trapping frequency (of the order of 10-200Hz) is much smaller than the radial one (∼100kHz). Three orthogonal standing waves generate a micro-trap structure with the periodicity of a simple cubic lattice, as shown in Fig. 1.6 (b). For distances $r \ll w_0$ from the common focal point, the trapping potential is well approximated by a homogeneous periodic lattice potential

$$V_{\mathrm{OL}}^{\mathrm{3D}} = V_0 \left(\sin^2(2\pi x/\lambda_L) + \sin^2(2\pi y/\lambda_L) + \sin^2(2\pi z/\lambda_L)\right). \tag{1.3.5}$$

Nowadays the degree of control on the optical potentials is such that, playing around with lasers frequencies, geometries and polarizations, a plethora of geometrical configurations can be experimentally realized [40, 67], allowing to control the system up to the single-site and single-atom level [68, 69].

To investigate the behavior of a quantum gas in an OL, we start by considering a single atom in a periodic potential like those of Eq. (1.3.5). An important energy scale is fixed by the recoil energy $E_r = 2\pi^2\hbar^2/m\lambda_L^2$, that is the kinetic energy that a laser photon can transfer to an atom of

$s = V_0/E_r$	J/E_r	$J^{(2)}/J$	$\lvert\langle w_0 \lvert \phi_0\rangle\rvert^2$
3	0.111	0.101	0.972
5	0.066	0.052	0.984
10	0.019	0.012	0.994
15	0.007	0.003	0.996
20	0.002	0.001	0.998

Table 1.1 : For 1D optical lattices of different depths $s = V_0/E_r$. Behavior of the hopping coefficients to nearest J and next-nearest neighbors $J^{(2)}$, obtained using the Wannier functions trough Eq. (1.3.10). We also show the overlap between the single particle Wannier function w_0 and the Gaussian ground state ϕ_0 of the single-site harmonic approximation. Data from [19].

mass m. The depth of the OL is measured by the dimensionless ratio

$$s = \frac{V_0}{E_r}. \tag{1.3.6}$$

At low temperatures, an atom ideally occupies the vibrational ground state of the single site potential well, but can still gain kinetic energy by tunneling from one site to a neighboring one. The energy eigenfunctions of a particle in a periodic potential are the Bloch states

$$\psi_{n,\mathbf{p}}(\mathbf{r}) = u_n(\mathbf{r})\, e^{i\mathbf{k}\cdot\mathbf{r}}, \tag{1.3.7}$$

where n is the band index and $\mathbf{p}$ the particle quasi-momentum within the first Brillouin zone (FBZ) of the reciprocal lattice [1]. The Bloch functions (1.3.7) are essentially plane waves modulated by a periodic function $u_n(\mathbf{r})$ having the same periodicity of the potential. Consequently, each $\psi_{n,\mathbf{p}}(\mathbf{r})$ extends over the whole lattice. To evaluate the hopping between lattice sites it is convenient to introduce the Wannier functions $w_{n,\mathbf{R}}(\mathbf{r})$, related to the Bloch functions by

$$w_{n,\mathbf{R}}(\mathbf{r}) = \frac{1}{\sqrt{N_s}} \sum_{\mathbf{k}} e^{-i\mathbf{k}\cdot\mathbf{r}}\, \psi_{n,\mathbf{p}}(\mathbf{r}), \tag{1.3.8}$$

where N_s is the number of sites of the lattice, where $\mathbf{k}$ takes the N_s allowed values in the first Brillouin zone. The set of functions $w_{n,\mathbf{R}}(\mathbf{r})$ represents a single-particle orthonormal basis, alternative to the Bloch one. Each Wannier function is centered around the lattice site position $\mathbf{R}$ and only depends on the distance $\mathbf{r} - \mathbf{R}$. The Hamiltonian for a free atom in a isotropic periodic potential like those of Eq. (1.3.5) is then

$$\mathcal{H}_{\text{single}} = -\sum_{\mathbf{R},\mathbf{R}',n} J_n(\mathbf{R} - \mathbf{R}') a^\dagger_{\mathbf{R},n} a_{\mathbf{R}',n}, \tag{1.3.9}$$

where $a_{\mathbf{R}',n}$ is the annihilation operator for a particle in the corresponding Wannier state and $J_n(\mathbf{R} - \mathbf{R}')$ quantifies the gain in kinetic energy due to the tunneling from the site centered in $\mathbf{R}$ to that centered in $\mathbf{R}'$. The tunneling coefficient depends on the overlap between $w_{\mathbf{R},n}$ and $w_{\mathbf{R}',n}$ [32]:

$$J_n(\mathbf{R} - \mathbf{R}') = -\int d^3\mathbf{r}\, w^*_{n,\mathbf{R}}(\mathbf{r}) \left[V^{\text{3D}}_{\text{OL}}(\mathbf{r}) - \frac{\hbar^2\nabla^2}{2m} \right] w_{n,\mathbf{R}'}(\mathbf{r}). \tag{1.3.10}$$

J_n rapidly decays with the distance $\mathbf{R} - \mathbf{R}'$ (c.f. Tab. 1.1), so that, typically, only nearest-neighbor hopping is taken into account. At low energies, transitions to excited bands are unlikely, so that one can restrict $\mathcal{H}_{\text{single}}$ to the $n=0$ band, dropping the index n and the corresponding sum.

In the deep-lattice limit $s \gg 1$, the bottom of each lattice site is well approximated by a harmonic potential of level spacing $\hbar\omega_0 = 2E_r\sqrt{s} \gg E_r$ and characteristic length $\ell_0 = (\hbar/m\omega_0)^{1/2}$. Within this approximation, a single-particle Wannier function w_0 can be replaced by the Gaussian ground state ϕ_0 of the harmonic trap. The validity of this equivalence can be tested by looking at the overlap $|\langle w_0|\phi_0\rangle|^2$ as a function of s, reported in Tab. 1.1. The harmonic approximation turns out to be suitable in the evaluation of on-site properties, as will be pointed out in the next section. However, even when the overlap is very large, the evaluation of the tunneling coefficient replacing w_0 by ϕ_0 in Eq. (1.3.10) gives wrong results. This is because the value of J_n critically depends on the tails of the functions, that are very different between w_0 and ϕ_0. In the deep lattice regime, it is anyhow possible to write approximated expressions for the tunneling coefficient. In particular, for $s>15$, one has [19]

$$J_0(\lambda_L/2) = J \simeq \frac{4}{\sqrt{\pi}} E_r\, s^{3/4}\, e^{-2\sqrt{s}}. \tag{1.3.11}$$

1.3.2 Bose-Hubbard model

Let us now consider a matter wave made of N bosons in a isotropic optical lattice (OL), like the one in Eq. (1.3.5), in the presence of a short-range interparticle interaction V_{int}. If two bosons occupy the same lattice site, centered in $\mathbf{R}$, both of them are described by the same Wannier function $w_{\mathbf{R}}$. Their interaction energy is [32]

$$U = \iint d^3\mathbf{r}_1\, d^3\mathbf{r}_2\, w^*_{\mathbf{R}}(\mathbf{r}_1)\, w^*_{\mathbf{R}}(\mathbf{r}_2)\, V_{int}(|\mathbf{r}_1 - \mathbf{r}_2|)\, w_{\mathbf{R}}(\mathbf{r}_1)\, w_{\mathbf{R}}(\mathbf{r}_2). \tag{1.3.12}$$

If the potential range is much smaller than the lattice spacing $\lambda_L/2$, the interaction between particles sitting in different sites can be neglected. As discussed in Sec. 1.2.1, an isotropic and short-ranged potential like V_{int} can be replaced by the corresponding pseudopotential V_c^{3D} [Eq. 1.2.6]. In this case Eq. (1.3.12) becomes

$$U = g_{3D} \int d^3\mathbf{r} |w_{\mathbf{R}}(\mathbf{r})|^4 \xrightarrow{s\gg 1} \sqrt{2\pi}\, \frac{a_{3D}}{\lambda_L}\, E_r\, s^{3/4}. \tag{1.3.13}$$

The value of U for $s \gg 1$ can be easily reproduced by the local harmonic approximation of the lattice potential.

A simple model for the description of bosons in an OL can be obtained summing the kinetic energy, as expressed in Eq. (1.3.9), and all the two-body contributions U [Eq. (1.3.12)]. In this

way one obtains the Bose-Hubbard model (BHM) Hamiltonian [70]

$$\mathcal{H}_{\mathrm{BHM}} = -J \sum_{\langle \mathbf{R},\mathbf{R}' \rangle} a^{\dagger}_{\mathbf{R}} a_{\mathbf{R}'} + \frac{U}{2} \sum_{\mathbf{R}} n_{\mathbf{R}}(n_{\mathbf{R}} - 1) + \sum_{\mathbf{R}} \varepsilon_{\mathbf{R}} n_{\mathbf{R}}. \tag{1.3.14}$$

In Eq. (1.3.14) the symbol $\langle \mathbf{R}, \mathbf{R}' \rangle$ denotes that the first sum includes, for each site at position $\mathbf{R}$, only the $\mathbf{R}'$ of nearest-neighbor sites. The operator $a_{\mathbf{R}}$ annihilates a particle in the site labeled by $\mathbf{R}$, while $n_{\mathbf{R}}$ is the corresponding number operator. The hopping coefficient $J = J_0(\mathbf{R} - \mathbf{R}')$ is typically positive. The quantity $\varepsilon_{\mathbf{R}}$, which gives the zero-point energy of the single-site trap, can be spatially dependent if there is an external trapping potential. Unless differently specified, we will consider the uniform case in which $\varepsilon_{\mathbf{R}} = \varepsilon_0$ for any $\mathbf{R}$. Case by case, depending on the kind of interaction and on the OL considered, a careful mapping is needed to relate the physical quantities of the system with the model parameters J, U, and $\varepsilon_{\mathbf{R}}$. The BHM remains valid for anisotropic lattices, provided a direction dependence of the tunneling parameters is included.

Let us consider an OL in which the density of bosons per site (i.e., the lattice filling factor) is one. In such a system, a quantum phase transition ruled by the ratio U/J emerges from the BHM. In the limit $U = 0$, the ground state of the system is a BEC in which all atoms occupy the $\mathbf{p} = 0$ Bloch state. In the periodic potential, this translates in a coherent superposition of site-localized states, which corresponds to a superfluid (SF) phase. This implies that the number of atoms per site fluctuates around the average value of one. Hence, in the SF phase, there is a non-zero probability of finding two or more atoms in the same site. For finite $U > 0$, such configurations are energetically disfavored, and, in the limit $U \gg J$, the system is driven towards the configuration with exactly one atom per site. This corresponds to the Mott insulator (MI) phase. Note that in the case of two-body attraction, i.e., $U < 0$, the ground state of the BHM is the collapse of all bosons in the same lattice site.

This quantum phase transition has been observed experimentally in 2002 for a 3D OL loaded with ^{87}Rb atoms [24]. Once the scattering length $a_{3\mathrm{D}}$ is set to a positive value, the ratio U/J can be adjusted via the lattice depth s. In a shallow lattice, tunneling is naturally favored, and the system tends to the SF phase. As it can be deduced from Eqs. (1.3.11) and (1.3.13), for a deep lattice $U/J \propto \exp(2\sqrt{s})$, so that for $s \gg 1$, one can approach the condition $U \gg J$ and the MI becomes the ground state. In [24] the phase transition has been detected by time-of-flight imaging of the matter wave, after its release from the trapping and optical potentials [c.f. Fig. 1.7 (left)]. If the trapped matter wave is in the SF phase, after expansion, it develops interference peaks at positions corresponding to the Brillouin zones' centers. These comes from the coherent superposition of components originally localized around different lattice sites. In the MI, instead, atoms in different sites are completely incoherent, so that, once released, the cloud just expands ballistically without any interference phenomena. The transition between the two regimes shows up in the

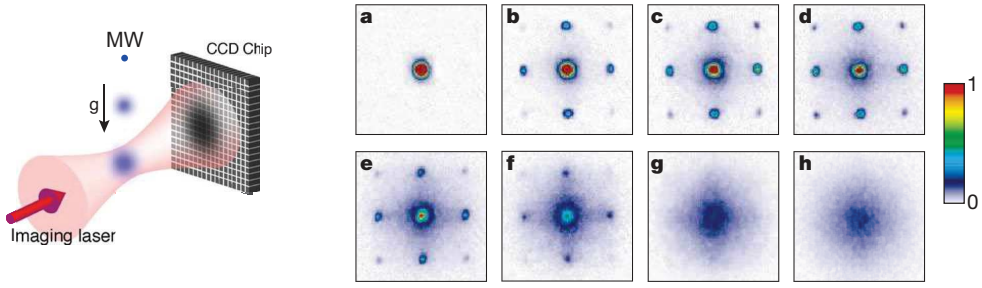

Figure 1.7 : Left: Schematic setup for absorption imaging after a time-of-flight period. The matter wave (MW) is released from its trap and falls under the effect of gravity. An imaging laser beam, resonant with the atomic transition, projects the cloud shadow on a CCD chip which captures the image. Picture from [19]. Right: Time-of-flight images of MWs released from optical lattices of different depths. In (a) $s = 0$ and the image is that of a nearly pure BEC. In (b) $s = 3$ and the interference peaks are the signature of the superfluid phase. The other panel correspond to (c) $s = 7$, (d) 10, (e) 13, (f) 14, (g) 16, and (h) 20. The interference pattern progressively disappears by increasing s, marking the transition to the Mott insulating phase. Figures from [24].

experimental pictures proposed in Fig. 1.7 (right). The SF-MI crossover is marked by the fading of the interference peaks when s is progressively increased.

1.3.3 Extended Bose-Hubbard model

The BHM relies on the hypothesis that bosons in two adjacent sites do not interact. The development of cooling and trapping techniques for dipolar particles makes it possible to realize systems beyond this limit [32]. As it will be discussed in Sec. 1.5, the dipolar interaction cannot be replaced by a contact potential, so that two-body non-local terms need to be added to the system Hamiltonian. The presence of a long-ranged interaction enriches the phase diagram with respect to that of the BHM. The simplest model accounting for non-zero-range interactions is the extended Bose-Hubbard model (EBHM) [22], which reads

$$\mathcal{H}_{\mathrm{EBHM}} = -J \sum_{\langle \mathbf{R},\mathbf{R}'\rangle} a^{\dagger}_{\mathbf{R}} a_{\mathbf{R}'} + \frac{U}{2} \sum_{\mathbf{R}} n_{\mathbf{R}}(n_{\mathbf{R}} - 1) + V \sum_{\langle \mathbf{R},\mathbf{R}'\rangle} n_{\mathbf{R}} n_{\mathbf{R}'} + \varepsilon_0 \sum_{\mathbf{R}} n_{\mathbf{R}}. \tag{1.3.15}$$

The nonzero value of V takes into account only the long-range interaction between atoms sitting in nearest-neighboring sites. The coefficient V can be evaluated similarly to U [Eq. (1.3.12)] by the two-body interaction potential V_{int} and the Wannier functions $w_{\mathbf{R}}$ [32]:

$$V = \iint d^3\mathbf{r}_1\, d^3\mathbf{r}_2\, w^*_{\mathbf{R}'}(\mathbf{r}_1)\, w^*_{\mathbf{R}'}(\mathbf{r}_2)\, V_{int}(|\mathbf{r}_1 - \mathbf{r}_2|)\, w_{\mathbf{R}}(\mathbf{r}_1)\, w_{\mathbf{R}'}(\mathbf{r}_2). \tag{1.3.16}$$

Long-range interactions might induce also other terms like two-particle hopping and density-assisted tunneling [71], which are usually neglected in the standard EBHM.

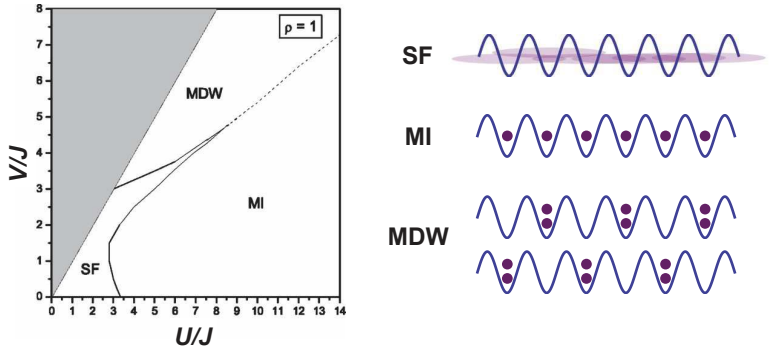

Figure 1.8 : Left: Phase diagram of the extended Bose-Hubbard Hamiltonian [Eq. (1.3.15)] for a one-dimensional lattice at unitary filling factor. Full lines indicate the insulator-superfluid (SF) crossovers. The dashed line marks the first-order transition between the two insulating phases: Mott insulator (MI) and mass density wave (MDW). The shaded region corresponds to $V > U$. Results, from [22], have been obtained by density-matrix renormalization calculations. Right: Sketches of the system configurations in the SF, MI, and the two-fold degenerate MDW.

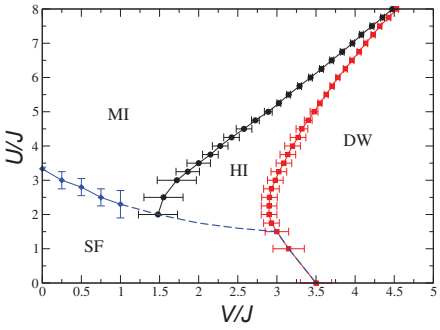

Figure 1.9 : Ground-state phase diagram for the 1D EBHM. Phase boundaries have been numerically evaluated via density-matrix renormalization group techniques in [72]. Besides the phases already presented in Fig. 1.8, the Haldane insulator (HI) appears.

The phase diagram of the EBHM in (1.3.15) is presented in Fig. 1.8 for a 1D OL loaded at unitary filling factor. Along the line $V = 0$, $\mathcal{H}_{\text{EBHM}}$ reduces to $\mathcal{H}_{\text{BHM}}$ and we find again the SF-MI transition. When $J \to 0$, two different insulating phases exist. As long as $U > 2V$, the on-site repulsion is strong enough to push atoms apart, making of the MI the system ground state. On the other hand, as soon as $U < 2V$, the nearest-neighbors repulsion gets stronger than the on-site one, so that atoms prefer to doubly occupy a site and leave empty the neighboring ones [c.f. Fig. 1.8 (right)]. The corresponding two-fold degenerate ground-state configurations are named mass density wave (MDW). In these states, the matter wave density is periodically modulated with twice the period of the OL.

It has been recently pointed out that the presence of long-range interactions in the EBHM can lead to the emergence of a further insulating phase, the Haldane insulator (HI) [73], characterized by an underlying hidden order. As shown in Fig. 1.9, such a phase can be detected between the MI and MDW. In the HI, the system is in a superposition of different configurations

in which a twice occupied site is always followed by an empty one, but the two can be separated by a string of arbitrary length of singly-populated sites [72]. This means that configurations like $\{\cdots 1,2,1,0,1,1\cdots\}$ or $\{\cdots 2,0,2,1,1,0\cdots\}$ are compatible with the HI phase, but not configurations like $\{\cdots 2,0,1,1,0,2\cdots\}$, since, excluding the singly occupied sites, two empty sites are consecutive. The preponderance of such configurations is detected evaluating the mean value of an appropriate operator, called string correlator, on the ground state of the system.

Other relevant phases occur for non-unitary filling. One can consider, for instance, the case of a 2D square lattice with filling factor $1/2$. Limiting the model to nearest-neighbors terms, the ground state of the system for $J \ll V$ is a checkerboard phase, in which, similarly to the MDW, four empty sites surround each occupied one. It is also interesting to include in the EBHM Hamiltonian [Eq. (1.3.15)] interactions beyond the nearest-neighbor one. It is possible to progressively consider farther sites [32] as well as taking all the contributions up to infinite distances [74].

1.4 Scattering in reduced dimensions

The experimental control on optical and magnetic potentials allows to strongly confine a matter wave along one or more directions, leading to systems in which the effective dimensionality is reduced. In this section we describe how the trapping potential directly affects the two-body scattering of cold particles. We begin in Sec. 1.4.1, by introducing the contact pseudopotentials for strictly 2D and 1D geometries. We then show, in Sec. 1.4.2, how the 3D contact potential [Eq. (1.2.6)] defines effective 2D and 1D scattering lengths in strongly-confined systems, discussing the emergence of confinement-induced resonances when a_{3D} or the trapping frequencies are modified. Finally, we address the problem of scattering in mixed dimensions, considering the interaction between a free particle and a trapped one. In particular, we focus in Sec. 1.4.3 on the exemplary case of 3D-1D scattering.

1.4.1 Contact pseudopotential in 1D and 2D

Before investigating the combined effects of trapping and s-wave interaction, it is useful to introduce the scattering formalism in strictly 2D and 1D systems. As for the 3D case (cf. Sec. 1.2), also in 2D and 1D it is possible to replace a short-ranged potential with a contact pseudopotential, weighted by a scattering length.

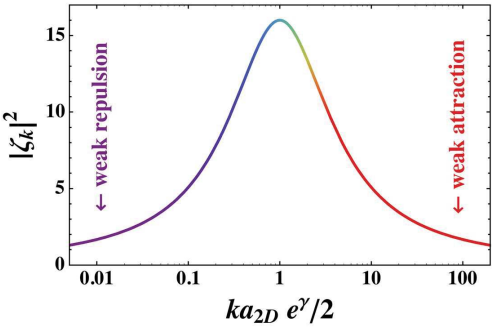

Figure 1.10 : Squared modulus of the 2D low-k scattering amplitude ζ_k [Eq. (1.4.6)]. Here a_{2D} is the 2D s-wave scattering length, while the wavevector k is related to the scattering energy by $E = \hbar^2 k^2/2\mu$. The limit $a_{2D} \to \infty$ ($a_{2D} \to 0$) corresponds to weakly attractive (repulsive) interaction.

Let us start from the 2D case. In the presence of an isotropic potential $V(\rho)$, whose finite range of interaction is ρ_0, the relative-motion 2D Schröedinger equation is

$$\left[V(\rho) - \frac{\hbar^2}{2\mu}\nabla_{\boldsymbol{\rho}}^2\right]\Psi(\boldsymbol{\rho}) = E\,\Psi(\boldsymbol{\rho}). \tag{1.4.1}$$

The scattering process looks similar to the 3D one sketched in Fig. 1.1, and, for interparticle distances $\rho \gg \rho_0$, the relative-motion wavefunction is the superposition of the incident plane wave plus an outgoing circular wave:

$$\Psi(\boldsymbol{\rho}) \propto e^{i\mathbf{k}\cdot\boldsymbol{\rho}} - \sqrt{\frac{i}{8\pi}}\, f_{2D}(k,\theta)\frac{e^{ik\rho}}{\sqrt{k\rho}}. \tag{1.4.2}$$

In Eq. (1.4.2) we introduced the quantity $f_{2D}(k,\theta)$, that is the 2D scattering amplitude modulating the outgoing circular wave [51, 75]. It is convenient to factorize the wavefunction as $\Psi(\boldsymbol{\rho}) = \psi_{\mathrm{m}}(\rho)e^{i\mathrm{m}\theta}$, so that we are left with the radial equation

$$\left[V(\rho) + \frac{\hbar^2\mathrm{m}^2}{2\mu r^2} - \frac{\hbar^2}{2\mu}\left(\frac{\partial^2}{\partial\rho^2} + \frac{1}{\rho}\frac{\partial}{\partial\rho}\right)\right]\psi_{\mathrm{m}}(\rho) = E\,\psi_{\mathrm{m}}(\rho), \tag{1.4.3}$$

where m is the angular-momentum quantum number. Similarly to the 3D case [Eq. (1.2.4)], a potential barrier emerges for states with $\mathrm{m} \neq 0$, so that only scattering in s-wave is relevant at very low energies. For $E \to 0$, Eq. 1.4.3 is solved by

$$\psi_s(\rho) = J_0(k\rho) - \frac{i}{4}\, f_{2D}(k)\, H_0^{(1)}(k\rho), \tag{1.4.4}$$

where J_0 and $H_0^{(1)}$ are the Bessel and Hankel functions. Contrary to the 3D case, the scattering amplitude f_{2D} remains k-dependent at low energies [76]:

$$f_{2D}^{-1}(k) \xrightarrow{k\to 0} \zeta_k^{-1} - \frac{r_e^2 k^2}{8\pi}, \tag{1.4.5}$$

with the introduction of the effective range of interaction r_e and of the low-k leading term

$$\zeta_k = \frac{2\pi}{i\frac{\pi}{2} - \ln\left(\frac{e^\gamma}{2}ka_{2D}\right)}. \tag{1.4.6}$$

Here a_{2D} is the the 2D s-wave scattering length and $\gamma \simeq 0.577$ is the Euler-Mascheroni constant. One obtains again the solution (1.4.4) of the Schrödinger equation 1.4.3 by replacing the true potential $V(\rho)$ by the 2D contact pseudopotential [77, 78]

$$V_c^{2D}(\rho) = -\frac{\pi\hbar^2}{\mu}\frac{1}{\ln(a_{2D}/a)}\,\delta(\rho)\left(1 - \ln(\rho/a)\rho\frac{\partial}{\partial\rho}\right), \tag{1.4.7}$$

for an arbitrary choice of the unit of length a. Note that the 2D scattering length a_{2D} can assume only positive values, ranging from zero to $+\infty$. The strength of the regularized bidimensional δ is set by the coupling constant $g_{2D} = -(\pi\hbar^2/\mu)/\ln(a_{2D}/a)$. The square modulus of the scattering amplitude (1.4.6), plotted in Fig. 1.10, constitutes an indicative quantity to visualize the properties of the 2D scattering. Being linearly proportional to the scattering cross section, it quantifies how likely the two particles feel each other. For $ka_{2D} = 2/e^{\gamma}$, $|\zeta_k|^2$ reaches its maximum value, marking the strong-interaction regime. Elsewhere the cross section decays logarithmically. Furthermore, the pseudopotential (1.4.7) admits a dimer state of energy

$$E_{\mathrm{dim}}^{2D} = -\frac{1}{\mu}\left(\frac{\hbar}{e^{\gamma}a_{2D}}\right)^2. \tag{1.4.8}$$

In the limit $a_{2D} \to \infty$ (i.e., $g_{2D} \to 0^-$) the particles weakly attract each other. For $a_{2D} \to 0$, instead, the dimer state becomes infinitely deep in energy and the interaction results weakly repulsive (i.e., $g_{2D} \to 0^+$).

For a 1D system we can proceed similarly. Let us consider a symmetric potential $V(x)$, whose finite range is x_0. In this case the Schrödinger equation reduces to

$$\left[V(x) - \frac{\hbar^2}{2\mu}\frac{\partial^2}{\partial x^2}\right]\Psi(x) = E\,\Psi(x). \tag{1.4.9}$$

For $x \gg x_0$, the relative-motion wavefunction tends to a superposition of the impinging plane wave plus an even and an odd scattered waves [14]:

$$\Psi(x) \propto e^{ikx} + f_{1D}^{e}\, e^{ik|x|} + f_{1D}^{o}\ \mathrm{sgn}(x)\, e^{ik|x|}, \tag{1.4.10}$$

where f_e and f_o are the scattering amplitudes for the even and odd channels. A crucial difference with respect to the 3D and 2D cases is that here none of the two scattering channels can be neglected at low energies, since no centrifugal barrier exists. Nevertheless, important simplifications come for identical particles. Being the center-of-mass wavefunction always symmetric under particle exchange, only the even (odd) channel will be experienced by bosonic (fermionic) particles. The corresponding scattering amplitudes can be evaluated by solving Eq. (1.4.9) for $\Psi(x) = \psi_p(x)$, where we introduced the parity index $p = e, o$. The low-energy scattering length for each channel is defined by [79]

$$a_{1D}^{p} = \lim_{x\to\infty}\left[x - \frac{\psi_p'(x)}{\psi_p(x)}\right]. \tag{1.4.11}$$

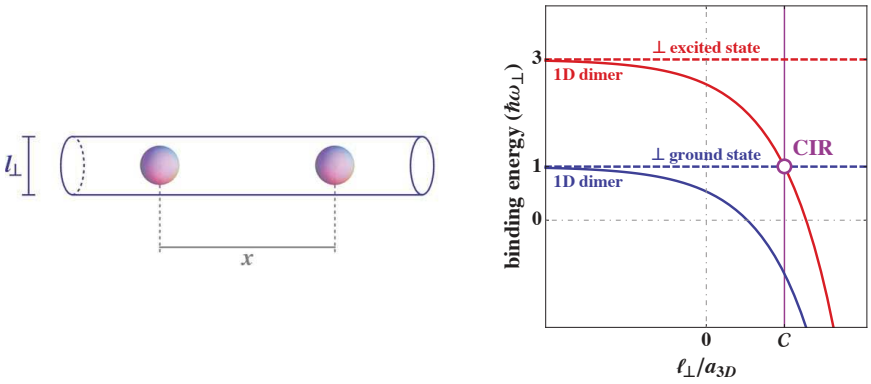

Figure 1.11 : Left: Representation of two contact-interacting particles harmonically confined on a quasi-1D tube. The tube size is fixed by the transverse-trapping characteristic length $\ell_\perp$. Right: Schematics of the mechanism responsible for the occurrence of the confinement-induced resonance (CIR) in the quasi-1D tube geometry. The energy levels near the resonance are plotted as a function of $\ell_\perp/a_{3D}$.

We stress that in the limit of a contact potential, i.e. $x_0 \to 0$, fermions do not perceive the scattering potential, being $\psi_o(0) = 0$. It follows that $f_o = 0$ and $f_e = -1/a^e_{1D}$. For this reason, from now on we will identify a^e_{1D} as the unique 1D scattering length a_{1D}, unless differently specified. The same scattering properties are obtained if the potential $V(x)$ is replaced by the 1D contact pseudopotential

$$V_c^{1D}(x) = -\frac{\hbar^2}{\mu}\frac{1}{a_{1D}}\delta(x). \tag{1.4.12}$$

1.4.2 Anisotropic trapping: confinement-induced resonances

In this section we consider the scattering process between two contact-interacting particles, both subject to an external, highly anisotropic trapping potential. We start by considering two particles, harmonically confined along the x axis, with transverse trapping frequency $\omega_\perp$ and oscillator length $\ell_\perp = (\hbar/m\omega_\perp)^{1/2}$, as sketched in Fig. 1.11 (left). The center-of-mass and relative motions are decoupled. The relative motion Hamiltonian of such a quasi-1D system is described by

$$\left[V_c^{3D}(r) + \frac{1}{2}\mu\omega_\perp^2\rho^2 - \frac{\hbar^2}{2\mu}\nabla^2_{\mathbf{r}}\right]\Psi(\mathbf{r}) = E\,\Psi(\mathbf{r}), \tag{1.4.13}$$

where we adopted a cylindrical coordinates around the x axis. Two different lengthscales compete in this system: one is set by a_{3D}, appearing in the contact potential V_c^{3D} [Eq. (1.2.6)], the other by the oscillator length $\ell_\perp$. This tube can be considered as an effective 1D system if the particle energy $E \ll \hbar\omega_\perp$. In this case the transverse component of $\Psi(\mathbf{r})$ reduces to the transverse-trap groundstate $\phi_0(\rho)$. By setting $\Psi(\mathbf{r}) = \phi_{\mathbf{0}}(\rho)\psi(x)$, Eq. (1.4.13) can be cast as an effective

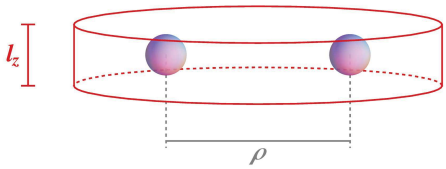

Figure 1.12 : Representation of two contact-interacting particles harmonically confined on a plane. The thickness of the quasi-2D system is fixed by the characteristic length ℓ_z.

1D Hamiltonian for $\psi(x)$:

$$\left[V_{\rm c}^{\rm 1D}(x) - \frac{\hbar^2}{2\mu}\frac{\partial^2}{\partial x^2}\right]\psi(x) = (E - \hbar\omega_\perp)\,\psi(x), \tag{1.4.14}$$

with the introduction in $V_{\rm c}^{\rm 3D}$ of the effective 1D scattering length [14]

$$a_{\rm 1D}^{\rm eff} = \frac{\ell_\perp}{2a_{\rm 3D}}(Ca_{\rm 3D} - \ell_\perp), \qquad C \simeq 1.4604\,. \tag{1.4.15}$$

In virtue of Eq. 1.4.15, the 1D coupling parameter $g_{\rm 1D} = -\hbar^2/\mu a_{\rm 1D}^{\rm eff}$ diverges for $\ell_\perp = Ca_{\rm 3D}$, leading to a confinement-induced resonance [14, 80]. The physical origin of the resonance relies, once more, on the coupling between a scattering and a closed channel. As sketched in Fig. 1.11 (right), the resonance occurs when the scattering energy in the transverse groundstate coincides with that of a transversely excited bound state. The confinement-induced resonance allows to tune the effective interaction in quasi-1D systems and represents a crucial ingredient to reach strongly interacting regimes in which bosons behaves as impenetrable particles [81, 82].

Analogously one can consider two contact-interacting particles harmonically confined on a plane, as represented in Fig. 1.12. The Hamiltonian of this quasi-2D system is

$$\left[V_{\rm c}^{\rm 3D}(r) + \frac{1}{2}\mu\omega_z^2 z^2 - \frac{\hbar^2}{2\mu}\nabla_{\mathbf{r}}^2\right]\Psi(\mathbf{r}) = E\,\Psi(\mathbf{r}), \tag{1.4.16}$$

where the trapping frequency ω_z defines the confining length $\ell_z = (\hbar/m\omega_z)^{1/2}$ in the perpendicular direction. For $E \ll \hbar\omega_z$ we can factorize $\Psi(\mathbf{r}) = \phi_0(z)\psi(\rho)$, conveniently setting the z axis as the polar one and introducing the perpendicular ground state $\phi_0(z)$. The quasi-2D system is equivalent to the effective 2D one ruled by

$$\left[V_{\rm c}^{\rm 2D}(\rho) - \frac{\hbar^2}{2\mu}\left(\frac{\partial^2}{\partial\rho^2} + \frac{1}{\rho}\frac{\partial}{\partial\rho}\right)\right]\psi(\rho) = (E - \hbar\omega_z/2)\,\psi(\rho). \tag{1.4.17}$$

The effective 2D s-wave scattering length $a_{\rm 2D}^{\rm eff}$, entering in the contact pseudopotential $V_{\rm c}^{\rm 2D}$ [see Eq. (1.4.7)], is given by [15, 75]

$$a_{\rm 2D}^{\rm eff} = \frac{2\ell_z}{e^\gamma}\sqrt{\frac{\pi}{\mathcal{B}}}\exp\left(-\sqrt{\frac{\pi}{2}}\frac{\ell_z}{a_{\rm 3D}}\right), \qquad \mathcal{B} \simeq 0.915\,. \tag{1.4.18}$$

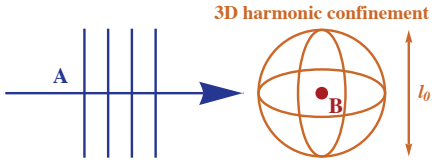

Figure 1.13 : Representation of the 0D-3D scattering process. The free atom A scatters on the B atom, confined by an isotropic harmonic trap of frequency ω_0 and associated length $\ell_0 = (\hbar/m_B\omega_0)^{1/2}$.

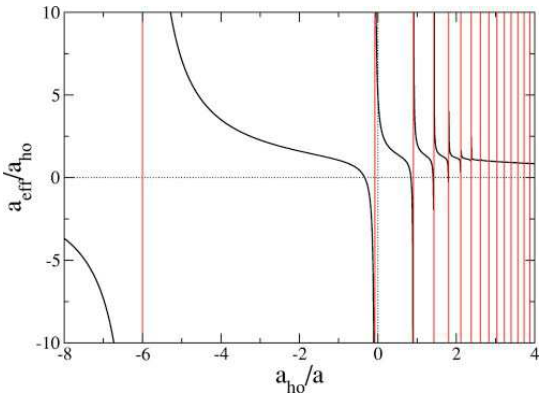

Figure 1.14 : Effective scattering length a_{3D}^{eff} [solid (black) curve] as a function of $1/a_{3D}$ for $m_B/m_A = 0.15$ (corresponding to a trapped ^{6}Li on which scatters a free ^{40}K atom). The unit of length a_{ho} corresponds to ℓ_0 in our notation. Vertical (red) lines mark the positions of the effective scattering resonances. Figure from [16].

Generally, the effective 2D scattering amplitude f_{2D} [Eq. (1.4.5)] will present the low-k resonant behavior shown in Fig. 1.10, where the role of a_{2D} is now played by a_{2D}^{eff}. In the limit of a_{3D} small and positive, $a_{2D}^{eff} \to 0$ and the contact interaction is repulsive. The effective potential can be visualized as cylindrical step of radius ℓ_z and height $V_0 \sim \hbar^2 a_{3D}/m\ell_z^3$. On the other hand, for a_{3D} small and negative, we recover the limit of weak attraction $a_{2D}^{eff} \to \infty$. In this case the potential looks, indeed, like a shallow well supporting a weakly bound state.

1.4.3 Species-dependent trapping: mix-dimensional resonances

In Sec. 1.4.2 we discussed the emergence of confinement-induced resonances when two scattering atoms are subject to the same confining potential. Here, we consider a slightly different scenario in which only one of the two particles feels a confining potential, as depicted in Fig. 1.13. This situation can be experimentally realized resorting to species-selective OLs [43, 44, 83]: optical potentials engineered to act differently on different atomic species. To give an example, we can consider the mixture of ^{87}Rb and ^{41}K used in [43], and suppose to generate an OL whose frequency falls exactly between two ^{87}Rb resonances. The attractive and repulsive optical forces [Eq. (1.3.1)] on a ^{87}Rb atom exactly cancel each other, so that only ^{41}K atoms perceive the optical potential.

We consider, in the following, the 0D-3D geometry investigated in [16] and sketched in Fig. 1.13. The elementary scattering process involves a particle A, of mass m_A, free to move in a

3D space, and a particle B, of mass m_B, trapped around $\mathbf{r}_s$ by a harmonic potential of frequency ω_0 and associated length $\ell_0 = (\hbar/m_B\omega_0)^{1/2}$. The Hamiltonian of such a system is

$$\mathcal{H} = -\frac{\hbar^2}{2m_A}\nabla^2_{\mathbf{r}_A} - \frac{\hbar^2}{2m_B}\nabla^2_{\mathbf{r}_B} + \frac{1}{2}m_B\omega_0^2|\mathbf{r}_B - \mathbf{r}_s|^2 + V_{\rm c}^{\rm 3D}\left(|\mathbf{r}_A - \mathbf{r}_B|\right), \tag{1.4.19}$$

where the contact pseudopotential $V_{\rm c}^{\rm 3D}$ is the one defined in Eq. (1.2.6). The scattering process is ruled by the masses ratio m_A/m_B, the trapping frequency ω_0 and the free-free scattering length $a_{\rm 3D}$. We restrict the analysis to low scattering energies $E \ll \hbar\omega_0$, such that after the collision the B atom still occupies the groundstate of the harmonic trap. As shown in [16], the A-atom wavefunction far from the scattering center $\mathbf{r}_s$ is the same as that of an effective system in which the free A atom impinges on a B pointlike scatterer fixed in $\mathbf{r}_s$ (i.e., $m_B \to \infty$). In this equivalent system, the scattering length $a_{\rm 3D}$ is replaced by an effective s-wave scattering length $a_{\rm 3D}^{\rm eff}$, depending on m_A/m_B, ω_0, and $a_{\rm 3D}$, which intrinsically accounts for the actual quantum motion of the B atom in the trap. An example of the nontrivial dependence of $a_{\rm 3D}^{\rm eff}$ on the real scattering length $a_{\rm 3D}$ (for a given masses ratio) is presented in Fig. 1.14. The effective scattering length experiences an infinite set of mix-dimensional resonances due to the confinement of only one of the two particles. Hence, conveniently setting $\mathbf{r}_s = 0$, the effective Hamiltonian for A simply results

$$\mathcal{H}_{\rm eff} = -\frac{\hbar^2}{2m_A}\nabla^2_{\mathbf{r}_A} + \frac{2\pi\hbar^2}{m_A}\, a_{\rm 3D}^{\rm eff}\, \delta(r_A)\, \frac{\partial}{\partial r_A}(r_A \cdots). \tag{1.4.20}$$

Other configurations, namely, the 1D-3D and 2D-3D one, have been theoretically investigated [84, 85] and some predictions on the emergence of mix-dimensional resonances have been verified experimentally [43].

1.5 Ultracold gases of dipoles

In many cases the behavior of a cold gas is well characterized by describing the interatomic interactions in terms of the contact pseudopotential introduced in Eq. (1.2.6). However, one of the most relevant cases where this is not true concerns particles with an intrinsic dipole moment, either of electric or magnetic nature, which makes them interact via the dipolar potential $V_{\rm dd}$, defined below in Eq. (1.5.1). The dipole-dipole interaction (DDI) cannot be, generally, replaced by a contact pseudopotential, due to its long-range and anisotropic nature [79]. In this section we briefly discuss the main features of the DDI and their effects on an ultracold gas, pointing at some experimental realization.

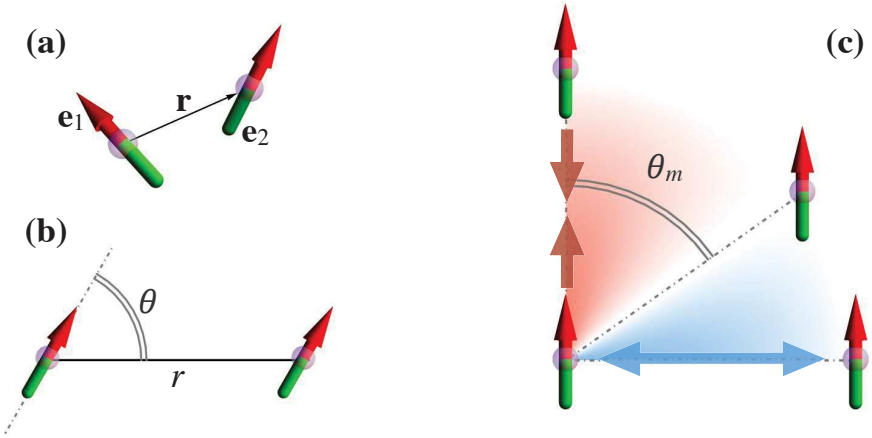

Figure 1.15 : (a) Representation of two dipolar particles arbitrarily oriented in space. The dipole-dipole interaction (DDI) [Eq. (1.5.1)] depends on their distance $\mathbf{r}$, but also on the orientations $\mathbf{e}_1$ and $\mathbf{e}_2$. (b) When the dipoles are aligned by a polarizing field the DDI simplifies [Eq. (1.5.2)] It depends on the distance r and the angle θ between the direction of polarization and the relative position of the particles. (c) Schematic representation of the DDI anisotropy. Two side-by-side dipoles repel each other, while they attract in head-to-tail configuration. The crossover between these two regimes defines the magic angle $\theta_m \simeq 54.7^\circ$ at which the DDI vanishes.

1.5.1 Properties of the dipolar interaction

When two identical particles possess either a permanent electric or magnetic dipole moment, the way in which they interact completely changes with respect to the central potential case discussed in Sec. 1.2. In particular, the dipolar potential $V_{\rm dd}$ not only depends on the interparticle distance $\mathbf{r}$, but also on the orientations of the two dipoles in space:

$$V_{\rm dd}(\mathbf{r}, \mathbf{e}_1, \mathbf{e}_2) = d^2 \frac{(\mathbf{e}_1 \cdot \mathbf{e}_2) r^2 - 3(\mathbf{e}_1 \cdot \mathbf{r})(\mathbf{e}_2 \cdot \mathbf{r})}{r^5}, \tag{1.5.1}$$

where $\mathbf{e}_1$ and $\mathbf{e}_2$ are the unit orientation vectors of the dipoles and d the dipolar strength, which will be defined later in Eq. (1.5.4) for the electric and magnetic case. This picture, represented in Fig. 1.15 (a), gets significantly simplified if we consider dipoles aligned by an external polarizing field. In this case Eq. (1.5.1) reduces to

$$V_{\rm dd}(r, \theta) = \frac{\hbar^2 r^*}{m} \frac{1 - 3\cos^2\theta}{r^3}, \tag{1.5.2}$$

where θ is the angle between polarization direction and the relative position of the particles, as represented in Fig. 1.15 (b). In Eq. (1.5.2) we introduced the dipolar length

$$r^* = \frac{m d^2}{\hbar^2}, \tag{1.5.3}$$

Species	dipole	r^*
^{87}Rb	$1.0\mu_B$	0.11nm
^{52}Cr	$6.0\mu_B$	2.4nm
^{168}Er	$7.0\mu_B$	11nm
^{164}Dy	$10\mu_B$	21nm
^{40}K^{87}Rb	0.57D	0.62μm
^{23}Na^{40}K	2.72D	7.0μm

Table 1.2 : Dipolar moments of different atomic and molecular species. The dipolar length r^* is defined in Eq.(1.5.3). Data from [25, 27–31].

which constitutes a fundamental lengthscale in dipolar systems. Two features, both captured in Eq. (1.5.2), distinguish the DDI from the typical interatomic potential $V(r)$ depicted in Fig. 1.2: the long-range behavior and the anisotropic character. A necessary condition for a potential $U(\mathbf{r})$ to be considered finite-ranged in D dimensions is that the integral $\int_{r_0}^{\infty} U(\mathbf{r})d^D\mathbf{r}$ is finite, where r_0 is a short-distance cutoff [79]. The $1/r^6$ behavior of the van der Waals potential satisfies this requirement for $D = 1, 2, 3$. The DDI decays as $1/r^3$, so that in 3D it is long-ranged. The anisotropic character is encoded in the θ-dependence of Eq. (1.5.2). In particular, the DDI is proportional to the d-wave spherical harmonic $Y_2^0(\theta, \varphi)$, being repulsive for particles sitting side by side and attractive if they are in a head-to-tail configuration, as illustrated in Fig. 1.15 (c). The crossover between these two cases defines the "magic angle" $\theta_m = \arccos(1/\sqrt{3}) \simeq 54.7°$, at which the DDI vanishes. An important consequence of these two properties is that $V_{\rm dd}$ cannot be replaced by an s-wave pseudopotential of the form (1.2.6), since also in the $k \to 0$ limit the scattering in states with $\ell \neq 0$ remains relevant and, furthermore, different partial waves are coupled by the angular dependence.

1.5.2 Electric and magnetic dipoles

Dipolar particles come in two flavors: electric and magnetic. The first are usually composite molecules in which a non-uniform charge distribution leads to a permanent electric dipole D, typically measured in Debye. Magnetic dipoles can be single atoms, in which the net magnetic moment comes from an unbalance of electronic and nuclear spins. Its magnitude depends on the Landé factor g_L of the atomic species and is given in units of the Bohr magneton μ_B. The DDI (1.5.1) depends on the squared dipole strength d^2, defined as:

$$d^2 = \begin{cases} D^2/4\pi\epsilon_0 & \text{electric dipoles,} \\ \mu_0 g_L^2 \mu_B^2/4\pi & \text{magnetic dipoles,} \end{cases} \tag{1.5.4}$$

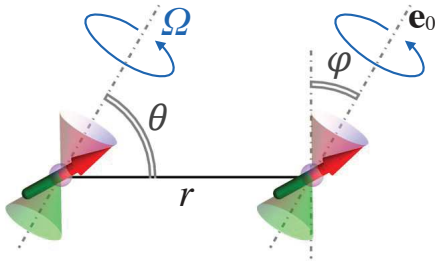

Figure 1.16 : Sketch of the rotating-field method presented in [87] to tune the strength of the interaction between permanent dipoles. The fast precession of the dipole moment around the axes $\mathbf{e}_0$ makes relevant only the time-average of the DDI. This allows to tune the dipolar length r^* in magnitude and sign.

where ϵ_0 and μ_0 are the vacuum permittivity and permeability. In Tab. 1.2 we present some values of permanent magnetic and electric dipole moments. Their effective magnitude can be compared by looking at the dipolar lengths r^*, much larger for electric than for magnetic dipoles. Note that, beyond the DDI, dipoles also feel a contact potential. This is known and independently tunable in most cases for neutral atoms [86], while much still has to be understood for heteronuclear molecules.

The intriguing perspectives opened by the DDI motivated a huge experimental effort in realizing degenerate dipolar gases. The first degenerate gas with a clear dipolar character has been realized in 2005 in Stuttgart [27], where a BEC of $\sim 5\times10^4$ atoms of ^{52}Cr has been successfully realized. The effects of the dipolar interaction, although perturbative, have been observed in the expansion dynamics of the released cloud [88]. More recently the BEC phase have been reached also with ^{168}Er [29] and ^{164}Dy [28]. An important feature for experimental purposes is the possibility to adjust the strength of the DDI with time-depent polarizing fields, through a mechanism schematically drawn in Fig. 1.16 and presented in [87]. The polarizing field is rotated at frequency Ω around an axis $\mathbf{e}_0$ on a cone of semi-aperture φ. A cloud of dipoles immersed in this field would follow the precession, so that an effective DDI is obtained by time-averaging the actual potential over the period $2\pi/\Omega$:

$$\langle V_{\rm dd}\rangle(r,\theta,\varphi) = \frac{\hbar^2}{m}\left(\frac{3\cos^2\varphi-1}{2}r^*\right)\frac{1-3\cos^2\theta}{r^3} \equiv \frac{\hbar^2}{m}\langle r^*\rangle\,\frac{1-3\cos^2\theta}{r^3}. \tag{1.5.5}$$

The angle φ plays thus the role of a tuning parameter through which adjust the effective value of the dipolar length $\langle r^*\rangle$ between r^* and $-r^*/2$.

Electric dipoles present dipolar lengths several orders of magnitude larger than those of magnetic ones and are expected to manifest stronger effects of the DDI. The best candidates in this direction are heteronuclear polar molecules. For such particles the tunability of the dipolar strength would be easier than in the magnetic case, since the magnitude of their dipole moment is proportional to the intensity of the polarizing field, up to the saturation value. These heteronuclear molecules can be obtained starting from a cold mixture of two atomic species, then associated into dimers by crossing a Feshbach resonance (cf. Sec. 1.2.2). This method led to the production of

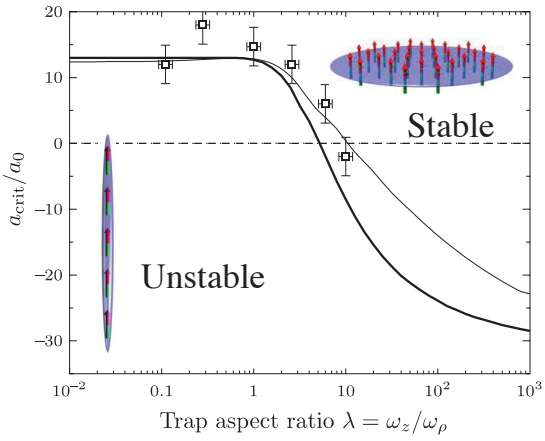

Figure 1.17 : Stability diagram of a dipolar BEC in a cylindrical harmonic trap. The aspect ratio of the confinement is defined by $\lambda = \omega_z/\omega_\rho$, where ω_z and ω_ρ are the axial and transverse trapping frequencies respectively. The trap is spherical for $\lambda = 1$, while it results cigar- (pancake-) shaped for $\lambda < 1$ ($\lambda > 1$), as sketched in the insets. The thin curve marks the stability threshold evaluated via gaussian ansatz on the BEC wavefunction [25]. The thick line comes from numerical solution of the non-local Gross-Pitaevskii equation [90]. Squares with error bars are experimental data from [91]. The scattering length is given in units of the Bohr radius $a_0 \simeq 0.53$Å. Figure from [25].

^{40}K^{87}Rb [30] and ^{23}Na^{40}K [31], whose remarkable dipolar lengths are reported in Tab. 1.2. Quantum degeneracy with this kind of composite particles has not yet been achieved, but one may expect it in a not too far future. One of the main issues is the recombination of the heteronuclear molecules into homonuclear ones after collisions. Other candidates of the electric family are light-induced dipoles and Rydberg atoms [25]. Even if their use is more and more widespread in cold-atoms experiments, their condensation is still far from being realized mainly due to lifetime reasons.

1.5.3 Stabilization and collapse

The long-range and anisotropic character of the DDI makes the stability issue central in experimental realizations of degenerate dipolar gases. Even considering the contact interaction alone, a condensate collapses for negative scattering lengths if the number of particles is larger than a critical value, eventually exploding in a Bosenova [89]. In the presence of the DDI the situation is even more complicated: the potential (1.5.2) has indeed the symmetry of a d wave, so that a region of attractive interaction exists for any value of r^*. In such a scenario, contact interaction and trapping anisotropy play a major role in determining the stability of an ultracold dipolar cloud.

It is intuitive that confining dipoles polarized in the z direction in the xy plane would stabilize the condensate, since the head-to-tail configuration gets prevented. On the other hand, in cigar-shaped trap elongated along z dipoles would likely collapse, unless a strong repulsive contact interaction overcomes the dipolar attraction. This intuition is confirmed by both numerical investigations and experimental realizations, the results of which are summarized in Fig. 1.17.

The dynamics of a collapsing BEC can unveil peculiar properties of the interatomic interactions. It is thus worth to take a peek to a collapsing dipolar BEC to see how the DDI affects this phenomenon. The first experimental observation dates back to 2008, when the collapse and

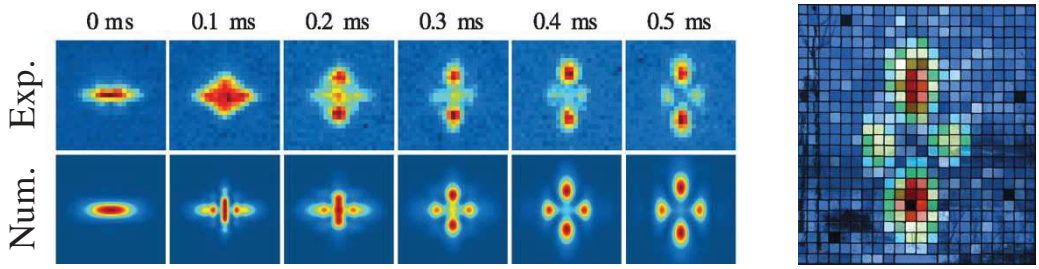

Figure 1.18 : Left: Comparison of numerical predictions and experimental results on the collapse of a dipolar BEC. The time-lapse have been obtained by time-of-flight imaging of the collapsed cloud after different in-trap evolution times. The field of view is 130μm $\times$ 130μm. Figure from [92]. Right: A stained-glass window realized by the artist Brigitte Simon, inspired by the results of [92]. Picture from [25].

explosion of a ^{52}Cr BEC have been observed [92]. In this experiment a BEC of ~20000 atoms was created in the stability region of the diagram in Fig. 1.17, then a_{3D} was rapidly switched below the stability threshold. The collapsed BEC was left evolving for an adjustable time t_{hold} and then imaged by time-of-flight measurements. A time-lapse of the collapse can be reconstructed by varying t_{hold}, obtaining the series of pictures presented in Fig. 1.18 (left). Initially, the condensate is just elongated in the polarization direction z, than it develops a torus-shaped structure on the xy plane and lobes along z, a structure reminiscent of the d-wave symmetry of the DDI.

To conclude with a pleasant curiosity, we mention that the results of [92], appeared also in the newspaper *Frankfurter Allgemeine Zeitung*, inspiring the artist Brigitte Simon in the realization of stained-glass window, pictured in Fig. 1.18 (right).

CHAPTER 2

Dipolar-Induced Resonances in Quasi-1D

In this chapter we investigate the effects of the dipole-dipole interaction (DDI) in quasi-1D geometries: systems in which the dynamics along two directions is frozen due to a tight confining potential. The DDI is known being responsible for dipolar-induced resonances (DIRs) in free space, which are low-energy resonances occurring when the dipole strength is varied. Here we consider, at first, the two-body scattering problem for dipolar particles confined along a quasi-1D tube, pointing out the emergence of a single DIR, related to the existence of a dimer-state sustained by the DDI. Hence, we turn our attention to cigar-shaped harmonic traps, introducing a two-state model to describe the DIR. The cigar trap is then taken as building block of a quasi-1D optical lattice loaded with dipolar bosons. The two-state description of the single-site physics naturally leads to the introduction of a novel atom-dimer extended Bose-Hubbard model to descibe the lattice. Its ground state is numerically investigated with exact diagonalization techniques on small-sized systems, revealing the emergence of superfluid, Mott insulator, mass density wave and collapse phases. Clues of the presence of a Haldane insulator domain are also discussed. In conclusion, both the two-body and many-body physics are strongly affected by the DIR, whose effects are likely to be detectable with present experimental techniques.

Contents

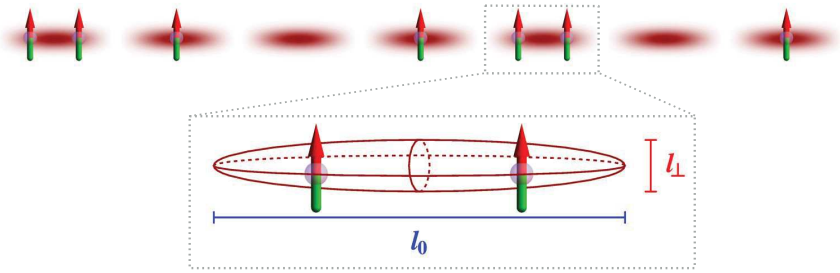

Figure 2.1 : Schematic representation of a quasi-1D optical latice loaded with dipolar bosons. Dipoles are supposed to be polarized perpendicularly to the lattice axis. The zoom-in on a single site represents its approximation by a cigar-shaped harmonic trap in which $l_\perp = (\hbar/m\omega_\perp)^{1/2}$ and $l_0 = (\hbar/m\omega_0)^{1/2}$ are the oscillator lengths associated respectively to the transverse and axial confinement.

2.1 Introduction

In the last years the study of cold dipolar gases has been boosted by the experimental realization of Bose-Einstein condensates (BECs) of magnetic atoms, such as chromium [27], erbium [29], and dysprosium [28]. In spite of the relatively weak dipolar moment of these species, perturbative effects of the dipolar interaction have been observed [88, 93]. On the other hand, encouraging developments come also from the frontline of cold heteronuclear molecules, like RbK [30] and NaK [31]. These carry much larger dipole moments of electric nature but quantum degeneracy remains to be achieved. The interest toward the dipole-dipole interaction (DDI) is motivated by its long-range and anisotropic character [25, 26]. These features, already presented in Sec. 1.5, allow to quantum simulate much more general Hamiltonians than those realizable with non-dipolar, neutral particles, disclosing new physical scenarios and intriguing properties. An example is given by the realization of optical lattices (OLs) loaded with dipolar bosons, a system already experimentally realized with atomic magnetic BECs [94] and non-condensed heteronuclear molecules [95, 96]. In such systems the long-range character of the DDI is caught by the extended Bose-Hubbard model (EBHM) discussed in Sec. 1.3.3, for which, beside the standard Mott-insulator and superfluid phases, a supersolid phase, a mass density wave [22, 97], and a Haldane insulator [72, 73] can appear.

The final goal of this chapter is the study of the many-body physics of a quasi-1D optical lattice loaded with dipolar bosons as a function of the DDI strength. The system, realizable with present experimental techniques, is thus a collection of cigar-shaped aligned micro-traps hosting dipoles which can eventually tunnel from one site to the neighboring ones, as represented in Fig. 2.1. The EBHM can be used to describe the system, prior the determination of the dependence of the model parameters on the DDI strength. It is thus essential to address, at first, the elementary two-

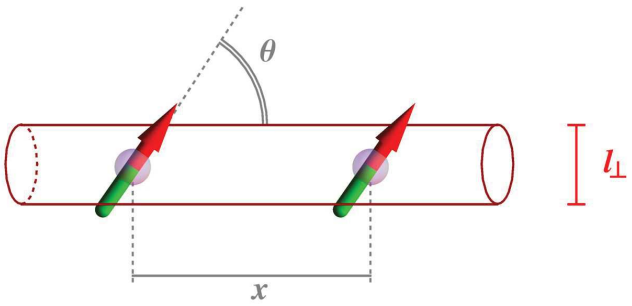

Figure 2.2 : Schematic representation of two polarized dipoles, of relative distance x, harmonically trapped along a quasi-1D tube. The tube size is determined by the confinement length $l_\perp = (\hbar/m\omega_\perp)^{1/2}$. The polarization direction and the tube axis form an angle θ.

body scattering problem for two dipolar particles in a single lattice site, task to which we dedicate Sec. 2.2. Already this preliminary study can reveal interesting features of the dipolar system, since resonances induced by the DDI are likely to occur [98]. Subsequently, in Sec. 2.3, we will focus on the optical lattice, investigating how the dipolar-induced resonances (DIRs) affect the many-body physics. We sum up our conclusions in Sec. 2.4.

2.2 Two dipoles in quasi-1D systems

This section is devoted to point out and characterize the emergence of DIRs in the two-body scattering process between dipolar particles confined in quasi-1D geometries [35, 99]. We begin showing the emergence of a single resonance in the case of two dipoles harmonically trapped along a tube [34], a system as sketched in Fig. 2.2. Then we introduce a multi-channel approach able to describe the resonance in a cigar-shaped trap. In the tight binding regime this trap represents the elementary single site of the quasi-1D optical lattice depicted in Fig. 2.1.

2.2.1 Dipolar-induced resonance in a 1D tube

Generally, the DDI [Eq. (1.5.1)] not only depends on the inter-particle distance, but also on the relative orientation of dipoles in space [25]. As shown in Sec. 1.5, it is considerably simplified by taking dipoles (of either electric or magnetic nature) aligned by a polarizing external field. In this case the relative dipolar potential takes the form

$$V_{\rm dd}(r,\theta) = \frac{\hbar^2 r^*}{m}\frac{1-3\cos^2\theta}{r^3}, \tag{2.2.1}$$

previously presented in Eq. 1.5.2, where θ is the angle between the polarization direction and relative distance vector $\mathbf{r}$ [c.f. Fig. 1.15 (b)]. The dipolar length $r^* = md^2/\hbar^2$ quantifies the strength

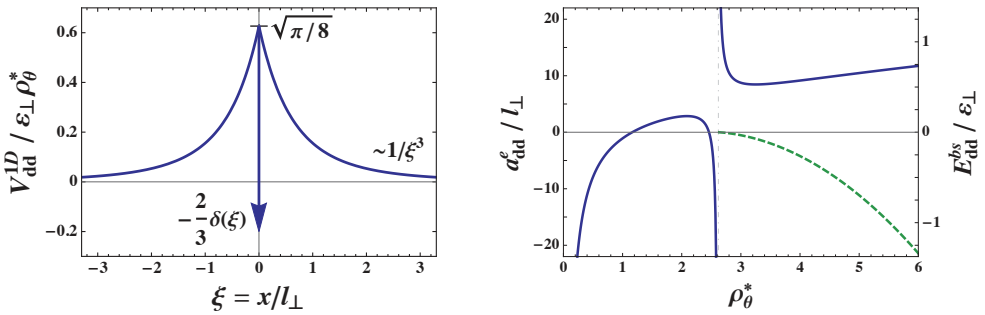

Figure 2.3 : Left: Effective 1D dipole-dipole interaction V_{dd}^{1D} [Eq. (2.2.3)] for the system presented in Fig. 2.2. Here $\theta_c < \theta < \pi/2$, corresponding to the regime in which two classical dipoles would just repel each other. Right: Numerical results for the even-channel scattering length a_{dd}^e associated to V_{dd}^{1D} as a function of the DDI strength [solid (blue)], as obtained from Eq. (2.2.7) for $x_{max} = 100 l_\perp$. A dipolar-induced resonance occurs for $\rho_\theta^* \simeq 2.6$, in coincidence with the entrance of a dipolar bound state of energy E_{dd}^{bs} [dashed (geen)]. Here $\varepsilon_\perp = \hbar\omega_\perp$ and $l_\perp = (\hbar/m\omega_\perp)^{1/2}$, where $\omega_\perp$ is the frequency of the transverse trapping potential.

of the dipole moments. The system we want to investigate, represented in Fig. 2.2, consists of two polarized dipoles harmonically trapped on a quasi-1D tube by the radial potential

$$V_\perp(\mathbf{r}) = \frac{1}{2} m\omega_\perp^2 (y^2 + z^2). \tag{2.2.2}$$

The trapping frequency $\omega_\perp$ fixes the harmonic oscillator length $l_\perp = (\hbar/m\omega_\perp)^{1/2}$. Two classical dipoles restricted to 1D motion would simply repel (attract) each other for $\theta_c < \theta < \pi/2$ ($0 < \theta < \theta_c$), where $\theta_c \simeq 54.7°$ is the "magic angle" at which the DDI vanishes [cf. Fig. 1.15 (c)]. Nevertheless, in the quantum case, we need to account for the radial extension of the particles' wavefunctions. By restricting the analysis to scattering energies $E \ll \varepsilon_\perp = \hbar\omega_\perp$, we assume the dipoles to lie in the ground state of $V_\perp$. Properly integrating out the transverse degrees of freedom [33, 100], one can map the system onto an effective 1D system, in which V_{dd} is replaced by the effective relative potential

$$V_{dd}^{1D}(x) = \varepsilon_\perp \rho_\theta^* \left[w\left(\frac{x}{l_\perp}\right) - \frac{2}{3}\delta\left(\frac{x}{l_\perp}\right) \right], \tag{2.2.3}$$

where we introduced the wing function

$$w(\xi) = \sqrt{\frac{\pi}{8}}(1 + \xi^2) \exp\left(\frac{\xi^2}{2}\right) \mathrm{erfc}\left(\frac{|\xi|}{\sqrt{2}}\right) - \frac{|\xi|}{2} \tag{2.2.4}$$

and the dimensionless quantity

$$\rho_\theta^* = \frac{r^*}{l_\perp}(1 - 3\cos^2\theta). \tag{2.2.5}$$

The derivation of Eq. (2.2.3) is described in App. A. The behavior of V_{dd}^{1D} is plotted in Fig. 2.3 (left) for $\rho_\theta^* > 0$, corresponding to the regime of classical repulsion $\theta_c < \theta < \pi/2$. Distant particles

($x \gg l_\perp$) perceive each other as classical dipoles, so that the potential has the expected $1/x^3$ behavior, reminiscent of the $1/r^3$ appearing in Eq. (2.2.1). On the other hand, getting closer, the dipoles' quantum nature emerges: the interplay of transverse extension and interaction anisotropy results in a non-divergent repulsion plus an attractive contact term. For $\rho^*_\theta < 0$ (i.e. $0 < \theta < \theta_c$) the potential is reversed, resulting mainly attractive, and for any small value of r^* there exists at least one dipolar bound state.

The scattering properties of V^{1D}_{dd} can be investigated by solving numerically the relative-motion zero-energy 1D Schrödinger equation

$$[V^{1D}_{dd}(x) - \hbar^2\partial_x^2/m]\psi_p(x) = 0. \tag{2.2.6}$$

The parity index $p = e, o$ distinguishes between even and odd solutions, corresponding, respectively, to bosonic and fermionic particles [101]. The scattering length for each channel is defined by Eq. (1.4.11):

$$a^p_{dd} = \lim_{x\to\infty}\left[x - \frac{\psi'_p(x)}{\psi_p(x)}\right]. \tag{2.2.7}$$

Due to the long-range character of V^{1D}_{dd}, it is not possible to associate to it a well defined scattering length, since Eq. (2.2.7) does not converge [79]. Anyhow, one can evaluate a^p_{dd} for a large, but finite value $x = x_{max}$ [34]. The even-channel scattering length of V_d for $x_{max} = 100 l_\perp$ is presented in Fig. 2.3 (right). A DIR occurs at $\rho^*_\theta \simeq 2.6$, due to the presence of the attractive δ-term which takes over the repulsive wings, allowing for the existence of a bound state of energy E^{bs}_{dd} also in the regime of classical repulsion. It is worth stressing how, similarly to other scattering resonances presented in Sec. 1.2, the entrance of the bound state exactly coincides with the occurence of the DIR. Remarkably, the resonance position is unaffected by the choice of x_{max}. Numerical estimations suggest that this is the only DIR existing for $\rho^*_\theta > 0$ in a quasi-1D tube. Since $\psi_o(0) = 0$, the odd branch is insensitive to the contact term in Eq. (2.2.3), so that no resonances due to the attraction-repulsion interplay arise in this scattering channel.

2.2.2 Toy model for the DIR in quasi-1D

To investigate the physical properties of V^{1D}_{dd}, we propose a versatile toy model for which a^p_{toy} is properly defined and can be evaluated analytically, together with the energy E^{bs}_{toy} of the dimer state appearing at the resonance. Hence, we replace the fast decaying wings of the 1D DDI with a finite-range step function, obtaining

$$V_{toy}(x) = \varepsilon_\perp \rho^*_\theta \left[\frac{1}{2}\,\sigma\left(\frac{x}{l_\perp}\right) - \frac{2}{3}\,\delta\left(\frac{x}{l_\perp}\right)\right], \quad \text{with} \quad \sigma(\xi) = \begin{cases} 1 & |\xi| \le 1, \\ 0 & |\xi| > 1. \end{cases} \tag{2.2.8}$$

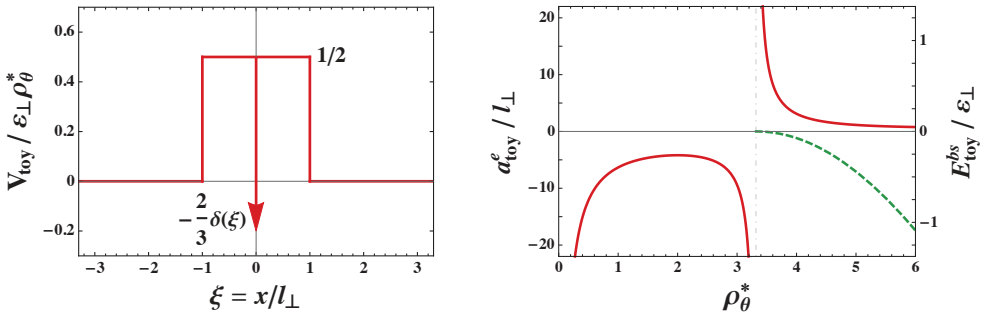

Figure 2.4 : Left: Toy potential V_{toy} [Eq. (2.2.8)] mimicking the dipole-dipole interaction V^{1D}_{dd} for the system presented in Fig. 2.2 and $\theta_c < \theta < \pi/2$. Right: Even-channel scattering length a^e_{toy} [Eq. (2.2.11), solid (red) curve] associated to V_{toy} as a function of the DDI strength. The qualitative behavior it the same as a^e_{dd} [Fig. 2.3 (right)], with a resonance occurring for $\rho^*_\theta \simeq 3.3$, coinciding with the entrance of a bound state of energy E^{bs}_{toy} [dashed (green)]. The quantities $\varepsilon_\perp$ and $l_\perp$ are defined like in Fig. 2.3.

The step width $2l_\perp$ corresponds to the region in which V^{1D}_{dd} deviates from the classical $1/x^3$ behavior, while its height $\varepsilon_\perp/2$ has been chosen so that areas under the wings $w(\xi)$ and the step $\sigma(\xi)$ are the same. The potential V_{toy} is plotted in Fig. 2.4, together with the corresponding even-channel scattering length $a^e_{toy}(\rho^*_\theta)$. The model is able to reproduce the DIR, with a resonance appearing at $\rho^*_\theta \simeq 3.3$ for even wave functions. Furthermore the analytic expression of a_{toy}, reported in Eq. (2.2.11) for a more general case, confirms that only one DIR exists for positive values of ρ^*_θ.

In addition to the DDI, we now consider the presence of a contact potential V^{1D}_c, which, as discussed in Sec. 1.4.2, depends on the 3D scattering length a_{3D} and on the tube width $l_\perp$. In the limit $a_{3D} \ll l_\perp$, this dependence is resumed by [102]:

$$V^{1D}_c(x) = 2\varepsilon_\perp \frac{a_{3D}}{l_\perp}\delta\left(\frac{x}{l_\perp}\right). \tag{2.2.9}$$

In a real system one can thus imagine to change independently the contact and long-range terms of the total interaction $V^{1D}_{dd}+V^{1D}_c$ by tuning a_{3D} via a Feshbach resonance (Sec. 1.2.2) and changing ρ^*_θ with the polarizing field (Sec. 1.5.2). Correspondingly we can generalize the toy-model potential as

$$\widetilde{V}_{toy}(x) = \varepsilon_\perp\left[\beta\,\sigma\left(\frac{x}{l_\perp}\right) + \alpha\,\delta\left(\frac{x}{l_\perp}\right)\right], \tag{2.2.10}$$

where the parameters $\alpha = 2a_{3D}/l_\perp - 2\rho^*_\theta/3$ and $\beta = \rho^*_\theta/2$ set, respectively, the contact and non-zero-range interaction strengths. By analytically solving the Schrödinger equation (2.2.6) for $\widetilde{V}_{toy}$, one gets the scattering lengths [34]

$$\widetilde{a}^e_{toy}(\alpha,\beta) = 1 - \frac{1}{\kappa}\frac{\alpha\sinh(\kappa) + 2\kappa\cosh(\kappa)}{2\kappa\sinh(\kappa) + \alpha\cosh(\kappa)}, \quad \widetilde{a}^o_{toy}(\beta) = 1 - \frac{\tanh(\kappa)}{\kappa}, \tag{2.2.11}$$

with $\kappa = \sqrt{\beta}$ for $\beta > 0$ and $\kappa = i\sqrt{|\beta|}$ for $\beta < 0$.

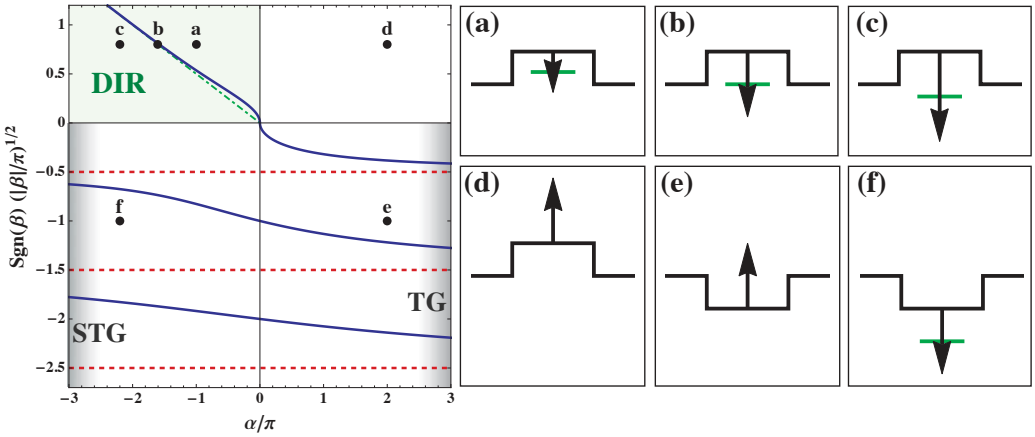

Figure 2.5 : (Color online) Left: Solid blue (dashed red) lines correspond to solutions of $1/\widetilde{a}^{e}_{\rm toy}=0$ ($1/\widetilde{a}^{o}_{\rm toy}=0$) [cf. Eq. (2.2.11)]. The green dot-dashed line marks the condition $E_\alpha = E_\beta$ (cf. text). Gray-shadowed regions ($\beta<0$) indicate the direction in which the Tonks-Girardeau (TG) and super-Tonks-Girardeau (STG) limits are asymptotically reached. The green-shadowed quadrant ($\alpha<0, \beta>0$) is the one in which the DIR mechanism occurs. Right: Illustration of the generalized toy-model potential [Eq. (2.2.10)] at the points (a,b,c,d,e,f) marked on the resonances diagram at left. Green horizontal lines represent the energy E_α of the δ-sustained bound state, shifted upwards by the height of the repulsive energy barries E_β.

In Fig. 2.5 (left) we show the position of the resonances of $\widetilde{a}^{p}_{\rm toy}$ varying α and β ($p=e,o$). The contact term is invisible to odd solutions since $\psi_o(0)=0$. Hence, the corresponding resonances do not depend on α [see Eq. (2.2.11)]. They exist only for $\beta<0$ and are simply those of a square well of depth $|\beta|$. Even solutions are, instead, strongly affected by the δ-potential. No resonances exist in the purely repulsive quadrant $\alpha,\beta>0$. For $\alpha>0$ and $\beta<0$ [Fig. 2.5 (e)], when $\alpha\to\infty$ the system reaches the Tonks-Girardeau limit of impenetrable particles [103]: even wave functions acquire a zero at the origin to avoid a divergent contribution to the energy and, correspondingly, the even resonances tend asymptotically to the odd ones. A similar even-to-odd limit occurs in the region $\alpha,\beta<0$ [Fig. 2.5 (f)]. For $\alpha\to-\infty$, the δ-potential sustains only a single, infinitely deep bound state, so that the other even wave functions must acquire a zero at the origin to keep their energy finite. The dipoles become, again, effectively impenetrable, reaching the super-Tonks-Girardeau regime [104, 105].

The DIR occurs if $\alpha<0$ and $\beta>0$. It is a (single-channel) shape resonance which results from a competition between the attractive delta term and the repulsive step potential, and it can be understood intuitively as follows. In the absence of the step potential ($\beta=0$), the δ term would support a bound state with energy $E_\alpha=-\varepsilon_\perp\alpha^2/4<0$. If we now add to the Hamiltonian a step potential whose height $E_\beta=\beta\varepsilon_\perp>0$ is smaller than $\sim|E_\alpha|$, the discrete level survives and its energy is shifted upwards by $\sim E_\beta$. On the other hand, if $E_\beta\gtrsim|E_\alpha|$, the discrete level supported by the delta

dissolves into the continuum and disappears. The resonance occurs at the threshold between these two regimes, i.e. for $E_\beta \sim |E_\alpha|$. Our results for the resonance position [Fig. 2.5 (left)] show that this condition is asymptotically exact (if $|\alpha|$ and β are both large, the resonance occurs for $E_\beta = |E_\alpha|$). In conclusion, we stress that Eq. (2.2.11) proves analytically that, for the toy model, only a single resonance in the even-channel can exist for $\alpha < 0$ and $\beta > 0$. This is analogous to the case of the DDI at $\rho^*_\theta > 0$.

2.2.3 DIR in a cigar-shaped trap

In this section we consider the building block of our quasi-1D optical lattice depicted in Fig. 2.1: the two-body problem for bosonic dipoles in a cigar-shaped harmonic trap. The physical system is similar to that considered in Sec. 2.2.1, with the addition of a harmonic potential of trapping frequency ω_0 along the tube direction. We restrict our investigation to the case of dipoles polarized perpendicularly to the long axes of the trap (more generally to $\rho^*_\theta > 0$), so that the effective DDI reduces to

$$V^{\mathrm{1D}}_{\mathrm{dd}}(x) = \varepsilon_\perp \frac{r^*}{l_\perp}\left[w\left(\frac{x}{l_\perp}\right) - \frac{2}{3}\delta\left(\frac{x}{l_\perp}\right)\right], \tag{2.2.12}$$

with the definition of $w(\xi)$ given in Eq. (2.2.4). The complete interaction potential should account also for an effective 1D contact potential $V^{\mathrm{1D}}_{\mathrm{c}}$ like the one of Eq. (2.2.9). The latter competes with the DDI to determine the stability and the phase of the system [91] and can be directly manipulated tuning a_{3D} with a Feshbach resonance [13]. Being interested in the peculiar properties of the DDI, we will consider in the following $g_{\mathrm{1D}} = 0$, unless otherwise specified.

The Hamiltonian for two particles of mass m in the equivalent 1D system is

$$\mathcal{H} = \mathcal{H}^{(1)}_{ho} + \mathcal{H}^{(2)}_{ho} + V^{\mathrm{1D}}_{\mathrm{dd}}(x_1 - x_2), \tag{2.2.13}$$

where we introduced the 1D harmonic oscillator Hamiltonian

$$\mathcal{H}^{(i)}_{ho} = -\frac{\hbar^2}{2m}\frac{\partial^2}{\partial x_i^2} + \frac{1}{2}m\omega_0^2 x_i^2. \tag{2.2.14}$$

The well known eigenfunctions of $\mathcal{H}^{(i)}_{ho}$ are

$$\psi_n(x_i) = \frac{1}{\sqrt{2^n n!}}\left(\frac{m\omega_0}{\pi\hbar}\right)^{1/4} H_n\left[\sqrt{\frac{m\omega_0}{\hbar}}\, x_i\right] e^{-\frac{m\omega_0 x^2}{2\hbar}}, \tag{2.2.15}$$

where the function H_n is the nth Hermite polynomial. The corresponding eigenvalues are

$$E_n = \left(n + \frac{1}{2}\right)\hbar\omega_0, \qquad n = 0, 1, 2, \cdots. \tag{2.2.16}$$

To solve the Schrödinger equation of the system, center-of-mass and relative motion can be decoupled. By introducing $X=(x_1+x_2)/2$ and $x=x_1-x_2$, one gets

$$\mathcal{H}=\mathcal{H}_{ho}^{\mathrm{cm}}+\mathcal{H}_{ho}^{\mathrm{rel}}+V_{\mathrm{dd}}^{\mathrm{1D}}(x). \tag{2.2.17}$$

The center-of-mass Hamiltonian is simply that of a quantum harmonic oscillator of frequency ω_0 and mass $M=2m$:

$$\mathcal{H}_{ho}^{\mathrm{cm}}=-\frac{\hbar^2}{2M}\frac{\partial^2}{\partial X^2}+\frac{1}{2}M\omega_0^2X^2. \tag{2.2.18}$$

Its eigenvalues are the same of Eq. 2.2.16, but the eigenfunctions, that we denote by $\Phi_n(X)$, differ from those of Eq. 2.2.15 in the mass M. The same argument holds for the eigenfunctions $\phi_n(x)$ of

$$\mathcal{H}_{ho}^{\mathrm{rel}}=-\frac{\hbar^2}{2\mu}\frac{\partial^2}{\partial x^2}+\frac{1}{2}\mu\omega_0^2x^2, \tag{2.2.19}$$

which contain the reduced mass $\mu=m/2$ instead of m. Note that the wavefunction of the two-body harmonic ground state satisfies $\psi_0(x_1)\psi_0(x_2)=\Phi_0(X)\phi_0(x)$.

Since the solution of the center-of-mass problem is trivial, the key point of our analysis becomes the two-body relative-motion Hamiltonian

$$\mathcal{H}_{\mathrm{2B}}=\mathcal{H}_{ho}^{\mathrm{rel}}+V_{\mathrm{dd}}^{\mathrm{1D}}(x). \tag{2.2.20}$$

Unlike for the contact interaction (see [106] and App. B), the Hamiltonian $\mathcal{H}_{\mathrm{2B}}$ cannot be diagonalized analytically, so that its ground state needs to be found numerically. A reasonable possibility is considering the restriction of $\mathcal{H}_{\mathrm{2B}}$ onto a subspace spanned by a finite number of basis states $\{|\phi_n\rangle\}$. A natural choice for such a basis is represented by the eigenstates of $\mathcal{H}_{ho}^{\mathrm{rel}}$, but the possible presence of a bound state makes this intuitive choice not suitable. Indeed, from the analysis of the tube problem proposed in Sec. 2.2.1, we saw that $V_{\mathrm{dd}}^{\mathrm{1D}}$ supports either no bound state or a single one. This bound state is present for large enough values of r^* and its entrance coincides with the occurrence of the DIR. The "bare" bound state is supported by the attractive δ-term of $V_{\mathrm{dd}}^{\mathrm{1D}}(x)$ and plays a key role. Its wavefunction can be easily derived and is

$$\psi_\delta^{bs}(x)=\sqrt{\kappa}\,e^{-\kappa|x|}, \tag{2.2.21}$$

where $\kappa=r^*/(3l_\perp^2)$, and its cusp at $x=0$ cannot be reproduced by projecting $|\psi_{\mathrm{BS}}\rangle$ onto any finite number of harmonic oscillator eigenstates, which are all smooth at $x=0$. In App. B, we come back to the problem of describing a system with a finite basis in the presence of a bound state, considering the simple example of the contact interaction. Hence, the DIR physics can only be captured if a wavefunction which has a cusp at $x=0$ is included in the basis $\{|\phi_n\rangle\}$. The smallest such basis is $\{|\phi_0\rangle,|\phi_{-1}\rangle\}$, where $|\phi_0\rangle$ is the ground state of $\mathcal{H}_{ho}^{\mathrm{rel}}$, and

$$|\phi_{-1}\rangle\propto|\psi_\delta^{bs}\rangle-\langle\phi_0|\psi_\delta^{bs}\rangle\,|\phi_0\rangle \tag{2.2.22}$$

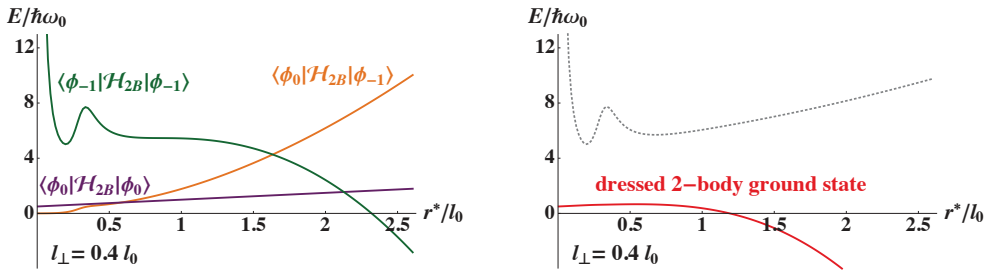

Figure 2.6 : Left: Matrix elements of the two-state Hamiltonian $\mathcal{H}_{2\text{state}}$ [Eq. (2.2.23)] describing two bosonic dipoles in a cigar-shaped harmonic trap, as a function of the dipolar length r^*. Right: Corresponding ground-state (red) and excited-state (dashed gray) energies resulting from the diagonalization of $\mathcal{H}_{2\text{state}}$. Here ω_0 and l_0 are frequency and characteristic length of the axial potential (loose confinement) while $l_\perp = 0.4 l_0$ is the length associated to the strong transverse confinement.

is a linear combination of $|\psi_\delta^{bs}\rangle$ and $|\phi_0\rangle$, chosen such that the basis is orthonormal. For a given value of r^*, we thus replace $\mathcal{H}_{2\text{B}}$ by the two-state Hamiltonian:

$$\mathcal{H}_{2\text{state}} = \begin{pmatrix} \langle\phi_{-1}|\,\mathcal{H}_{2\text{B}}\,|\phi_{-1}\rangle & \langle\phi_{-1}|\,\mathcal{H}_{2\text{B}}\,|\phi_0\rangle \\ \langle\phi_0|\,\mathcal{H}_{2\text{B}}\,|\phi_{-1}\rangle & \langle\phi_0|\,\mathcal{H}_{2\text{B}}\,|\phi_0\rangle \end{pmatrix}. \tag{2.2.23}$$

Modeling the system with $\mathcal{H}_{2\text{state}}$ corresponds to picture the DIR, i.e. a shape resonance, as a two-channel resonance. Each channel corresponds to the following two possible ground states of the system.

Open channel The dipoles are two distinct particles, both in the ground state of the harmonic trap. The two-body state of this channel is $|\psi_0^{(1)}\rangle\,|\psi_0^{(2)}\rangle$, that is equivalent to $|\Phi_0\rangle\,|\phi_0\rangle$ in center-of-mass and relative-motion coordinates.

Closed channel The dipoles form a dimer, whose state in the center-of-mass and relative coordinate is described by $|\Phi_0\rangle\,|\phi_{-1}\rangle$.

In both channels the center-of-mass gives a contribution $\hbar\omega_0/2$ to the system total energy. The diagonal elements in Eq. (2.2.23) are, instead, the different relative-motion energies of these two scattering channels. They vary as a function of r^* as represented in Fig. 2.6 (left). The off-diagonal terms couple the two channels, so that the resulting ground state $|\Psi_{2\text{B}}\rangle$ is a dressed state, mixing a bi-atomic and a dimer component.

By diagonalizing $\mathcal{H}_{2\text{state}}$ one gets the relative-motion ground-state energy $E_{2\text{B}}(r^*)$ and the corresponding wavefunction $|\Psi_{2\text{B}}(r^*)\rangle$. The non-monotonic behavior of $E_{2\text{B}}(r^*)$ is a signature of the DIR. More specifically we can identify the resonance position r^*_{crit} in the point at which the relative-motion ground-state energy goes below the zero-point energy of the harmonic oscillator $\hbar\omega_0/2$. It follows $r^*_{\text{crit}}/l_0 \simeq 0.90$ for $l_\perp/l_0 = 0.4$ [cf. Figs. 2.6 (right) and 2.7].

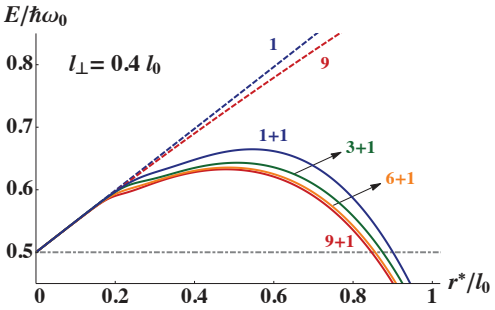

Figure 2.7 : Ground-state energy $E_{2B}(r^*)$ of the Hamiltonian $\mathcal{H}_{2B}$, for $g_{1D} = 0$ and $l_\perp/l_0 = 0.4$, including 1 (blue), 3 (green), 6 (orange), and 9 (red) harmonic oscillator states, without (dashed lines) and with (solid lines) the "bare" bound state $|\phi_{-1}\rangle$ in the projection basis. The quantities ω_0, l_0 and $l_\perp$ are defined like in Fig. 2.6.

The applicability of the quasi-1D effective potential [Eq. (2.2.12)] to our harmonically confined system requires $l_\perp/l_0$ to be small. The behavior of the matrix elements of $\mathcal{H}_{2\text{state}}$ is plotted in Fig. 2.6 for $l_\perp/l_0 = 0.4$, together with the energy $E_{2B}(r^*)$ of the dressed 2-body ground state. The qualitative behavior stays the same for smaller values of the ratio $l_\perp/l_0$.

In the many-body treatment described in the following section, we are interested in situations where the dimer population is very small. Similarly to Feshbach resonance physics [13], the existence of the closed channel has a strong impact even though it is only marginally populated. Moreover, the dimer population being nearly vanishing will help us simplify the problem to an effective open-channel model. This assumption is satisfied here, as the overlap $|\langle\phi_{-1}|\Psi_{2B}\rangle|^2$ remains smaller than 0.10 for $r^* \lesssim r^*_{\text{crit}}$. This overlap only becomes substantial if $|\phi_0\rangle$ and $|\phi_{-1}\rangle$ have comparable energies, i.e. for $r^*/l_0 \gtrsim 2.13$ (Fig. 2.6, right). The bound state population near r^*_{crit} increases as $l_\perp/l_0$ decreases, but it remains < 0.15 for $l_\perp/l_0 \geq 0.2$.

In Fig. 2.7 we analyze the behavior of the the ground-state energy $E_{2B}(r^*)$ when the diagonalization basis is extended. Moreover, the inclusion of more harmonic oscillator states allows for the calculation of higher-energy states (Fig. 2.8). The qualitative behavior of $E_{2B}(r^*)$ appears unaffected by the basis size, as long as $|\phi_{-1}\rangle$ is also included. In particular the non-monotonic character of the ground-state energy is already captured with the two-state model (2.2.23), and also the resonance position r^*_{crit} does not change significantly. On the other hand the lack of $|\phi_{-1}\rangle$ makes the resonance disappear and, even including nine oscillator eigenstates, E_{2B} increases monotonically in the investigated region of r^*.

Figure 2.8 shows the r^*-dependence of the lowest eigenvalues of $\mathcal{H}_{2B}$, evaluated diagonalizing the Hamiltonian (2.2.20) on a seven-element basis (six harmonic oscillator eigenstates plus $|\phi_{-1}\rangle$). To stress the leading role of the dipolar contact term appearing in Eq. (2.2.12), we compare this analysis in two different situations: (i) the s-wave interaction term $g_{1D} = 0$ (as everywhere else in our analysis) and (ii) $g_{1D} \neq 0$ exactly cancels the contact term in Eq. (2.2.12) [100]. The r^*-dependence of the energy levels in these two situations is completely different. When the contact term is canceled out the relative potential is purely repulsive and, as predictable, the energy of

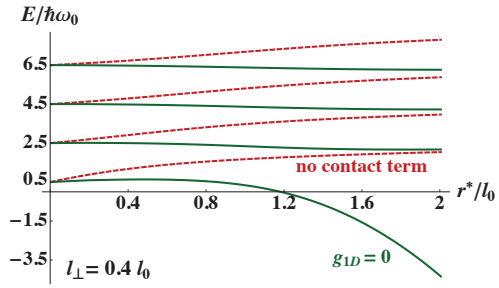

Figure 2.8 : Right: The four lowest eigenvalues of $\mathcal{H}_{2B}$ as a function of r^*, for $g_{1D} = 0$ (green) and choosing $g_{1D} = 2\hbar^2 r^*/(3ml_\perp^2)$ (dashed red) to cancel the contact term in V_{dd}^{1D}. Energies have been calculated including six harmonic oscillator states and the bare bound state $|\phi_{-1}\rangle$ in the basis. The quantities ω_0, l_0 and $l_\perp$ are defined like in Fig. 2.6.

each state monotonically grows with r^*. In particular the spacing between the ground and the first-excited state behaves clearly differently in the two cases, and this will allow for an observation of the DIR using spectroscopic techniques [107].

2.3 Dipolar bosons in a quasi-1D optical lattice

In this section we address the many-body effects of the DIR which, as pointed out in Sec. 2.2, emerges at the two-body level. For this purpose we consider N dipolar particles in a deep quasi-1D optical lattice with unity filling factor, as depicted in Fig. 2.1. Such kind of systems is typically described with the extended Bose-Hubbard model (EBHM), presented in Sec. 1.3.3. We show how the presence of a DIR at the single-site level naturally leads to the introduction of a two-band atom-dimer EBHM [35]. Its phase diagram is numerically investigated via exact diagonalization of the system Hamiltonian for small-sized optical lattices. The properties of larger systems can be inferred by means of an effective single-band model.

2.3.1 Atom-dimer extended Bose-Hubbard model

The long range character makes ultracold dipolar gases suitable for experimental implementations of the EBHM. The parameters of the model need to be carefully related to the physical quantities of the system, such as the dipole strength, measured through the length r^*, and the depth of the optical lattice. The latter is typically quantified with the parameter $s = V_0/E_R$, where V_0 is the intensity of the optical lattice and E_R is the recoil energy (see Sec. 1.3). With respect to the Bose-Hubbard model described in Sec. 1.3.2, the presence of long-range interactions is known to enrich the phase diagram of the system [20, 22, 23, 25, 26, 32]. The problem we address here is how effective the DDI can be to unveil or to hide these new phases in realistic scenarios. We focus on the regime $r^* \lesssim r^*_{\text{crit}}$, so that the DIR affects the two-body properties even though the number of dimers present in the system is extremely small. Finally we restrict our investigations to deep optical lattices, i.e. $s \gg 1$, so that the bottom of each single site is well approximated by

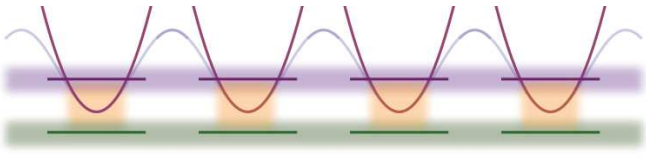

$$\mathcal{H}_{\rm AD} = \sum_i \Big[\varepsilon_a n_i + \frac{U}{2} n_i(n_i-1) - J_a(a_i^\dagger a_{i+1} + \text{H.c.}) + V n_i n_{i+1} + \varepsilon_d m_i - J_d(b_i^\dagger b_{i+1} + \text{H.c.}) + \Omega\,(b_i^\dagger a_i a_i + \text{H.c.}) \Big]$$

Figure 2.9 : Pictorial representation of the atom-dimer extended Bose-Hubbard model introduced in Eq. (2.3.1). Atomic dipoles live in the atomic band (purple) and can tunnel from site to site, similarly does dipolar dimers in the dimer band (green). The terms in $\mathcal{H}_{\rm AD}$ modeling each band are highlighted in the corresponding color. The switch of atoms into dimers, and vice versa, takes place at the single-site level at the conversion rate fixed by Ω (orange).

a harmonic potential. This implies that the analysis performed in Sec. 2.2.3 for the cigar-shaped trap gives an accurate description of the single-site physics. Due to the fast decay $\propto 1/x^3$ of the DDI with distance, we include only nearest-neighbors terms in the EBHM of our system.

As we showed in Sec. 2.2.3, the emergence of the DIR is well reproduced by a two-state description of the two-body problem [Eq. (2.2.23)]. When several sites are connected to form a lattice, atoms can tunnel from one to the nearest ones, so that each of the two states $|\phi_0\rangle$ and $|\phi_{-1}\rangle$ yields a band. Hence we introduce an atom-dimer EBHM whose Hamiltonian, schematically pictured in Fig. 2.9, reads:

$$\mathcal{H}_{\rm AD} = \sum_i \Big[\varepsilon_a n_i + \frac{U}{2} n_i(n_i-1) - J_a(a_i^\dagger a_{i+1} + \text{H.c.}) + V n_i n_{i+1} + \varepsilon_d m_i - J_d(b_i^\dagger b_{i+1} + \text{H.c.}) + \Omega(b_i^\dagger a_i a_i + \text{H.c.}) \Big]. \quad (2.3.1)$$

In Eq. (2.3.1), $a_i^\dagger$ and $b_i^\dagger$ are the creation operators in the site i for atoms and dimers, respectively, and $n_i = a_i^\dagger a_i$ and $m_i = b_i^\dagger b_i$ are the corresponding number operators. Atoms and dimers are created in the ground state of the well i.

The atomic on-site and nearest-neighbor interaction parameters U and V are defined in terms of $V_{\rm dd}^{\rm 1D}$ and the Wannier wavefunctions $w_i(x)$ and $w_{i+1}(x)$ localized on the sites i and $i+1$ by [32]:

$$U = \iint dx_1 dx_2\, w_i^2(x_1) w_i^2(x_2)\, V_{\rm dd}^{\rm 1D}(x_1 - x_2)\,, \quad (2.3.2a)$$

$$V = \iint dx_1 dx_2\, w_i^2(x_1) w_{i+1}^2(x_2)\, V_{\rm dd}^{\rm 1D}(x_1 - x_2)\,. \quad (2.3.2b)$$

We rely on the deep-lattice approximation, discussed in Sec. 1.3.1, to replace the Wannier functions $w_i(x)$ with the Gaussian functions representing the ground-state of the harmonic expansion

of the lattice potential

$$V_{\rm lat}(x) = V_0 \sin^2(2\pi x/\lambda), \tag{2.3.3}$$

where λ is the wavelength of the laser used to generate the optical lattice and V_0 its intensity. From the definition of the lattice-depth parameter $s = V_0/E_R$ and of the recoil energy $E_R = 2\pi^2\hbar^2/(m\lambda^2)$ it finally follows

$$\omega_0 = \frac{\hbar}{m}\left(\frac{2\pi}{\lambda}\right)^2 \sqrt{s}. \tag{2.3.4}$$

Eq. (2.3.4) constitutes a fundamental tool in our description of the lattice, since it connects the single-site trapping frequency ω_0 with the lattice parameters s and λ. As a side remark on the harmonic approximation we point out that the single-site energy scale and the recoil energy are simply related by $\hbar\omega_0/E_R = 2\sqrt{s}$. Similarly, the lattice spacing results $\lambda/2 = \pi l_0 \sqrt[4]{s}$, where $l_0 = (\hbar/m\omega_0)^{1/2}$ is the typical extension of the oscillator ground state in the lattice direction.

The model parameters U, ε_a, ε_d, and Ω of Eq. (2.3.1) account for on-site properties and can be directly related to the matrix elements appearing in Eq. (2.2.23). To do so we replace the Wannier state of the jth particle $|w^{(j)}\rangle$ with its Gaussian approximation $|\psi^{(j)}\rangle$. The simplest example is

$$\varepsilon_a = \langle w^{(j)}|H_{ho}^{(j)}|w^{(j)}\rangle \simeq \langle \psi^{(j)}|H_{ho}^{(j)}|\psi^{(j)}\rangle = \hbar\omega_0/2. \tag{2.3.5}$$

We proceed similarly for two-particles contributions, like U. In this case we start from the *braket* version of Eq. (2.3.2a):

$$\begin{aligned} U &= \langle w^{(1)}|\,\langle w^{(2)}|V_{\rm dd}^{\rm 1D}|w^{(2)}\rangle\,|w^{(2)}\rangle \\ &\simeq \langle \psi^{(1)}|\,\langle \psi^{(2)}|V_{\rm dd}^{\rm 1D}|\psi^{(2)}\rangle\,|\psi^{(2)}\rangle \\ &= \langle \Phi_0|\,\langle \phi_0|V_{\rm dd}^{\rm 1D}|\phi_0\rangle\,|\Phi_0\rangle \\ &= \langle \phi_0|V_{\rm dd}^{\rm 1D}|\phi_0\rangle = \langle \phi_0|\mathcal{H}_{\rm 2B}|\phi_0\rangle - \hbar\omega_0/2. \end{aligned} \tag{2.3.6}$$

All the energy of a dimer in a lattice site is encoded in

$$\begin{aligned} \varepsilon_d &\simeq \langle \Phi_0|\,\langle \phi_{-1}|\mathcal{H}_{ho}^{\rm cm} + \mathcal{H}_{\rm 2B}|\phi_{-1}\rangle\,|\Phi_0\rangle \\ &= \langle \Phi_0|\mathcal{H}_{ho}^{\rm cm}|\Phi_0\rangle + \langle \phi_{-1}|\mathcal{H}_{\rm 2B}|\phi_{-1}\rangle \\ &= \hbar\omega_0/2 + \langle \phi_{-1}|\mathcal{H}_{\rm 2B}|\phi_{-1}\rangle\,. \end{aligned} \tag{2.3.7}$$

The last single-site parameter to set is Ω. It is the conversion rate of a two-atom state $|\Phi_0\rangle\,|\phi_0\rangle$ into a one-dimer state $|\Phi_0\rangle\,|\phi_0\rangle$ in the same lattice site. Hence:

$$\begin{aligned} \sqrt{2}\,\Omega &= \langle \Phi_0|\,\langle \phi_{-1}|\mathcal{H}_{ho}^{\rm cm} + \mathcal{H}_{\rm 2B}|\phi_0\rangle\,|\Phi_0\rangle \\ &= \langle \Phi_0|\mathcal{H}_{ho}^{\rm cm}|\Phi_0\rangle\,\langle \phi_{-1}|\phi_0\rangle + \langle \Phi_0|\Phi_0\rangle\,\langle \phi_{-1}|\mathcal{H}_{\rm 2B}|\phi_0\rangle \\ &= \langle \phi_{-1}|\mathcal{H}_{\rm 2B}|\phi_0\rangle\,. \end{aligned} \tag{2.3.8}$$

The $\sqrt{2}$ factor in the previous equation comes from the fact that operators like $b_i^\dagger aa$, weighted by the parameter Ω in Eq. (2.3.1), couple a two-particles state with a single-dimer one. In summary, the single-site model parameters are

$$\varepsilon_a = \hbar\omega_0/2 \,, \tag{2.3.9a}$$

$$U = \langle\phi_0|\,\mathcal{H}_{2B}\,|\phi_0\rangle - \hbar\omega_0/2 \,, \tag{2.3.9b}$$

$$\varepsilon_d = \hbar\omega_0/2 + \langle\phi_{-1}|\,\mathcal{H}_{2B}\,|\phi_{-1}\rangle \,, \tag{2.3.9c}$$

$$\Omega = \langle\phi_{-1}|\,\mathcal{H}_{2B}\,|\phi_0\rangle \,/\, \sqrt{2} \,. \tag{2.3.9d}$$

Making use of the harmonic approximation, the nearest-neighbor coefficient V can be easily calculated from the integral expression in Eq. (2.3.2b). Case by case, we verified that the Gaussian approximation gives a good agreement with the values obtained using the exact Wannier functions. Finally, for the atomic tunneling coefficient J_a we used the numerical approximation [108]

$$\frac{J}{\hbar\omega_0} \simeq 0.725\, s^{0.48}\, e^{-2.07\sqrt{s}}. \tag{2.3.10}$$

The nearly-vanishing dimer population allows for a crude description of the dimer dynamics, therefore we neglect atom-dimer and dimer-dimer interaction in the Hamiltonian (2.3.1), and we take $J_d = J_a/10$. This choice for J_d reflects the assumption that the molecule, being heavier than a single atom, less likely tunnels from one site to another. Anyhow this rough approximation does not affect our numerical results in the low-population regime we consider.

2.3.2 Quantum phases of the system

Once the model is set we can determine the quantum phases of the system at $T = 0$ by evaluating the lowest-energy state of the Hamiltonian (2.3.1). Before discussing the different phases, it is useful to determine the parameters convenient to investigate the phase diagram. Like for the two body problem, on whose solution all our analysis relies, we consider $l_\perp/l_0$ fixed and small. Hence, as shown further on in Fig. 2.10, we determine the ground state of the system in function of the two parameters r^*/l_0 (abscissa) and V/U (ordinate, right side). The choice of r^*/l_0 as phase-diagram parameter allows for a direct comparison with the two-body physics illustrated in Sec. 2.2.3. Keeping the assumption $g_{1D} = 0$, Eqs. (2.3.2) show that the ratio V/U does not depend on r^*, indeed it decays with the lattice depth s. Hence, one can exploit the one-to-one correspondence between V/U and s and equivalently use the latter as phase-diagram parameter (cf. left side of the ordinate axis in Fig. 2.10). The harmonic approximation requires s to be large enough and thus imposes an upper bound on V/U. This maximum value depends on $l_\perp/l_0$. For instance, in the case $l_\perp = 0.4 l_0$ of Fig. 2.10 we find $(V/U)_{\max} \simeq 6.2 \times 10^{-2}$.

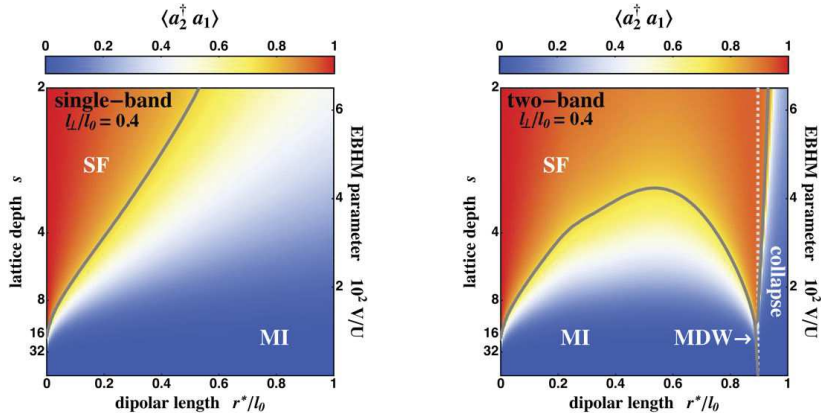

Figure 2.10 : Comparison of the many-body phase diagrams obtained using the single-band ($\Omega = 0$, left) and atom-dimer ($\Omega \neq 0$, right) EBHMs. The phases have been obtained performing exact diagonalization on a six-atom, six-well system fixing the ratio $l_\perp/l_0 = 0.4$. The effective on-site interaction $U_{\text{eff}} < 0$ on the right of the vertical dashed line. The phase boundaries have been obtained with a quasianalytical variational method described in Sec. 2.3.3. Here l_0 and $l_\perp$ are the harmonic-oscillator length respectively associated to the single-site axial and transverse potential.

N	configurations
2	5
4	85
6	1715
8	36693

Table 2.1 : Number of possible configurations for N dipoles in N lattice sites, accounting for the eventual existence of dipolar dimers. The configurations number gives the basis size for the exact diagonalization of the atom-dimer EBHM (2.3.1).

The ground state of the model is numerically detected with an exact diagonalization routine. Fixed the number of particles and lattice sites, all possible configurations of atoms and dimers in the sites are constructed and this set of configurations constitutes the basis on which the Hamiltonian (2.3.1) is diagonalized. This technique allows to know exactly the state of the system at $T = 0$ but its implementation becomes fast numerically demanding when the system size grows. The basis size, indeed, rapidly increases if the number N of particles and sites increases, as shown in Tab. 2.1. The following results have been obtained for a six-atom, six-well system. Some hint on the behavior of larger systems, up to the thermodynamic limit, can be deducted by the effective single-band approach presented in Sec. 2.3.3.

Let us consider the case $l_\perp = 0.4 l_0$. The observable in our phase diagrams is the single-particle off-diagonal density matrix element $\rho_1 = \langle a_2^\dagger a_1 \rangle$, which is able to distinguish the superfluid phase ($\rho_1 \neq 0$) from the insulating phases ($\rho_1 = 0$). The different insulating phases can subsequently be told apart by examining the ground-state wavefunction. If the emergence of the DIR is neglected

the phase diagram of the system is the one presented in the left panel of Fig. 2.10. These results have been obtained considering the single-band EBHM [22], that is analogous to put $\Omega = 0$ in Eq. (2.3.1) to prevent the conversion of atoms into dimers. In the considered range of parameters only two phases are accessible: the superfluid (SF) and the Mott insulator (MI). The fast decay of the DDI repulsive wings makes indeed V always much smaller than U, so that the mass density wave (MDW) never appears as the ground state of the system.

The right panel of Fig. 2.10 shows instead the phase diagram of the complete atom-dimer EBHM, presenting three qualitative differences with the single-band case.

1. The phase diagram includes a narrow MDW domain, occurring for very small values of V/U. A zoom-in on this region is presented in the left panel of Fig. 2.11. Such a result is in contrast with previous models which predicted the MDW phase to occur in an extended domain corresponding to large values of V/U [22].

2. The MI phase region stops at $r^* = r^*_{\mathrm{crit}}$.

3. There appears a "collapse" phase where all atoms sit in the same well. A similar phenomenon was predicted in [23] for the 2D case using a mean-field approach to calculate the Bose-Hubbard parameters. Note that, however, in the present case, the collapse occurs in a completely different geometry.

As will be described in deeper detail in Sec. 2.3.3, these features can be interpreted in terms of an effective on-site interaction U_{eff}. The DIR can make this effective interaction smaller than V, bringing the system into the MDW phase. For $r^* > r^*_{\mathrm{crit}}$, $U_{\mathrm{eff}} < 0$ and the particles collapse.

We notice that our phase diagram shows no phases with a period of three sites or more. We have checked that longer-period insulating phases are not energetically favored in virtue of the fast decay of the DDI wings. This is in agreement with the density-matrix renormalization group (DMRG) calculations including next-nearest-neighbor interactions reported in [73]. However, such phases have been predicted to occur for filling factors $\neq 1$ (see e.g. [109]).

The central and right panels of Fig. 2.11 show a zoom-in on the atom-dimer phase diagrams for $l_\perp/l_0 = 0.3$ and 0.2 respectively. The comparison with the left panel, corresponding to $l_\perp/l_0 = 0.4$, shows that decreasing the value of $l_\perp/l_0$ has a two-fold effect on the phase diagram: (i) the collapse phase, which starts at $r^* = r^*_{\mathrm{crit}}$, appears for smaller values of r^*/l_0, and (ii) the extension of the MDW phase domain is reduced. This second result suggests that the experimental observation of the MDW phase will remain difficult in quasi-1D bosonic systems. It is worth to recall that these results have been obtained considering only the DDI. Being interested in the pure dipolar effects, indeed, we assumed $g_{1\mathrm{D}} = 0$. The tuning of this additional parameter could enlarge or shift the MDW domain.

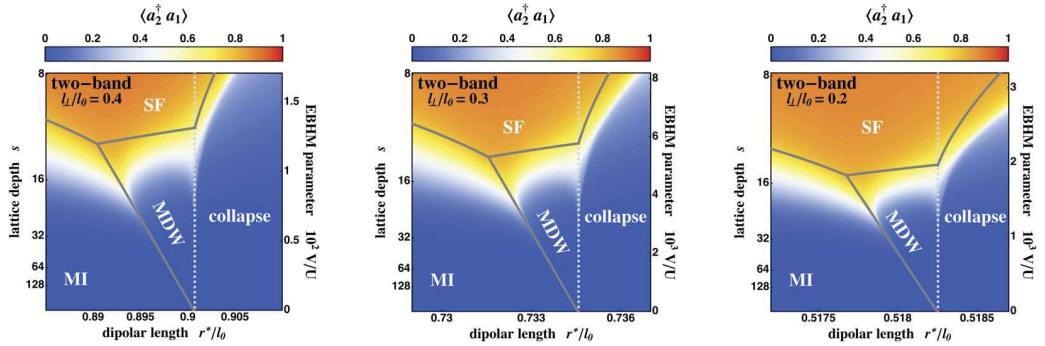

Figure 2.11 : Left: Zoom-in on the part of the atom-dimer phase diagram for $l_\perp/l_0 = 0.4$ (Fig. 2.10, right) showing the transitions between the superfluid (SF), Mott insulator (MI), mass density wave (MDW), and collapse phases. Center and right: Same as left panel, but for $l_\perp/l_0 = 0.3$ and $l_\perp/l_0 = 0.2$ respectively. The phase boundaries have been obtained with a quasianalytical variational method described in Sec. 2.3.3. Here l_0 and $l_\perp$ are the harmonic-oscillator length respectively associated to the single-site axial and transverse potential.

As mentioned before, the different insulating phases can be told apart by looking at the ground-state wavefunction projected on the basis of configurations. Such an analysis gives also some insight on the nature of the phase transitions. In Fig. 2.12 we show how the ground-state configuration evolves when the physical parameters r^*/l_0 and V/U are varied. In Fig. 2.12 (a) we fix V/U and vary r^*/l_0, observing two transitions: MI-MDW and MDW-collapse. The MI configuration $\{1, 1, 1, 1, 1, 1\}$ is the only one populated for small r^*/l_0. In the MDW the two peaks correspond to the double degeneracy of this phase, realized for both $\{2, 0, 2, 0, 2, 0\}$ and $\{0, 2, 0, 2, 0, 2\}$. Finally six configurations are equiprobable in the collapse phase, namely $\{6, 0, 0, 0, 0, 0\}$ and its permutations. In our small-sized system the insulator-insulator transitions appear sharp, in accordance with their expected first-order character. In Fig. 2.12 (b) of Fig. 2.12 we fix r^*/l_0 and vary V/U, observing both the MI-MDW and MDW-SF transitions. Contrary to the insulator-insulator cases, the transition between SF and MDW is smooth. The MDW maxima slowly disappear in a superposition of all the possible configurations, maximizing the particles delocalization. A similar behavior occurs at the SF-MI and SF-collapse boundaries. This is compatible with the Berezinskii-Kosterlitz-Thouless character predicted in 1D for such transitions [22]. With the same method we can also look for another phase, characterized by hidden order: the Haldane insulator (HI) [73]. We recall that this phase appears as a superposition of configurations in which a doubly-occupied site is always followed by an empty one but, differently from the MDW, an arbitrary number of singly-occupied sites can separate these two. To give some example, configurations like $\{1, 2, 1, 1, 0, 1\}$ or $\{2, 1, 0, 1, 2, 0\}$ are Haldane-compatible, while $\{2, 1, 2, 0, 1, 0\}$ is not because, ignoring the singly occupied sites, the ones occupied by 2 and 0 particles are not alternating. Several DMRG calculations performed on the EBHM pointed out the emergence of such a hidden ordering along the

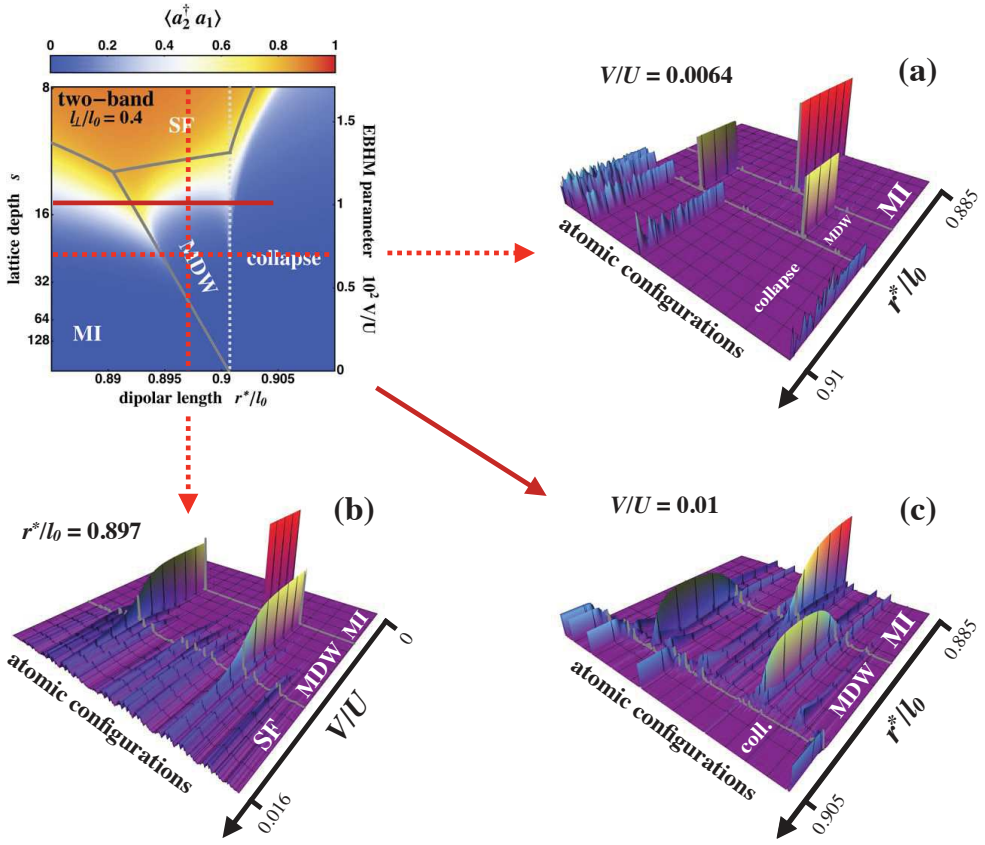

Figure 2.12 : Evolution of the ground-state wavefunction of the optical lattice along relevant paths in the phase diagram for $l_\perp = 0.4 l_0$ (presented in the left panel of Fig. 2.11 and reported here in the top-left panel). The wavefunction is projected on the basis of atomic configurations on which $H_{\rm AD}$ have been diagonalized (dimer and atom+dimer configurations are not represented since their occupation is always negligible). Panel a: Evolution as a function of r^* (horizontal line at $V/U = 0.0064$) showing the sharp MI-MDW and MDW-collapse phase transitions. Panel b: Evolution as a function of V/U (vertical line at $r^* = 0.897 l_0$) showing both the sharp MI-MDW transition and the smooth MDW-SF crossover. Panel c: Another evolution as a function of r^* (horizontal line at $V/U = 0.01$). This path crosses the region in which an Haldane insulator phase is likely to emerge. Here l_0, $l_\perp$, and the phases acronyms are defined as in Fig 2.11.

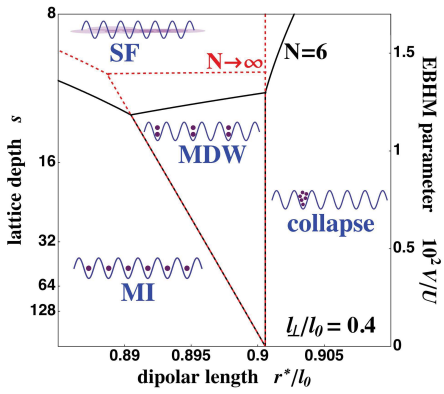

Figure 2.13 : Quasi-analytical phase boundaries calculated for the six-atom six-well system (solid black) and in the thermodynamic limit $N \to \infty$ (dashed red). The inset sketches the atomic configuration in the corresponding phases. Here l_0, $l_\perp$, and the phases acronyms are defined as in Fig 2.11.

MI-MDW transition, in the vicinity of the "triple point" where this boundary meets the SF region [72, 73]. Unfortunately the small size of our system does not allow to clearly observe the HI, but in Fig. 2.12 (c) we focus on a region of our phase diagram where some signature of the new phase can actually be detected. For $V/U = 0.01$ the MI-MDW transition happens close to the SF regime and, differently from the cases (a) and (b), beside the MI peak and the two MDW maxima other configurations are non-negligible. By looking at these latter one notices that they are all compatible with the Haldane phase.

2.3.3 Effective single-band extended Bose-Hubbard model

The negligible population of the dimer band allows for an interesting interpretation of the phase diagrams presented above using an effective single-band EBHM, where the on-site interaction U_{eff} reproduces the two-body ground-state energy:

$$\mathcal{H}_{\text{eff}} = \sum_i \left[\varepsilon_a n_i + \frac{1}{2} U_{\text{eff}} n_i(n_i - 1) - J_a(a_i^\dagger a_{i+1} + \text{H.c.}) + V n_i n_{i+1} \right], \tag{2.3.11}$$

with $U_{\text{eff}}(r^*) = E_{2\text{B}}(r^*) - \varepsilon_a$. In the parameter range explored in Figs. 2.10 and 2.11, the phase diagram obtained using $\mathcal{H}_{\text{eff}}$ is very similar to those obtained with H_{AD}. This is due to the atom-dimer detuning $\Delta = \varepsilon_d - U - 2\varepsilon_a$ being much larger than Ω, J_a and V. The two approaches are expected to yield different results for small Δ. In this case the dimer population becomes non-negligible, and the proper description of the system is given by the atom-dimer model of Eq. (2.3.1), where at this point also the parameters modeling the dimer dynamics should be carefully determined. Such a regime occurs for $r^* \simeq 2.13$ at $l_\perp = 0.4 l_0$, which is way after the largest value $r^* = 1$ that we considered in our calculations. The same reasoning applies for $l_\perp/l_0 = 0.3$ and 0.2.

The effective single-band model turns out to be extremely useful to derive quasi-analytical approximations for the phase boundaries for any number N of particles and sites. It is easy to

determine the configurations corresponding to each phase and thus, starting from the Hamiltonian (2.3.11), we can calculate the energy of the system deep within each phase in terms of J, U_{eff}, V, and N:

$$E_{\text{MI}} = N\varepsilon_a + NV, \tag{2.3.12a}$$

$$E_{\text{MDW}} = N\varepsilon_a + NU_{\text{eff}}/2, \tag{2.3.12b}$$

$$E_{\text{coll.}} = N\varepsilon_a + N(N-1)U_{\text{eff}}/2, \tag{2.3.12c}$$

$$E_{\text{SF}} = N\varepsilon_a + (N-1)U_{\text{eff}}/2 + (N-1)V - 2NJ_a. \tag{2.3.12d}$$

Equating these energies for two contiguous phases, we obtain the boundaries shown for $N = 6$ on Figs. 2.10 and 2.11. we can also predict the boundaries position in the thermodynamic limit taking $N \to \infty$. The results for the finite and infinite systems are presented in Fig. 2.13, showing that the case $N = 6$ is already very similar to $N \to \infty$. It is worth to focus on the boundary between the SF and the collapse phases, defined by

$$E_{\text{SF}} - E_{\text{coll.}} \xrightarrow{N\gg 1} N(V - 2J_a) - N^2 U_{\text{eff}}/2 = 0. \tag{2.3.13}$$

The tunneling and long-range terms scale with N, whereas the interaction one scales with N^2. Hence, for small N, the superfluid phase survives in a region where $U_{\text{eff}} < 0$, but the collapse phase is energetically favored when N increases. This instability for large N corresponds to the implosion of a Bose-Einstein condensate with a negative scattering length when its size is increased [49].

To conclude, we point out that the effective model $\mathcal{H}_{\text{eff}}$ of Eq. (2.3.11) is easier to implement numerically with DMRG methods with respect to the atom-dimer EBHM presented in Eq. (2.3.1). This allows to investigate the behavior of larger systems and to compare it with our predictions. Some preliminary calculations performed by L. Barbiero agrees with the aforementioned results for the phase boundaries position in the large-N limit. They also confirm the occurrence of a phase with HI-character when the MI-MDW transition is smooth.

2.4 Conclusions

In this chapter we considered the combined effects of reduced dimensionality and dipolar interaction. At the two-body level we pointed out the emergence of a dipolar-induced resonance (DIR) for dipolar particles tightly confined along a tube. For dipoles polarized perpendicularly to the tube direction a single resonance occurs in the even scattering channel [34]. Such a phenomenon implies the existence of a dimer-state sustained by the dipole-dipole interaction (DDI) even for regimes in which two classical dipoles would simply repel each other. The mechanism responsible for the resonance have been investigated resorting to an analitycally-solvable toy model. We

then introduced a two-state Hamiltonian to describe the DIR in a cigar-shaped harmonic potential. The main effect of the resonance is the non-monotonic behavior of the ground-state energy [35] (c.f. Fig. 2.8) which may be detected experimentally using to spectroscopic techniques [107].

After a detailed analysis of the two-body problem, we investigated the consequences of the DIR at the many-body level. The system we considered is a quasi-1D optical lattice of N sites loaded with N dipolar bosons (c.f. Fig. 2.1). Each lattice site can be approximated by a cigar-shaped trap, so that its two-state description naturally translates in the introduction of a novel atom-dimer extended Bose-Hubbard model [35] [Eq. (2.3.1)]. We discussed the new features of this model with respect to preexisting single-band ones (cf. Figs. 2.10 and 2.11). The phase boundaries can be predicted quasi-analytically by reducing the atom-dimer model to an effective single-channel one. This method allows to infer intriguing predictions for large systems without having to rely on computational-demanding numerical techniques. One possible way to explore experimentally the foregoing ground-state phase diagrams is to cool the system in a given geometry in the absence of dipolar interactions, and then adiabatically increase r^*. The phases we have predicted at $T = 0$ may be experimentally identified using in-situ imaging techniques [68] as well as the recent advances allowing for the detection of non-local order [110].

Among the possible outlooks of our study, one should for sure consider the interplay of DDI and contact interaction, in order to establish a better connection with realistic experimental situations. In our work, this has been explicitely done only in the toy-model for the two-body problem. The inclusion of an independent contact term in the atom-dimer EBHM is expected to modify the phase diagram, for instance shifting and enlarging the MDW domain. In our work, we have focused on the configuration of *classical repulsion*, but the opposite case of *classical attraction* can also bare some interesting features due to the cohexistence of an effective finite attractive potential and an induced on-site repulsion, leading to a finite, and not infinite, number of bound states.

In general, while the DDI has been widely considered in literature for different geometries and configurations, the DIR has been typically neglected. Hence, it would be interesting to reconsider such systems, looking for possible effects of the DIR. For example, one may extend our study to 2D geometries, where the anisotropy of the dipolar interaction is expected to play an important role. One may also investigate the transition between 1D and 2D, in which a dipolar gas is known to exhibit crystal-like phases for a purely repulsive DDI [111]. The extension to higher dimensions would also allow to study different lattices, like a zig-zag [112] or a staircase [113] optical lattice. In these geometries, interesting effects can arise from the interplay of anisotropic interaction and geometric frustration. In the presence of the dipolar-induced bound state, a precise mapping between real system geometry and Hamiltonian parameters, or even the introduction of a two-channel model, might be required also in the case of disordered systems [114, 115].

Another possible development line consists in the study of fermionic systems. The case of attractive fermions in a quasi-1D tube has been recently investigated in [116], pointing out the existence of many-body bound states. Considering a fermionic mixture, one may explore the effects of the DIR between different spin components. Hence, our model could also be adapted to study the fermionic 1D EBHM with repulsive interactions, where the relevant phases are the spin density wave, the charge density wave, and the bond order wave [117–120].

CHAPTER 3

Bidimensional Atomic Artificial Crystals

In this chapter we present a general scheme to realize a cold-atom quantum simulator of bidimensional atomic crystals. Our model is based on the use of two independently trapped atomic species: the first one constitutes a two-dimensional matter wave which interacts only with atoms of the second species, pinned at the nodes of a two-dimensional optical lattice. By introducing a general analytic approach, we investigate the matter-wave transport properties. We propose some illustrative applications to both Bravais (square, triangular) and non-Bravais (graphene, kagomé) lattices, studying ideal periodic systems as well as experimental-size and disordered ones. Some remarkable spectral properties of these atomic artificial crystals are pointed out, such as the emergence of single and multiple gaps, flat bands, and Dirac cones. All these features can be manipulated via the widely tunable interspecies interaction.

Contents

3.1 Modeling bidimensional crystals with cold atoms

In spite of the development of supercomputers and cutting-edge numerical methods, the simulation of experimental-size many-body systems is still a hard task. Following Feynman's conjecture of a quantum simulator, it proves useful to analyze manipulable systems able to reproduce, in a controllable way, the physical scenario that one wants to investigate. As we discussed in Chapter 1, the theoretical and experimental progress of the last decades, boosted by nanotechnological needs, has made it possible to combine the properties of cold gases and optical lattices (OLs) to build up artificial simulators of condensed-matter systems [20]. A crucial factor in the success of these models is their experimental versatility. For instance, in Chapter 1 and 2, we saw that interactions between cold atoms can indeed be tuned via Feshbach [13], dipolar [98] or confinement-induced [14] resonances. This combines with the precise control on the potential landscape offered by OLs, allowing for the exploration of quantum phase transitions [21, 24]. Furthermore, these kinds of simulators enable the exploration of parameter ranges beyond those of the real material they imitate, unveiling new physical scenarios.

In solid-state physics, among the plethora of crystals that can be investigated, two-dimensional ones are of special interest due to the intriguing properties that 2D materials have been shown to possess. Up to the early 2000s the study of these systems was only of academic interest, 2D solids being considered unstable structures never observed experimentally. Things changed in 2004, when graphene was finally isolated [36]. This discovery paved the way to the study of this astonishing carbon allotrope composed of a monolayer of ions forming a honeycomb lattice in which charge carriers manifest peculiar transport properties [37, 38]. In particular, conduction and valence bands touch in isolated points of k space: the Dirac points. Around them the energy-momentum dispersion relation is conical and a Dirac-like equation for massless fermions replaces the Schrödinger equation to describe the quantum motion of the carriers. Graphene thus qualifies as a quantum electrodynamics simulator on a benchtop scale. Furthermore, relativistic effects, in general inversely proportional to the speed of light, would be enhanced in graphene: the role of c is played here by the group velocity v_g of the particles around the cone and $c/v_g \sim 300$ [37].

The growing attention to graphene and other monolayer materials translates in an increasing interest in their quantum simulators, so that many artificial prototypes of 2D lattices have been proposed and realized in past years (for a recent review see [39]). In the present work we introduce a general, highly controllable model for the realization of artificial bidimensional lattices, based on the use of two cold-atomic species [41, 42]. In our system a 2D matter wave (MW), made up of A atoms, interacts with point-like scatterers of a second atomic species, denoted by B, independently trapped around the nodes of a 2D OL. A schematic of our model is presented in Fig. 3.1. Such a scheme is already experimentally realizable using species-selective OLs: trapping potentials

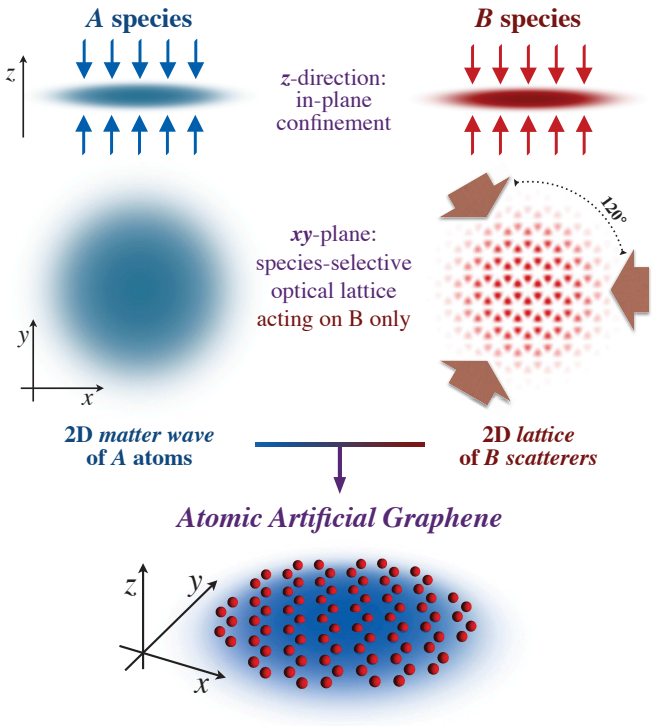

Figure 3.1 : Schematic of our model for the realization of bidimensional atomic artificial crystals, specified here to the exemplary case of the atomic artificial graphene. Two atomic species, namely, A (depicted in blue) and B (depicted in red), are strongly confined on a plane. Making use of a species-selective optical lattice, B atoms are trapped to form a 2D lattice of point-like scatterers of arbitrary geometry (a honeycomb lattice in this example). In-plane confined A atoms form a 2D matter wave which propagates through the artificial crystal.

engineered to act on an atomic species (B in the present case) being at the same moment invisible to a second one (for us, A) [43, 44, 83]. This has been done, for instance, in [43] for a mixture of ^{87}Rb and ^{41}K atoms: when the optical-lattice frequency is tuned exactly in between two ^{87}Rb resonances, the attractive and repulsive contributions to the optical force cancel each other and only ^{41}K feels the added potential. In this chapter we limit our investigations to one-body physics in the MW, i.e., we assume A atoms to be noninteracting with themselves, a situation attainable by using polarized fermions or bosons at zero scattering length. One can instead employ the B–B interaction to reach a Mott insulating phase with exactly one atom per lattice site (cf. Sec. 1.3) and subsequently freeze the atoms in this configuration by increasing the lattice depth. Other techniques are also available to probe [68] and manipulate [69], at single-site and single-atom level, the scatterer arrangement. This model has recently been proposed to study the effects of disorder in 1D [115, 121–123], 2D, and 3D [124] systems, and it has the advantage of showing

a one-to-one correspondence with the bidimensional lattices that it can mimic: the A atoms of the MW play the role of the electronic cloud, while the deeply trapped B atoms represent the crystalline structure. Henceforth we refer to our system as an atomic artificial crystal (AAC), since the periodic potential felt by the MW is generated by other atoms and not by an optical potential.

We begin this chapter by introducing our theoretical model in Sec. 3.2. At first, we briefly address in Sec. 3.2.1 the elementary scattering process between an atom of the MW and a trapped scatterer, which amounts to a problem of scattering in reduced *and* mixed dimensions. Then, we describe the general approach to the study of finite-sized AAC in Sec. 3.2.2, treatment which naturally applies also to disordered systems. We thus conclude the presentation of the theoretical model in Sec. 3.2.3, where we specify the model to the case of infinite, periodic arrangements of the scatterers. In the second part of the chapter we apply our theoretical formalism to concrete geometries. We investigate the square (Sec. 3.3) and triangular (Sec. 3.4) lattices as illustrative examples of Bravais lattices. For both of them the spectral properties of the MW are analyzed as a function of the $A-B$ interaction strength, investigating also finite-size and disorder effects. Sec. 3.5 is entirely devoted to the atomic artificial graphene (AAG) [41], that is, an AAC whose scatterers are arranged to form an honeycomb lattice. For the AAG we point out and characterize the emergence of Dirac cones and nondispersive flat bands. Features that we find again in the kagomé lattice, investigated in Sec. 3.6. Finally, we present or conclusions in Sec. 3.7.

3.2 Theoretical approach

This section is devoted to the introduction of the main theoretical tools that will be used, in the following, to investigate the transport properties of a MW in an AAC. After some comment on the $A-B$ elementary scattering process, we introduce our theoretical formalism for both generic finite systems and infinite periodic crystals.

3.2.1 0D-2D scattering process

As we extensively discussed in the previous chapters, a remarkable feature of cold-atomic systems is the possibility of using experimentally controllable parameters as knobs to tune the interatomic scattering lengths. This can be done, for example, by means of Feshbach or dipolar-induced resonances [13, 34, 35, 98, 125]. When the interacting particles are subject to a trapping potential, it can, in turn, lead to confinement-induced resonances [14]. A strong trapping reduces the effective dimensionality of the system, as discussed in Sec. 1.4, where we also considered

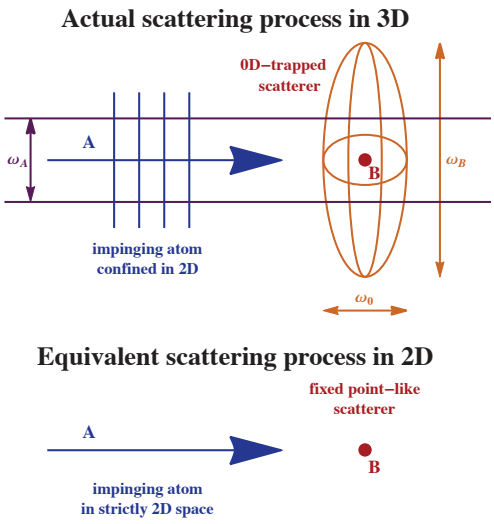

Figure 3.2 : Representation of the two-body scattering process between a 2D-trapped A atom and a 0D-trapped B atom. The scattering process in the actual system (top) is ruled by the 3D $A-B$ scattering length a_{3D} of the contact interaction, as well as by the trapping frequencies and the mass ratio of the two atomic species. The system is equivalent to a strictly bidimensional one (bottom) in which the B atom constitutes a fixed point-like scatterer and the scattering process is ruled only by an effective 2D scattering length a_{2D}^{eff} [45].

scattering processes involving differently-trapped atoms. Recently such mixed-dimension scattering have been addressed for system in which a free particle impinges on a trapped one (nD-3D scattering [16, 84, 85]) and some theoretical predictions have been tested experimentally [43].

The subject of mixed-dimension scattering is related with the physics of AACs. Indeed, the building-block of our analysis is the two-body low-energy scattering process between an A atom of mass $m_A = m$, harmonically trapped on a plane, and a B one of mass m_B, trapped around a node of an OL, a process represented schematically in Fig. 3.2. It can be shown that, by providing a proper effective 2D scattering length a_{2D}^{eff}, the system is mapped into a strictly 2D space in which the B atom is now a fixed point-like scatterer. The effective parameter a_{2D}^{eff}, which takes also into account the quantum motion of the B atom in the real system, depends on the atomic mass ratio, the trapping frequencies and the $A-B$ scattering length a_{3D} in free space (c.f. Fig. 3.2). More details about this 0D-2D scattering process are presented in App. C. For our purposes we assume, hereafter, a_{2D}^{eff} to be tunable in its full range of existence $[0, \infty[$, and that the B scatterers can be always considered point-like. In this regime the interaction can be taken into account by considering the A atom as free and imposing the Bethe-Peierls contact condition,

$$\psi(\mathbf{r}) \xrightarrow{\mathbf{r}\to\mathbf{r}_B} \frac{m}{\pi\hbar^2} D_B \ln\left(\frac{|\mathbf{r}-\mathbf{r}_B|}{a_{2D}^{\text{eff}}}\right) + O\left(|\mathbf{r}-\mathbf{r}_B|\right), \tag{3.2.1}$$

on its wave function at the position $\mathbf{r}_B$ of the scatterer, where D_B is an arbitrary complex coefficient. It is worth to briefly recall some important property of the 2D scattering, extensively discussed in Sec. 1.4.1. Contrary to the 3D and 1D cases, even at low energies the 2D scattering amplitude stays momentum-dependent and only in the limit $a_{2D}^{\text{eff}} \to \infty$ one can consider the interaction to be overall weakly repulsive. On the other hand, for $a_{2D}^{\text{eff}} \to 0$ the 2D pseudopotential [Eq. (1.4.7)] allows a single, infinitely deep bound state and results weakly repulsive for positive-energy scattering states [77, 78].

3.2.2 Finite-sized and disordered systems

Let us start by considering now a general case in which N point-like B scatterers are fixed at positions $\{\mathbf{r}_i\}$. The first steps of our calculation follow [124]: we consider the Hamiltonian of the matter wave (MW) as that of a free A atom, i.e., $\mathcal{H} = -\frac{\hbar^2}{2m}\nabla^2_{2D}$ with ∇^2_{2D} the 2D Laplace operator, and add the $A-B$ interaction by imposing the boundary conditions (3.2.1) at the position of each B scatterer. This introduces a set of N independent complex coefficients D_i. The same conditions apply to the MW Green's function, $G(\mathbf{r}, \mathbf{r}_0)$, solution of the Schrödinger equation for a point-like source term of matter waves in $\mathbf{r}_0$:

$$(E + i0^+ - \mathcal{H})G(\mathbf{r}, \mathbf{r}_0) = \delta(\mathbf{r} - \mathbf{r}_0). \tag{3.2.2}$$

The previous wave equation can be rewritten to take the boundary conditions directly into account. In particular, making use of the identity $\nabla^2_{2D}\ln(r) = 2\pi\delta(\mathbf{r})$, the effect of contact conditions resumes in the inclusion of secondary point-like sources of amplitude D_i at the position of each scatterer, leading to

$$(E + i0^+ - \mathcal{H})\, G(\mathbf{r}, \mathbf{r}_0) = \delta(\mathbf{r} - \mathbf{r}_0) + \sum_{i=1}^{N} D_i\, \delta(\mathbf{r} - \mathbf{r}_i). \tag{3.2.3}$$

Since the poles of G (and of its analytical continuation to complex energies in the lower half-plane) correspond to eigenstates of the system, its knowledge is of fundamental importance to determine the properties of the AAC.

To integrate Eq. (3.2.3) we use its solution in the absence of scatterers, which is the case for a free 2D MW. In this case, $G(\mathbf{r}, \mathbf{r}_0) = g_0(\mathbf{r} - \mathbf{r}_0)$, with

$$g_0(\mathbf{r}) = -i\frac{m}{2\hbar^2}H_0^{(1)}(kr). \tag{3.2.4}$$

In Eq. (3.2.4), $H_0^{(1)}$ is the zero-index Hankel function of the first kind and the wave-vector modulus k is linked to the MW energy by the usual relation

$$E = \frac{\hbar^2 k^2}{2m}, \tag{3.2.5}$$

with $k > 0$ for $E > 0$ and $k = i\kappa$ with $\kappa > 0$ for $E < 0$ (i.e. for bound states). Hence, we can cast the formal solution of the wave equation (3.2.3) as

$$G(\mathbf{r}, \mathbf{r}_0) = g_0(\mathbf{r} - \mathbf{r}_0) + \sum_{i=1}^{N} D_i\, g_0(\mathbf{r} - \mathbf{r}_i), \tag{3.2.6}$$

where the determination of the N coefficients D_i depends on the system geometry, encoded in the set $\{\mathbf{r}_i\}$. This problem can be tracked back to the solution of a complex linear system in the N

unknowns D_i. Each equation of this system comes from the limit $\mathbf{r} \to \mathbf{r}_j$ of Eq. (3.2.6), imposing the Bethe-Peierls condition (3.2.1) on the left-hand side and applying

$$H_0^{(1)}(kr) \xrightarrow[r\to 0]{} 1 + \frac{2i}{\pi} \ln\left(\frac{e^\gamma}{2} kr\right) + o(1) \tag{3.2.7}$$

on the right-hand side, where $\gamma \simeq 0.577216$ is the Euler-Mascheroni constant. After some straightforward algebraic manipulation the complex system becomes

$$\sum_{i=1}^{N} \mathbb{M}_{ji} D_i = -\frac{\pi\hbar^2}{m} g_0(\mathbf{r}_j - \mathbf{r}_0) \qquad j = 1, 2, \cdots, N, \tag{3.2.8}$$

with the introduction of the matrix $\mathbb{M}$ of elements

$$\mathbb{M}_{ji} = \begin{cases} \frac{\pi\hbar^2}{m} g_0(\mathbf{r}_j - \mathbf{r}_i) & \mathbf{r}_j \neq \mathbf{r}_i, \\ \ln\left(\frac{e^\gamma}{2} k a_{2\mathrm{D}}^{\mathrm{eff}}\right) - i\frac{\pi}{2} & \mathbf{r}_j = \mathbf{r}_i. \end{cases} \tag{3.2.9}$$

The formal solution of G [Eq. (3.2.6)] has a pole if $\mathbb{M}$ is not invertible, i.e., if

$$\det(\mathbb{M}) = 0. \tag{3.2.10}$$

In conclusion we can take Eq. (3.2.10) as our general condition for the existence of an eigenstate for a MW propagating in a gas of scatterers pinned at positions $\{\mathbf{r}_i\}$. Such a general approach holds equally for quasi-periodic crystals, finite-size structures, and random distributions of scatterers.

In view of a numerical implementation of the theoretical model, we stress that condition (3.2.10) can be rewritten in a more practical form by noting that the interaction-dependent terms appear only in the diagonal elements of $\mathbb{M}$. In particular, one can write

$$\mathbb{M}_{jj} = \ln\left(\frac{e^\gamma}{2} ka\right) - i\frac{\pi}{2} + \alpha, \tag{3.2.11}$$

with the introduction of the 2D interaction coefficient

$$\alpha = \ln(a_{2\mathrm{D}}^{\mathrm{eff}}/a), \tag{3.2.12}$$

and for an arbitrary choice of the unitary length a. It follows that $\mathbb{M} = \mathbb{M}^o + \mathbb{I}\alpha$, for $\mathbb{M}^o = \mathbb{M}(\alpha = 0)$ and $\mathbb{I}$ the $N \times N$ identity matrix. For $E < 0$ the matrix $\mathbb{M}^o$ is real, and looking for solutions of $\det(\mathbb{M}) = 0$ is equivalent to solving

$$m_i^o(E) = -\alpha, \qquad i = 1, 2, \cdots, N, \tag{3.2.13}$$

for each of the N eigenvalues m_i^o of $\mathbb{M}^o$. Solutions of Eq. (3.2.13) give real and negative energies of the MW bound states in the gas of scatterers. For $E > 0$ the situation is slightly different.

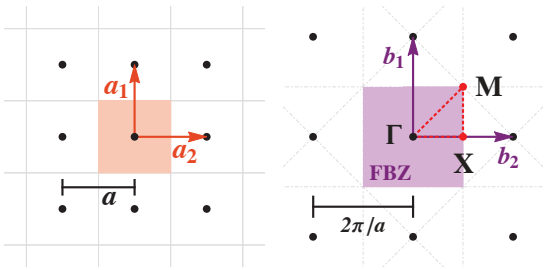

Figure 3.3 : Left: Real-space representation of a square lattice of primitive vectors $\mathbf{a}_1 = a(1,0)$ and $\mathbf{a}_2 = a(0,1)$. The shaded area represents the unit cell. Right: Reciprocal lattice in k space corresponding to the square lattice. Consequently the reciprocal primitive vectors are $\mathbf{b}_1 = \frac{2\pi}{a}(1,0)$ and $\mathbf{b}_2 = \frac{2\pi}{a}(0,1)$. The first Brillouin zone (FBZ) is shaded. The high-symmetry points $\mathbf{\Gamma} = (0,0)$, $\mathbf{X} = \frac{\pi}{a}(1,0)$, and $\mathbf{M} = \frac{\pi}{a}(1,1)$ are highlighted and the $\mathbf{\Gamma}-\mathbf{X}-\mathbf{M}-\mathbf{\Gamma}$ path [dashed (red) line] constitutes an irreducible symmetry path.

A continuum of states is allowed for the MW; nevertheless, for a large enough number of scatterers, precursors of the bulk Bloch states of the infinite periodic system can be identified in the form of complex poles of the analytical continuation of G to the lower half-plane of complex energies. In our approach, this corresponds to the fact that $\mathbb{M}^o$ is now a complex matrix and the poles of the extended G can be found by solving

$$m_i^o(z) = -\alpha, \qquad i = 1, 2, \cdots, N, \tag{3.2.14}$$

for complex energies of the form $z = E - i\hbar\Gamma/2$, where E and $\Gamma > 0$ represents, respectively, the position and band-width (i.e., inverse lifetime) of the eigenstate. The latter, in an extended and ordered system, would be a quasi-Bloch state: a state showing the periodicity properties of a Bloch state within the gas of scatterers but with a finite lifetime inside of it. Further details on the quasi-Bloch states will be discussed in Sec. 3.3.2, in the framework of the practical application of our model to the case of a finite-sized square lattice.

3.2.3 Infinite periodic systems

Infinite periodic structures play a crucial role in solid state physics, since their analysis is the starting point to understand the transport properties of charge carriers in real materials. In the same way, by looking at ideal systems we can derive bad structure and density of states for a MW in an AAC. With this purpose in mind, we develop, in the following, the transformation of the finite-size formalism introduced in Sec. 3.2.2 to a theoretical model valid for ideal periodic crystals.

3.2.3.1 Bravais lattices

In this section we adapt the general formalism introduced in Sec. 3.2.2 to the case in which the B atoms are arranged in a Bravais lattice: an infinite periodic structure where a unit cell, containing only *one* atom, is repeated to cover the entire 2D space (c.f. Figs. 3.3 and 3.4). Such a lattice is

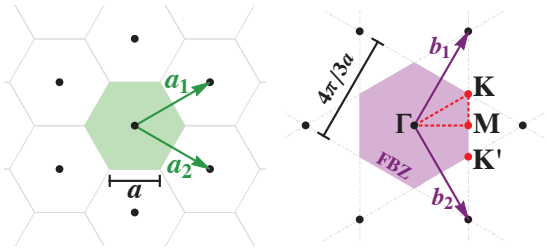

Figure 3.4 : (Color online) Left: Representation in real-space of a triangular lattice of primitive vectors $\mathbf{a}_1 = \frac{3a}{2}(1, 1/\sqrt{3})$ and $\mathbf{a}_2 = \frac{3a}{2}(1, -1/\sqrt{3})$. The shaded region represents the Wigner-Seitz unit cell. Right: Reciprocal lattice for the triangular one, $\mathbf{b}_1 = \frac{2\pi}{3a}(1, \sqrt{3})$ and $\mathbf{b}_2 = \frac{2\pi}{3a}(1, -\sqrt{3})$ being the reciprocal primitive vectors. The first Brillouin zone (FBZ) is shaded and the high-symmetry points $\mathbf{\Gamma} = (0, 0)$, $\mathbf{M} = \frac{2\pi}{3a}(1, 0)$, $\mathbf{K} = \frac{2\pi}{3a}(1, 1/\sqrt{3})$, and $\mathbf{K}' = \frac{2\pi}{3a}(1, -1/\sqrt{3})$ are highlighted. The $\mathbf{\Gamma} - \mathbf{M} - \mathbf{K} - \mathbf{\Gamma}$ path [dashed (red) line] is a high-symmetry one.

invariant under any translation $\mathbf{R} \in L$ with

$$L = \{n_1\mathbf{a}_1 + n_2\mathbf{a}_2 : n_1, n_2 \in \mathbb{Z}\}, \tag{3.2.15}$$

where the set L, defined in terms of the two primitive vectors $\mathbf{a}_1$ and $\mathbf{a}_2$, contains all the real-space lattice vectors. Consequently, we can define the reciprocal lattice as a periodic structure invariant under translations $\mathbf{K} \in RL$ with

$$RL = \{n_1\mathbf{b}_1 + n_2\mathbf{b}_2 : n_1, n_2 \in \mathbb{Z}\}, \tag{3.2.16}$$

where $\mathbf{b}_1$ and $\mathbf{b}_2$ are the reciprocal primitive vectors, defined by the relation $\mathbf{a}_i \cdot \mathbf{b}_j = 2\pi\delta_{ij}$ $(i, j = 1, 2)$ [1]. Some examples of Bravais and corresponding reciprocal lattices are presented in Figs. 3.3 and 3.4.

The condition for the existence of an eigenstate, i.e., $\det(\mathbb{M}) = 0$ [Eq. (3.2.10)], implies that the homogeneous system

$$\sum_{i=1}^{\infty} \mathbb{M}_{ji} D_i = 0, \qquad j = 1, 2, \cdots, \infty, \tag{3.2.17}$$

associated with the inhomogeneous one of Eq. (3.2.8) admits a nontrivial solution. Note that the number of scatterers N, and thus the number of equations and unknowns in the system, is now infinite [126–128]. In such a periodic structure Bloch's theorem holds [1], implying that

$$D_i = D_j e^{i\mathbf{q}\cdot(\mathbf{r}_j - \mathbf{r}_i)}, \tag{3.2.18}$$

where $\mathbf{q}$ is a vector of the first Brillouin zone (FBZ) in reciprocal space. Resorting to this property all the equations of the homogeneous system (3.2.17) become identical, so that the unique condition to verify is

$$\ln\left(\frac{e^\gamma}{2} k a_{2D}^{\text{eff}}\right) - i\frac{\pi}{2} + \sum_{\mathbf{R}\in L^*} \frac{\pi\hbar^2}{m} g_0(\mathbf{R}) e^{i\mathbf{q}\cdot\mathbf{R}} = 0, \tag{3.2.19}$$

where $L^* = L \setminus \{0\}$. Due to the slow convergence of the sum in Eq. (3.2.19), a rewriting of the equation in terms of reciprocal-lattice vectors is appropriate. The delicate details of this transformation are reported in the App. D.1, the result being

$$C_\infty + \ln\left(\frac{e^\gamma}{2}\right) + \frac{2\pi}{\mathcal{A}}\frac{1}{k^2 - q^2} \quad + \frac{2\pi}{\mathcal{A}}\sum_{\mathbf{K}\in RL^*}\left(\frac{1}{k^2 - |\mathbf{K}-\mathbf{q}|^2} + \frac{1}{K^2}\right) + \alpha = 0. \tag{3.2.20}$$

Here C_∞ is a coefficient depending only on the geometry of the Bravais lattice; its origin and definition follow from the real-to-reciprocal lattice transformation, presented in the App. D.1. Its numerical determination for the lattices treated in this work is discussed in the App. D.1.1. In Eq. (3.2.20), $\mathcal{A}$ is the area of the real-space unit cell of the Bravais lattice and we have also reintroduced the 2D interaction coefficient $\alpha = \ln(a_{2D}^{\text{eff}}/a)$, ($a$ being an arbitrary unit of length).

It is worth noting that Eq. (3.2.20) can be cast as

$$f(\mathbf{q}, E) = -\alpha, \tag{3.2.21}$$

with the introduction of the interaction-independent function

$$f(\mathbf{q}, E) = C_\infty + \ln\left(\frac{e^\gamma}{2}\right) + \frac{2\pi}{\mathcal{A}}\frac{1}{k^2 - q^2} + \frac{2\pi}{\mathcal{A}}\sum_{\mathbf{K}\in RL^*}\left(\frac{1}{k^2 - |\mathbf{K}-\mathbf{q}|^2} + \frac{1}{K^2}\right). \tag{3.2.22}$$

It follows by its definition that $f(\mathbf{q}, E)$ diverges for

$$k = |\mathbf{K} - \mathbf{q}| \qquad \forall\, \mathbf{K} \in RL, \tag{3.2.23}$$

recalling that wave vector and energy of the MW are related by $E = \hbar^2 k^2/2m$. Furthermore, $f(\mathbf{q}, E)$ is monotonically decreasing in E between two divergences, ensuring that for a given $\mathbf{q}$ only *one* solution of Eq. (3.2.21) exists between them. Another remarkable consequence is that if Eq. (3.2.23) holds, then condition (3.2.21) is satisfied only for $|\alpha| \to \infty$, which is in the limit of noninteraction between the MW and the scatterers (for a practical example, cf. Fig. 3.6 below). This implies that for $|\alpha| \to \infty$ (i.e., in the limit of weak $A-B$ interaction) one would recover the dispersion relation of a free MW, whose energy is given by

$$E_{\text{free}} = \frac{\hbar^2}{2m}|\mathbf{K} - \mathbf{q}|^2 \qquad \forall\, \mathbf{K} \in RL. \tag{3.2.24}$$

3.2.3.2 Non-Bravais lattices

This section is devoted to generalizing the formalism introduced in Sec. 3.2.3.1 to the case in which B scatterers are arranged in a non-Bravais lattice: an infinite periodic structure in which a unit cell, now containing M atoms, is repeated to cover the 2D plane. Such a structure can be

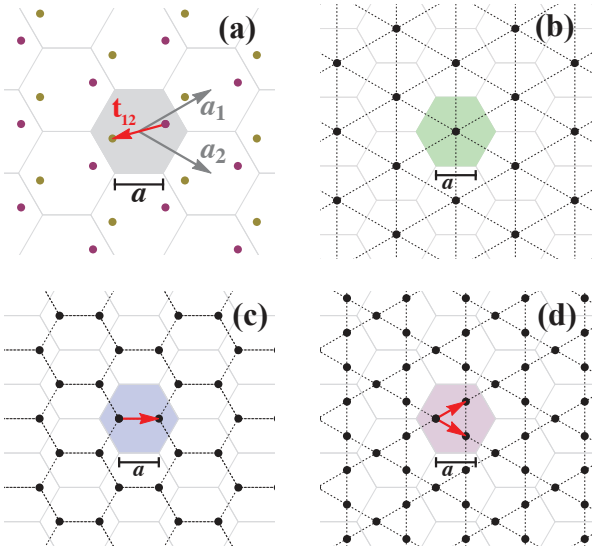

Figure 3.5 : (a) Representation of an $M = 2$ non-Bravais lattice. It can be seen as a triangular lattice (Fig. 3.4) with two atoms per unit cell (shaded hexagon) whose relative position is $\mathbf{t}_{12}$. Equivalently, it can be obtained as the superposition of two interpenetrating triangular lattices (distinguished by colors) displaced by $\mathbf{t}_{12}$ with respect to each other. The generating vectors $\mathbf{a}_{1,2} = \frac{3a}{2}(1, \pm 1/\sqrt{3})$ are also indicated. (b) Representation of the triangular lattice as an example of a basic Bravais lattice, i.e., with *one* atom per unit cell. The distance between nearest atoms is $a\sqrt{3}$. (c) Representation of the hexagonal lattice of graphene, a *two*-atom non-Bravais lattice based on the triangular one, obtained for $\mathbf{t}_{12} = (\mathbf{a}_1 + \mathbf{a}_2)/3 = (a, 0)$. With these definitions, the side of the hexagons has length a. (d) Representation of the kagomé lattice, a *three*-atom non-Bravais lattice based on the triangular one, obtained for $\mathbf{t}_{12} = \mathbf{a}_1/2$ and $\mathbf{t}_{13} = \mathbf{a}_2/2$. The nearest-neighbor distance is $a\sqrt{3}/2$.

equivalently seen as a set of M identical Bravais lattices, the mth and nth being displaced by $\mathbf{t}_{mn}$ with respect to each other. The structure will still be invariant if translated by $\mathbf{R} \in L$ [Eq. (3.2.15)], where $\mathbf{a}_{1,2}$ are the primitive vectors of a sublattice [cf. Fig. 3.5(a)]. All the properties of a Bravais lattice remain separately valid for each sublattice. If we denote by $\mathbf{R}_i$ the central position of the ith unit cell, and by $\boldsymbol{\rho}_m$ the position of the mth atom with respect to this reference, the location of a scatterer in the non-Bravais lattice is given by $\mathbf{r}_{im} = \mathbf{R}_i + \boldsymbol{\rho}_m$. The linear system, (3.2.17), becomes

$$\sum_{i=1}^{\infty} \sum_{m=1}^{M} \mathbb{M}_{jn,im}\, D_{im} = 0 \tag{3.2.25}$$

for each $j = 1, 2, \cdots, \infty$ and $n = 1, 2, \cdots, M$. Practically, each index has been split with respect to previous notation (i.e., $j \to jn$ and $i \to im$) such that the first index runs on the lattice cells, while the second indicates at which of the M sublattices the scatterer belongs. Accordingly, the definition of $\mathbb{M}$ given in Eq. (3.2.9) still holds. Bloch's theorem is now separately valid for each sublattice, so that

$$D_{im} = D_{jm}\, e^{i\mathbf{q}\cdot(\mathbf{r}_{jm} - \mathbf{r}_{im})} = D_{jm}\, e^{i\mathbf{q}\cdot(\mathbf{R}_j - \mathbf{R}_i)}, \tag{3.2.26}$$

while D_{im} and D_{jn} stay independent for $m \neq n$ [128]. This assumption makes the present treatment not valid in the few accidental cases in which the non-Bravais lattice degenerates into a Bravais

one. For an arbitrary choice of j, all the equations in system ,(3.2.25), take the form

$$\sum_{m=1}^{M} D_{jm} \sum_{i=1}^{\infty} \mathbb{M}_{jn,im}\, e^{i\mathbf{q}\cdot(\mathbf{R}_j-\mathbf{R}_i)} = 0, \tag{3.2.27}$$

giving a homogeneous system of M equations in the M unknowns D_{jm}, whose matrix $\mathbb{T}$ is defined by

$$\mathbb{T}_{nm} = \sum_{i=1}^{\infty} \mathbb{M}_{jn,im}\, e^{i\mathbf{q}\cdot(\mathbf{R}_j-\mathbf{R}_i)}. \tag{3.2.28}$$

The matrix elements read explicitly

$$\mathbb{T}_{nm} = \sum_{R\in L} \frac{\pi\hbar^2}{m}\, g_0(\mathbf{R}+\mathbf{t}_{nm})\, e^{i\mathbf{q}\cdot\mathbf{R}} \qquad \text{for } n\neq m, \tag{3.2.29a}$$

$$\mathbb{T}_{nn} = \ln\left(\frac{e^\gamma}{2}\, k a_{\mathrm{2D}}^{\mathrm{eff}}\right) - i\frac{\pi}{2} + \sum_{\mathbf{R}\in L^*} \frac{\pi\hbar^2}{m}\, g_0(\mathbf{R})\, e^{i\mathbf{q}\cdot\mathbf{R}}, \tag{3.2.29b}$$

with $\mathbf{t}_{nm}=\boldsymbol{\rho}_n-\boldsymbol{\rho}_m$. The condition

$$\det(\mathbb{T}) = 0 \tag{3.2.30}$$

has to be satisfied so that system (3.2.27) has a solution, which, in turn, means that this is the condition for the existence of an eigenstate of the A-atom MW in presence of a non-Bravais lattice of B scatterers. Note that the diagonal terms are all the same and that they correspond to the left-hand side of Eq. (3.2.19). This naturally implies that for $M=1$ we get back to the case of a Bravais lattice: $\det(\mathbb{T})=\mathbb{T}_{11}=0$ is exactly Eq. (3.2.19). It is again convenient to rewrite the sums in terms of reciprocal-lattice vectors. Following the procedure described in App. D we finally have

$$\mathbb{T}_{nm} = \frac{2\pi}{\mathcal{A}} \sum_{\mathbf{K}\in RL} \frac{e^{i(\mathbf{K}-\mathbf{q})\cdot\mathbf{t}_{nm}}}{k^2-|\mathbf{K}-\mathbf{q}|^2}, \tag{3.2.31a}$$

$$\mathbb{T}_{nn} = C_\infty + \ln\left(\frac{e^\gamma}{2}\right) + \frac{2\pi}{\mathcal{A}}\frac{1}{k^2-q^2} + \frac{2\pi}{\mathcal{A}} \sum_{\mathbf{K}\in RL^*} \left(\frac{1}{k^2-|\mathbf{K}-\mathbf{q}|^2} + \frac{1}{K^2}\right) + \alpha. \tag{3.2.31b}$$

Besides, from the latter expressions the matrix $\mathbb{T}$ turns out to be explicitly Hermitian.

3.3 Square lattice

As a first example of AAC we consider B scaterers arranged in a square lattice of spacing a, for which the primitive vectors are simply $\mathbf{a}_1=a(1,0)$ and $\mathbf{a}_2=a(0,1)$. The reciprocal lattice and the FBZ are consequently defined, as illustrated in Fig. 3.3.

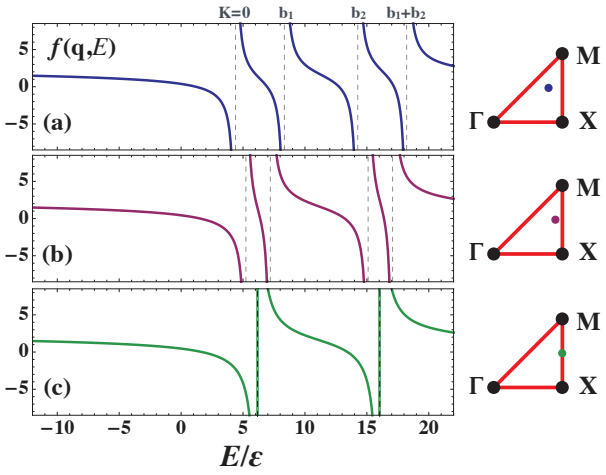

Figure 3.6 : For a square lattice, behavior of $f(\mathbf{q}, E)$ [Eq. (3.2.22)] as a function of E for different values of $\mathbf{q}$ [namely, $\frac{\pi}{a}(0.8, 0.5)$, $\frac{\pi}{a}(0.9, 0.5)$, and $\frac{\pi}{a}(1, 0.5)$, from top to bottom]. Dashed vertical (gray) lines represent the lowest values of E_{free} for the selected $\mathbf{q}$. In the sketches at the right of each panel a point indicates the corresponding $\mathbf{q}$ inside the $\mathbf{\Gamma}-\mathbf{X}-\mathbf{M}-\mathbf{\Gamma}$ symmetry path. Here $\varepsilon = \hbar^2/ma^2$.

3.3.1 Periodic system

To study the band structure of the artificial atomic square lattice (AASL) one needs to solve Eq. (3.2.20), where in this case $C_\infty \simeq 1.4265$ (cf. Appendix D.1.1). It is computationally convenient to evaluate once for all the function $f(\mathbf{q}, E)$ defined in Eq. (3.2.22) and look afterwards for solutions of Eq. (3.2.21) for a given α. In Fig. 3.6 we plot $f(\mathbf{q}, E)$ for different values of $\mathbf{q}$ inside the FBZ. As expected, f diverges each time that $E = E_{\text{free}}$ [i.e., when condition (3.2.23) is satisfied], but when $\mathbf{q}$ gets closer to the boundary of the FBZ some values of E_{free} corresponding to different $\mathbf{K}$ eventually tend to each other. A solution of Eq. (3.2.21) thus remains "trapped" in the small corridor formed by the two divergences and it tends to $E = E_{\text{free}}$ in the degeneracy limit, independently of α.

We present in Fig. 3.7 the spectrum and density of states (DOS) of the AASL for $\alpha = -0.75$. The spectrum is evaluated along the $\mathbf{\Gamma}-\mathbf{X}-\mathbf{M}-\mathbf{\Gamma}$ symmetry path (cf. inset). The free-MW energy E_{free} is also shown and, as expected, only one solution of Eq. (3.2.21) exists between two (eventually coinciding) free bands. An omnidirectional gap is found in the band structure and, correspondingly, in the DOS. The numerical evaluation of the DOS can be obtained by sampling each energy band in N_s points within the FBZ. Subsequently the formula

$$\text{DOS}(E) = \frac{N_E}{N_s \delta E} \tag{3.3.1}$$

gives the DOS in the energy range $(E, E + \delta E)$, being N_E the number of sampled energies falling in the energy interval. The DOS defined in Eq. (3.3.1) is normalized to the number of bands taken into account. Finally we remark that the lowest, isolated band lays entirely at negative energies for this value of α, meaning that the MW Bloch states are actually bound.

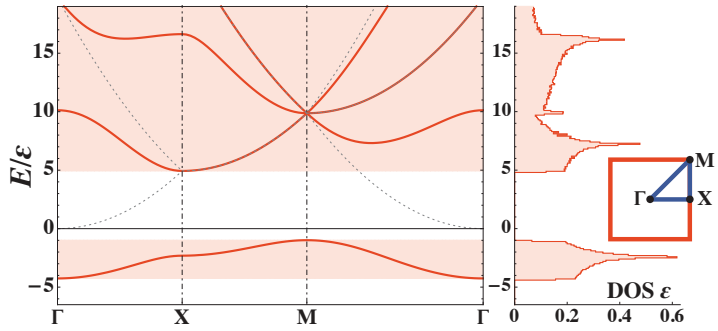

Figure 3.7 : For the artificial atomic square lattice, the band structure (left) and density of states (right) evaluated at $\alpha = -0.75$. Left: The four lowest energy bands are evaluated along the irreducible symmetry path $\mathbf{\Gamma}-\mathbf{X}-\mathbf{M}-\mathbf{\Gamma}$ within the first Brilouin zone (see inset). Dashed (gray) lines correspond to the energy spectrum of a free matter wave. Right: Density of states (DOS) obtained by evaluating the energies of the same bands in $N_s \simeq 6100$ points sampled inside the path. For each bin of the histogram (of width $\delta E = 0.1\varepsilon$, $\varepsilon = \hbar^2/ma^2$) the band-normalized DOS is evaluated according to Eq. (3.3.1).

A fundamental aspect of our model relies on the possibility of tuning its physical properties by acting on α. This remarkable feature is shown in Fig. 3.8, where the spectra of the AASL are compared for different values of α. The most evident modification concerns the lowest band, which is isolated for $\alpha \lesssim 0.7453$, so that a gap opens in the spectrum. Furthermore, the band becomes increasingly deep and flat, leading to low group velocities for the corresponding eigenstates. For $|\alpha| \gg 1$, the MW and scatterers are weakly interacting and, as expected, the band structure tends to the free-MW spectrum [dashed (grey) curves in Fig. 3.8].

3.3.2 Finite-size effects

In Sec. 3.3.1 we have considered the ideal periodic square lattice, but for both theoretical and practical interests it is crucial to investigate the robustness of the above-reported results for realistic finite-size systems. In this case one cannot resort to Bloch's theorem and the use of the general approach presented in Sec. 3.2.2 is necessary. In a typical experimental setup, atomic clouds can be manipulated in OLs extending over ∼60 sites per dimension. This means that 2D artificial atomic lattices with $\sim 10^3$ trapped B scatterers are experimentally realizable. In Fig. 3.9 we thus present the density of states on the $[\alpha, E]$ plane for a finite system of ∼2500 scatterers arranged in a square lattice inside a circular region of radius $R = 26a$. The finite-size results are compared here with those of an ideal infinite system and the agreement is excellent.

In the evaluation of the DOS in Fig. 3.9 it is computationally convenient to fix E and, correspondingly, look for the values of α satisfying conditions (3.2.13) or (3.2.14). For $E < 0$ the $N \times N$

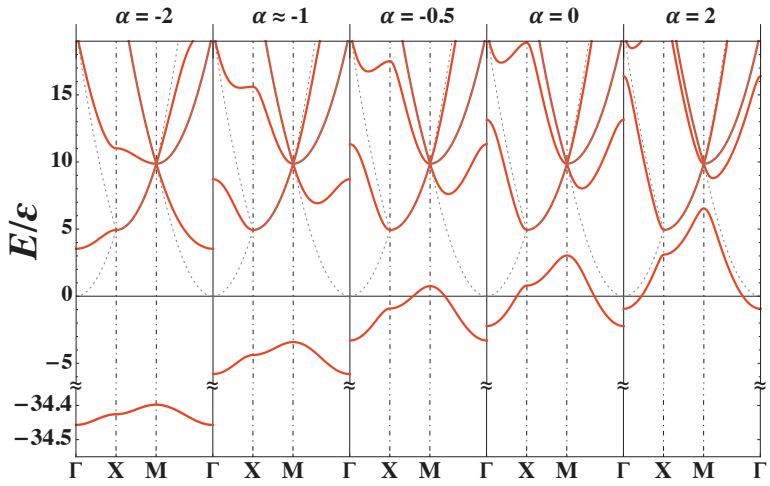

Figure 3.8 : Square lattice: band structure for different values of the interaction parameter α. Spectra are evaluated along the same path shown in Fig. 3.7. Dashed (gray) lines correspond to the energy spectrum of a free matter wave. Energies are normalized on $\varepsilon = \hbar^2/ma^2$.

real symmetric matrix $\mathbb{M}^o(E)$ and its eigenvalues can be evaluated, thus the values of α solving Eqs. (3.2.13) are immediately obtained. For $E > 0$ one can use $\tilde{E} = E$ as the starting point to find an approximate solution of the complex Eqs. (3.2.14). We write $z = \tilde{E} + \delta z$ and we assume the first-order expansion $m_i^o(z) = m_i^o(\tilde{E}) + \delta z\, m_i^{o\prime}(\tilde{E})$ to be valid. By choosing $\alpha = -\,\mathrm{Re}[m_i^o(\tilde{E})]$ each equation reduces to $i\,\mathrm{Im}[m_i^o(\tilde{E})] + \delta z\, m_i^{o\prime}(\tilde{E}) = 0$, from which δz can be directly derived. The energy E and band-width Γ of the quasi-Bloch states follow from

$$z = E - i\frac{\hbar}{2}\Gamma \simeq \tilde{E} - i\frac{\mathrm{Im}[m_i^o(\tilde{E})]}{m_i^{o\prime}(\tilde{E})}. \tag{3.3.2}$$

Note that the derivative $m_i^{o\prime}(\tilde{E})$ can be evaluated resorting to the generalized Hellmann-Feynman theorem [124]: for the complex symmetric matrix $\mathbb{M}^o$, one has $dm_i^o(z)/dz = \vec{u}_i \cdot [d\mathbb{M}^o(z)/dz]\,\vec{u}_i$, where $\vec{u}_i$ is the right eigenvector of eigenvalue $m_i^o(z)$, normalized as $\vec{u}_i \cdot \vec{u}_i = 1$ (instead of the usual $\vec{u}_i \cdot \vec{u}_i^* = 1$).

The first order approximation (3.3.2) is sufficient if $\mathrm{Im}[m_i^o(\tilde{E})]$ is small [124], and this is the case for most of the solutions we find. In particular, for quasi-Bloch states one expects a lifetime $\tau = 1/\Gamma \simeq R/v_g$, where R is the radius of the region containing the scatterers and v_g the group velocity of the state. To verify this behavior we selected a small window on the $[\alpha, E]$ plane, studying the distributions of τ when the system size varies. The results of this analysis are presented in Fig. 3.10. We find that the distribution peak follows the expected behavior, confirming that the first-order approximation is sufficient to individuate quasi-Bloch states. Nevertheless, when the poles of G are evaluated by Eq. (3.3.2), one can eventually find some results for which the first-

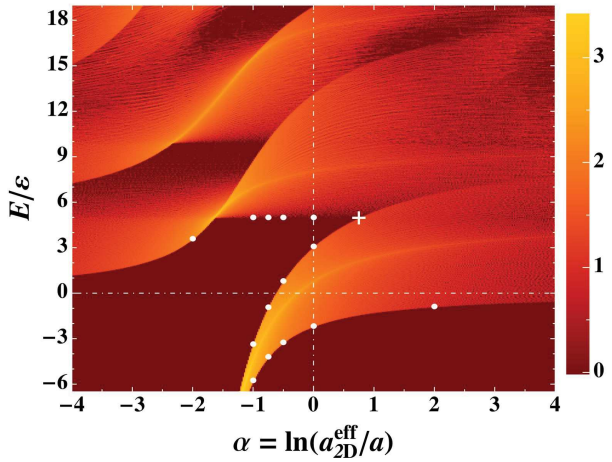

Figure 3.9 : Finite-sized square lattice: DOS per scatterer in the plane $[\alpha, E/\varepsilon]$ for a system of $N = 2551$ scatterers arranged in a square lattice inside a disk of radius $R = 26a$. Energies are discretized with a step of 0.01ε ($\varepsilon = \hbar^2/ma^2$). For a given $E < 0$ all N solutions of Eqs. (3.2.13) are selected. For $E > 0$ the sampled values are used as starting points to find N complex poles of G according to Eq. (3.3.2). Only quasi-Bloch bulk states are selected, as explained in the text. The color map is applied to $\log_{10}(\frac{N_p}{N}\frac{\varepsilon}{\delta\alpha\,\delta E})$, where N_p is the number of selected poles of G within a rectangular bin of area $\delta\alpha\,\delta E$ ($\delta\alpha = 0.02$ and $\delta E = 0.05\varepsilon$). White circles indicate the positions of band boundaries as expected from the analysis of an infinite system (Figs. 3.7 and 3.8). Analogously, the white plus symbol marks the expected contact point between the lowest and the first excited band, corresponding to the gap closure.

order is insufficient. These solutions would present nonphysical negative values of Γ and needs to be rejected (in the case presented in Fig. 3.9 they constituted 10.6% of positive-energy states). Furthermore, in a finite-size system, states other than quasi-Bloch ones can appear (such as edge states) for which the law $\Gamma \simeq v_g/R$ is not valid. In order to tell them apart one can look at the density of Γ, shown in Fig. 3.11 for the same system considered in Fig. 3.9. A neat change in the behavior is found in $\Gamma_{\max} \sim v_{g\,\max}/R$, where $v_{g\,\max}$ is the highest estimated group velocity in the range of E and α considered. States with $\Gamma > \Gamma_{\max}$ can in turn be rejected, finally, leaving only solutions behaving as quasi-Bloch bulk states (in the case of Fig. 3.9 this led to the exclusion of an additional 8.4% of solutions). A natural question may arise concerning the dependence of $v_{g\,\max}$ on α and E. It has been verified that by considering a cutoff depending on α and E the results are qualitatively the same as those obtained using the aforementioned selection method.

3.3.3 Introduction and effects of disorder

A remarkable advantage of our atomic artificial lattices with respect to other one-species models is the possibility of naturally introducing disorder in the system. Loading the B-atom OL with

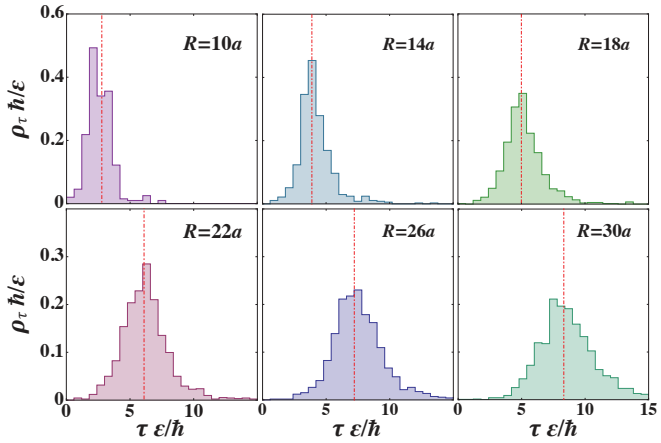

Figure 3.10 : Square lattice of finite size: normalized densities of lifetimes τ for $E/\varepsilon = 6.5 \pm 0.5$ and $\alpha = -0.75 \pm 0.1$ ($\varepsilon = \hbar^2/ma^2$). Different panels correspond to different radii R of the scattering region. Dot-dashed vertical (red) lines in each panel indicate $R/\bar{v}_g$, where $\bar{v}_g$ is the average group velocity in the selected region of the $[\alpha, E]$ plane.

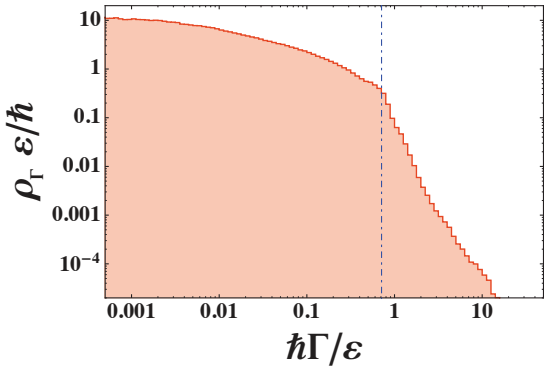

Figure 3.11 : For the same finite-size square lattice considered in Fig. 3.9: normalized density of bandwidths Γ for all positive-energy poles of the Green function ($\varepsilon = \hbar^2/ma^2$). The dot-dashed vertical (blue) line at $\Gamma = \Gamma_{\max}$ marks the change in behavior of the density ρ_Γ. Solutions with $\Gamma > \Gamma_{\max}$ have been rejected because they are incompatible with the behavior of a quasi-Bloch bulk state. Here we found $\Gamma_{\max} \simeq 0.7\varepsilon/\hbar$ (i.e., $\Gamma_{\max} \simeq 2$kHz for a matter wave of ^{87}Rb atoms in an AASL with $a = 500$nm).

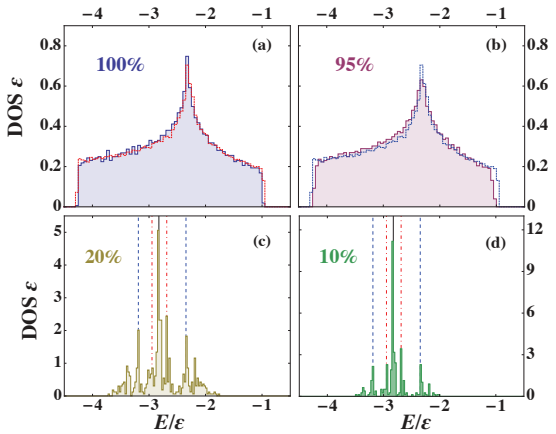

Figure 3.12 : Disordered square lattice: normalized negative-energy DOS at $\alpha = -0.75$ for an AASL of radius $R = 32a$, corresponding to 3209 available lattice sites. Different panels refer to different percentages of randomly occupied sites: (a) 100%, (b) 95%, (c) 20%, (d) 10%. Histograms are obtained with a bin size $\delta E = 0.05\varepsilon$ in (a) and (b) and $\delta E = 0.025\varepsilon$ in (c) and (d). Superimposed dotted histograms in (a) and (b) represent the DOS for an infinite periodic system. Vertical lines in (c) and (d) indicate the energies of few-body bound states: AB dimer [solid (black) lines], AB_2 trimer with B atoms separated by a [dashed (blue) line] and $a\sqrt{2}$ [dot-dashed (red) lines]. Here $\varepsilon = \hbar^2/ma^2$.

nonunitary filling would result in the presence of randomly unoccupied sites constituting random defects in the artificial crystal [129]. Our general theoretical approach, presented in Sec. 3.2.2, can be used to investigate the effects of this kind of disorder. In particular, we show in Fig. 3.12 the negative-energy DOS of an AASL of radius $R = 32a$ at different filling factors, obtained fixing $\alpha = -0.75$. In Fig. 3.12 (a) 100% of the sites are occupied and finite-size effects can be investigated by comparing the DOS with that of the periodic system (presented in Fig. 3.7). There are no significant discrepancies between the two quantities, confirming the robustness of the results with respect to the system size. The DOS in the presence of 5% of vacant sites [Fig. 3.12 (b)], appears in turn to be compatible with the results for an ideal periodic system, thus proving robustness also against a small number of vacancies. For a large number of unoccupied sites, instead, the periodicity of the lattice gets lost and the MW interacts locally with few-body clusters of scatterers. An atom A can get trapped by an isolated B scatterer, thus forming an AB dimer. Similarly, it can form an AB_2 trimer in the vicinity of a couple of B atoms, and so on so forth for larger clusters. As shown in Fig. 3.12 (c) and 3.12 (d), this gives rise to a DOS which is more and more peaked around the energies of few-body AB_n bound states. The energies of these bound states can be derived from Eqs. (3.2.13), where the eigenvalues of $\mathbb{M}^o$ can be analytically obtained for $n \leq 4$. The explicit expressions can be found in Eqs. (45) and (46) in [124], where the emergence of disorder-localized states for low filling is investigated.

3.4 Triangular lattice

Another relevant example of atomic artificial Bravais lattice is the triangular one, whose analysis is also preliminary to the study of intriguing non-Bravais structures, such as graphene and the kagomé lattice. In this case the primitive vectors are $\mathbf{a}_1 = a(\sqrt{3}, 1)\sqrt{3}/2$ and $\mathbf{a}_2 = a(\sqrt{3}, -1)\sqrt{3}/2$, from which the real and reciprocal lattices, illustrated in Fig. 3.4, are defined.

To investigate the spectral properties of the atomic artificial triangular lattice (AATL) we need, once again, to solve Eq. (3.2.21), now for $C_\infty \simeq 0.9597$ (cf. Appendix D.1.1). We can thus proceed as in Sec. 3.3.1 for the square lattice. In Fig. 3.13 we present a typical spectrum of the system, evaluated in $\alpha = -0.6$. The band structure, studied along the $\mathbf{\Gamma}-\mathbf{M}-\mathbf{K}-\mathbf{\Gamma}$ high-symmetry path (see inset), shows the presence of a gap, which the DOS confirms to be omnidirectional. Also in this case we verify the existence of a single solution of Eq. (3.2.21) between two values of E_{free}. The versatility of this artificial lattice emerges in Fig. 3.14, where we compare its spectra for different values of the interaction parameter α. One finds that there exists a gap of tunable width for $\alpha \lesssim 3.853$, and again, the lowest, isolated band rapidly becomes thin and deep in energy with decreasing α.

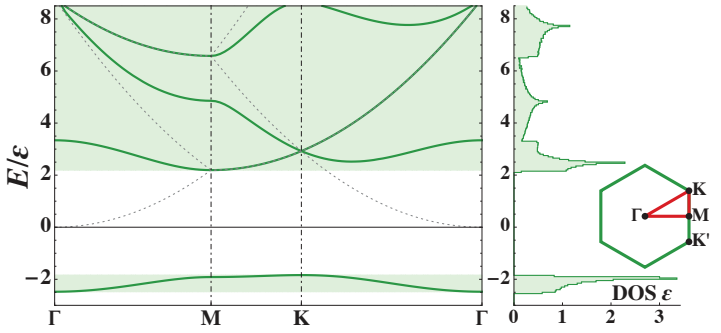

Figure 3.13 : Artificial atomic triangular lattice: band structure (left) and DOS (right) for $\alpha = -0.6$. Left: Behavior of the four lowest energy bands along the **Γ**–**M**–**K**–**Γ** path (see inset at right). Dashed (gray) lines indicate the dispersion relation for a free matter wave. Right: DOS, as defined in Eq. (3.3.1), obtained by evaluating the energy of the bands in $N_s = 7600$ points sampled inside the aforementioned symmetry path. The bin size of the histogram is $\delta E = 0.05\varepsilon$ ($\varepsilon = \hbar^2/ma^2$).

For the sake of completeness we again test our results against finite-size effects. With the same method illustrated in Sec. 3.3.2 we evaluated the DOS on the plane $[\alpha, E]$ for an experimental-size system of ∼2100 scatterers arranged in a triangular lattice inside a circular region of radius $R = 42a$. The results, shown in Fig. 3.15, are, once again, in good agreement with predictions based on the analysis of an ideal AATL. We also verified that, in analogy to the square-lattice case, the results are robust if a small number of vacancies is randomly introduced in the triangular structure, while few-body states become dominant for low fillings.

3.5 Atomic artificial graphene

Due to the fundamental role of carbon in biological systems, the investigations of physical properties of its allotropes has always raised great interest. This is the case for graphene, which is a flat monolayer of carbon atoms arranged in a 2D honeycomb lattice [37, 38], as represented in Fig. 3.5 (c). The experimental isolation of graphene in 2004 [36] pushed out of the mere academic interest the study of this intriguing material, with particular interest to the outstanding transport properties of charge carriers. These follow from the peculiar band structure of electrons: conduction and valence bands touch in isolated points of the k space, around which the energy-momentum dispersion relation is conical. In such a scenario the Schrödinger' equation fails to describe the particles' behavior, ruled by a Dirac-like equation for massless fermions. The group velocity $v_g \simeq 10^6$m/s of these particles around the Dirac cone plays the role of an effective speed-of-light of the charge carriers. This intriguing scenario allows for the investigation of quantum electrodynamics in benchtop experiments [37].

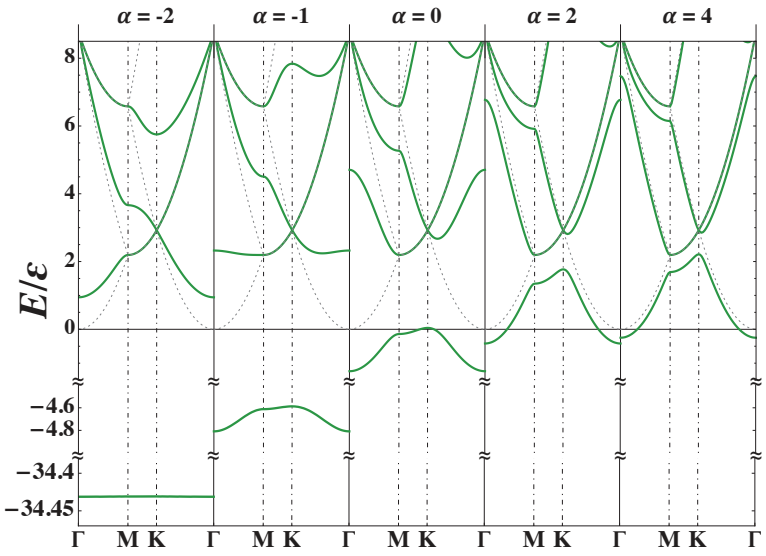

Figure 3.14 : Triangular lattice: comparison of the band structure for different values of the interaction parameter α. The spectrum evaluation path is the same as for Fig. 3.13. Dashed (gray) lines correspond to the energy spectrum of a free matter wave. Energies are normalized on $\varepsilon = \hbar^2/ma^2$.

The interest towards these amazing properties led to the realization of several kinds of artificial graphene: systems whose geometrical symmetries allow for the appearance of Dirac singularities (for a recent review, see [39]). Among these we find nano-structured surfaces on which hexagonal patterns are impressed [130, 131] and molecular graphene, obtained by accurately depositing molecules on a substrate [132]. Microwave analogs of graphene can also be implemented making use of honeycomb lattices of dielectric resonators [133]. As discussed throughout Chapter 1, ultracold gases in OLs revealed themselves as a powerful and versatile tool in the domain of quantum simulation, due to the wide and precise tunability of interparticle interactions and lattice geometries [20, 134]. Several theoretical approaches predict the existence of Dirac points in such kind of systems, analyzing also their motion and merging acting on experimental parameters [135, 136]. These effects have been recently observed for a one-component ultracold Fermi gas [40]. The emergence of non-dispersive and non-isolated flat bands for cold-atoms in honeycomb lattices have also been predicted [137] and experimentally observed for polaritons [131].

Motivated by the increasing activity on this peculiar 2D material, it seemed natural to apply our model to the investigation of atomic artificial graphene (AAG). The case of AAG represents a useful benchmark for the theoretical model developed in Sec. 3.2.3.2 for non-Bravais lattices. The honeycomb lattice, indeed, comes from the superposition of two interpenetrating triangular lattices of primitive vectors $\mathbf{a}_1 = \frac{3a}{2}(1, 1/\sqrt{3})$ and $\mathbf{a}_2 = \frac{3a}{2}(1, -1/\sqrt{3})$ with relative displacement $\mathbf{t} = a\,(1, 0)$, as illustrated in Fig. 3.5 (c). Each unit cell have area $\mathcal{A} = 3\sqrt{3}a^2/2$ and the reciprocal

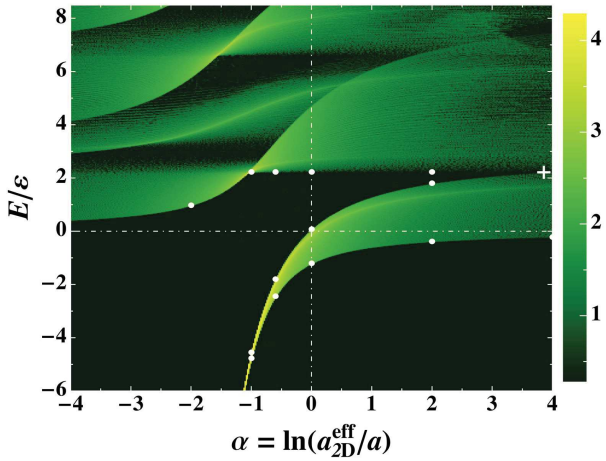

Figure 3.15 : Triangular lattice of finite size: DOS per scatterer in the plane $[\alpha, E/\varepsilon]$ for a system of $N = 2125$ scatterers arranged in a triangular lattice inside a disk of radius $R = 42a$. The same method as for Fig. 3.9 was used, but discretizing E in steps of 0.005ε ($\varepsilon = \hbar^2/ma^2$). Positive-energy quasi-Bloch bulk states were selected imposing $\Gamma < \Gamma_{\max} \simeq 0.3\varepsilon/\hbar$ (i.e., $\Gamma_{\max} \simeq 880$Hz for a matter wave of ^{87}Rb atoms in an AATL with $a = 500$nm). The color-map is applied to the quantity $\log_{10}(\frac{N_p}{N}\frac{\varepsilon}{\delta\alpha\,\delta E})$, where N_p is the number of selected poles of G within a rectangular bin of area $\delta\alpha\,\delta E$ ($\delta\alpha = 0.02$ and $\delta E = 0.025\varepsilon$). White circles indicate the expected positions of the band boundaries as evaluated for the infinite system (Figs. 3.13 and 3.14). Analogously, the white plus symbol marks the expected contact point between the lowest and the first excited band.

primitive vectors result $\mathbf{b}_1 = \frac{2\pi}{3a}(1, \sqrt{3})$ and $\mathbf{b}_2 = \frac{2\pi}{3a}(1, -\sqrt{3})$. Since the elementary building block is a triangular lattice, we use again $C_\infty \simeq 0.9597$ (cf. App. D.1.1).

3.5.1 Periodic system: Dirac cones and isolated flat band

As usual, we begin by considering an ideal infinite system. For a generic two-atom non-Bravais lattice the condition for the existence of an eigenstate is $\det(\mathbb{T}) = 0$ [Eq. (3.2.30)], the matrix $\mathbb{T}$ being a 2×2 hermitian one. Once again, the diagonal interaction term α can be isolated by writing $\mathbb{T} = \mathbb{T}^o + \mathbb{I}\alpha$, where $\mathbb{I}$ is the 2×2 identity matrix and

$$\mathbb{T}^o = \mathbb{T}(\alpha = 0) = \begin{pmatrix} f(\mathbf{q}, E) & \varphi(\mathbf{q}, E) \\ \varphi^*(\mathbf{q}, E) & f(\mathbf{q}, E) \end{pmatrix}, \tag{3.5.1}$$

with $f(\mathbf{q}, E)$ defined as in Eq. (3.2.22) and

$$\varphi(\mathbf{q}, E) = \frac{2\pi}{\mathcal{A}} \sum_{\mathbf{K}\in RL} \frac{e^{i(\mathbf{K}-\mathbf{q})\cdot\mathbf{t}}}{k^2 - |\mathbf{K}-\mathbf{q}|^2}. \tag{3.5.2}$$

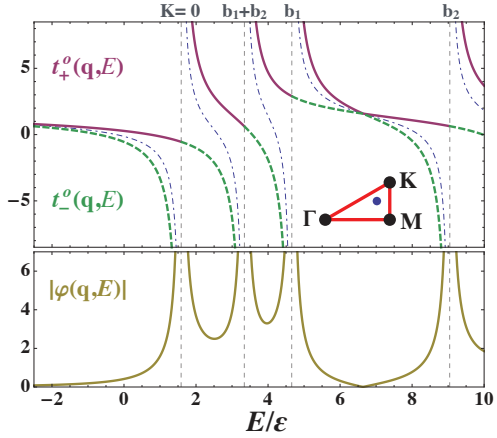

Figure 3.16 : Atomic artificial graphene. Top: Behavior of $t^o_+(\mathbf{q}, E)$ [solid (purple) line] and $t^o_-(\mathbf{q}, E)$ [dashed (green) line] as a function of E for $\mathbf{q} = \frac{2\pi}{3a}(0.8, 0.3)$. Dashed vertical (gray) lines indicates the lowest values of E_{free} for the selected $\mathbf{q}$. Dot-dashed (blue) curves show the behavior of $f(\mathbf{q}, E)$. Inset: position of $\mathbf{q}$ within the $\mathbf{\Gamma}$–$\mathbf{M}$–$\mathbf{K}$–$\mathbf{\Gamma}$ symmetry path (Fig. 3.4). Bottom: Behavior of $|\varphi(\mathbf{q}, E)|$ for the same $\mathbf{q}$. Here $\varepsilon = \hbar^2/ma^2$.

It follows that condition $\det(\mathbb{T}) = 0$ is equivalent to

$$t^o_\pm(\mathbf{q}, E) = f(\mathbf{q}, E) \pm |\varphi(\mathbf{q}, E)| = -\alpha, \tag{3.5.3}$$

where $t^o_\pm$ are the two real eigenvalues of $\mathbb{T}^o$. It can be easily proved that when f diverges, i.e., when $E \to E_{\text{free}}$, the absolute value of φ exactly cancels the divergence so that the left limit of t^o_+ is finite and equal to the right limit of t^o_-:

$$\lim_{E \to E^{\mp}_{\text{free}}} t^o_\pm(\mathbf{q}, E) = \lim_{E \to E_{\text{free}}} f(\mathbf{q}, E) - \frac{\pi\hbar^2}{m\mathcal{A}} \frac{1}{E - E_{\text{free}}}. \tag{3.5.4}$$

A numerical example of this is given in Fig. 3.16, where the two eigenvalues $t^o_\pm(\mathbf{q}, E)$ and $|\varphi(\mathbf{q}, E)|$ are plotted as functions of E for a fixed $\mathbf{q}$. By virtue of the aforementioned properties, only *one* solution of Eq. (3.5.3) exists between two solutions of the corresponding Eq. (3.2.21). This practically means that a band of a non-Bravais lattice with $M = 2$ is always included between two bands of the corresponding Bravais lattice ($M = 1$).

An example of a spectrum for the AAG is presented in Fig. 3.17. The band structure for $\alpha = -0.5$ is evaluated along an high-symmetry path in the k space of the honeycomb lattice, and is presented along with the corresponding DOS, numerically determined via Eq. (3.3.1). Band structure and DOS point out the presence of a double gap. A key feature is the existence of two nonequivalent Dirac points, situated in $\mathbf{K}, \mathbf{K}' = \frac{2\pi}{3a}(1, \pm 1/\sqrt{3})$ within the FBZ. Here the two lowest bands touch each other, creating a cone-shaped energy-momentum dispersion. The MW obeys there to a Dirac-like equation for relativistic massless fermions in which the role of the speed of light is played by v_g: the modulus of the group velocity of the wave along the cone. At higher energies we find an isolated band followed by a continuum of states.

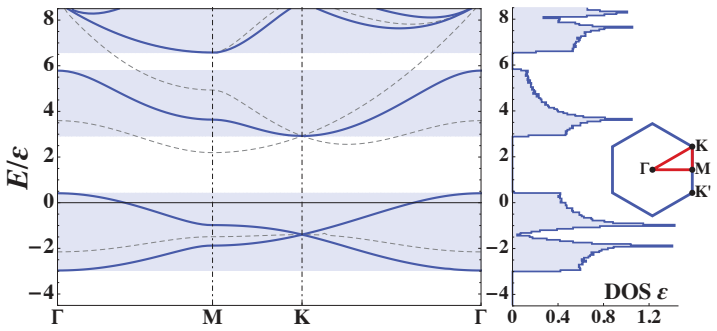

Figure 3.17 : Honeycomb lattice: band structure (left) and DOS (right) for the AAG at $\alpha = -0.5$. Left: Behavior of the five lowest energy bands along the irreducible symmetry path in the inset (at right). Dashed (gray) curves show the band structure for the corresponding triangular lattice. Right: DOS [defined in Eq. (3.3.1)] obtained by sampling the band energy in $N_s = 3300$ points within the symmetry path. The histogram bin size is $\delta E = 0.06\varepsilon$ ($\varepsilon = \hbar^2/ma^2$).

The remarkable tunability of the AAG emerges from Fig. 3.18, in which band structures corresponding to different values of α are compared. The gaps can be modulated and closed tuning the interaction strength. The two lowest bands, supporting the Dirac cone, move to negative energies for $\alpha \lesssim 0$, making the relativistic physics played now by states bounded in the system. Furthermore, similarly to the Bravais artificial lattices, the lowest bands get flat with decreasing α. The same two bands still touch only in the isolated points **K** and **K′**. It follows that the slope of the Dirac-cones walls decreases, leading to a reduction of the local group velocity v_g (Fig. 3.18, inset) remarkably down to $v_g \lesssim 1$mm/s, *i.e.*, 10^{-9} the value for real graphene. It is worth stressing that for $-2 < \alpha < -1$ the third band changes concavity, becoming completely flat around $E \simeq 2.924\varepsilon$ ($\varepsilon = \hbar^2/ma^2$) for $\alpha \simeq -1.631$. It may be argued that, also in the case of Bravais AACs, quasiflat bands emerge for large and negative values of α (see the lowest bands in Figs. 3.8 and 3.14), but some important differences between these bands and the one we find for AAG. At first, graphene's band is topologically flat, which means that $v_g = 0$ for every value of $\mathbf{q}$. The quasiflat bands, instead, keep their structure, even though they are compressed into a small range of energies (this phenomenon is clearly shown in Fig. 3.8). Moreover, graphene's flat band lies at positive energies, in the propagative region of the MW. Remarkably, differently from previously investigated graphene-like systems [131, 137], here the flat band results also isolated. The interest in this kind of flat band arises from its nondispersivity: for noninteracting A atoms (the case considered in this work), any MW state would be stationary and localized, the group velocity on the band being strictly zero. The effects of an eventual $A-A$ interaction, even if extremely small, would be enhanced, leading to the emergence of strongly correlated phases [137, 138]. Nonisolated flat bands have recently been observed in honeycomb lattices for polaritons [131].

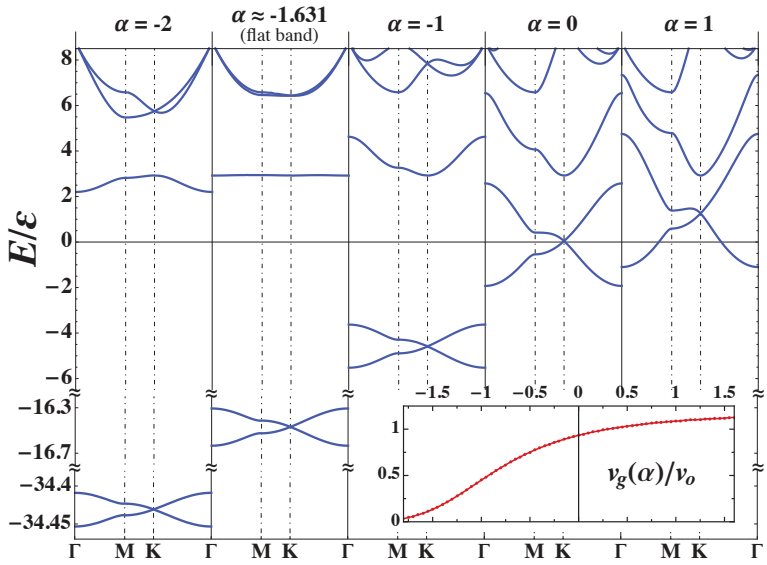

Figure 3.18 : Comparison of the band structures of the atomic artificial graphene for different values of α evaluated along the $\mathbf{\Gamma}-\mathbf{M}-\mathbf{K}-\mathbf{\Gamma}$ symmetry path (see inset of Fig. 3.17). For $\alpha \simeq 1.63$ the third, isolated band is topologically flat. The unit of energy is $\varepsilon = \hbar^2/ma^2$. Inset: Modulus of the group velocity v_g for an A-atoms matter wave around the Dirac's cone as a function of α. Speeds are normalized on $v_o = \hbar/ma$ ($\simeq 1.5$mm/s for MW of ^{87}Rb atoms in an OL with $a = 500$nm).

3.5.2 Distorted graphene: motion and merging of Dirac cones

Beside allowing to tune interactions, the use of cold atoms in optical lattices offers a large experimental control on the potential landscape. The effects of a distorted honeycomb potential have been investigated, both theoretically and experimentally, for one-component artificial graphene, i.e., in the presence of a single atomic species propagating through a periodic optical potential. For such systems, a deformation of the OL can lead to a displacement of the Dirac cones within the FBZ, eventually resulting in their merging and disappearance [135, 136]. Such a phenomenon have been recently pointed out experimentally for a Fermi gas [40]. In the case of our two-component AAG, a distorsion in the honeycomb arrangement of B scatterers is likely to induce similar effects.

We investigated the motion and merging of Dirac points in a triangular, $M = 2$ non-Bravais lattice, like those of Fig. 3.5 (c), considering different displacement vectors of the form $\mathbf{t} = \beta(a, 0)$. Note that the case $\beta = 1$ corresponds to the undistorted AAG. For $\alpha = -0.6$, we show in Fig. 3.19 the positions of the Dirac cones along the $\mathbf{\Gamma}-\mathbf{K}'-\mathbf{M}-\mathbf{K}-\mathbf{\Gamma}$ path, plotted taking β as parameter. For $\beta = 1$ we find, as expected, that the Dirac points lie at $\mathbf{K}$ and $\mathbf{K}'$. The cones depart vertically by increasing β, i.e., by pushing horizontally apart the scatterers within the unit cell. On the

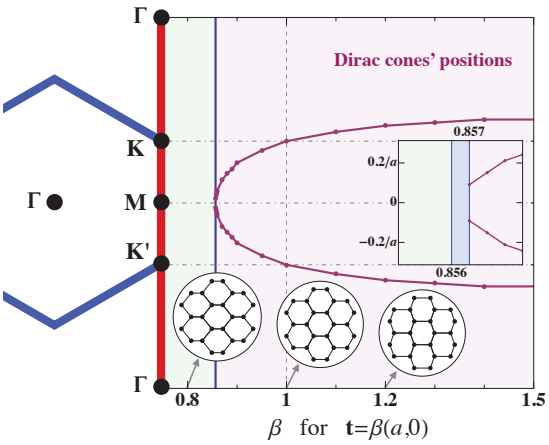

Figure 3.19 : For the atomic artificial honeycomb lattice [cf. Fig. 3.5 (c)] with displacement vector $\mathbf{t} = \beta(a, 0)$. We show, as a function of the parameter β, the position of the Dirac cones, if existing, along the $\mathbf{\Gamma} - \mathbf{K}' - \mathbf{M} - \mathbf{K} - \mathbf{\Gamma}$ path (highlighted in red at left, on a schematic representation of the first Brillouin zone). The present results have been obtained for $\alpha = -0.6$. Right, inset: Zoom-in around the merging region. The results show that the Dirac points meet and cancel each other in $\mathbf{M}$ for $\beta \sim 0.86$. Bottom, circular insets: Real-space arrangement of the scatterers in the honeycomb lattice for the indicated values of β: 0.8, 1 (i.e., undistorted graphene) and 1.2 from left to right.

other hand, for $\beta < 1$, the cones approach each other and merge in $\mathbf{M}$ for $0.856 < \beta < 0.857$ (see zoom-in in Fig. 3.19). The dispersion relation at the merging point shows the typical semi-Dirac behavior: it is parabolic along the merging direction but stays linear along the perpendicular one [136]. For smaller values of β, a gap is opened and Dirac points finally disappear. These features stay qualitatively the same if α is set to a different value.

As a technical comment we point out that the case $\beta = 1.5$ constitutes one of the few accidental cases in which the approach presented in Sec. 3.2.3.2 to describe non-Bravais lattices fails to describe the system. This is because, in this circumstance, the double-triangular non-Bravais lattice actually becomes a rectangular Bravais one, so that the corresponding Eq. (3.2.20) should be solved, instead of Eq. (3.2.30). For a Bravais lattice, the Bloch's theorem [Eq. (3.2.18)] connects all the amplitude coefficients D_i, while in its non-Bravais version [Eq. (3.2.26)] M subsets of coefficients D_{im} are left independent, being M the number of atoms in the unit cell. Such a choice adds unphysical solutions when a Bravais lattice is treated as a non-Bravais one. To conclude is worth noting that, for any arbitrary small deviation from the degeneracy point, the non-Bravais approach is meaningful, since such an infinitesimal distortion is periodically repeated infinite times in space, thus affecting the physics of the AAC.

3.5.3 Finite-size and disorder effects

A natural question concerns how and when the features of an ideal periodic AAG are modified if both finite-size and vacancy effects are considered. In the case of finite or disordered systems, the appropriate theoretical tools are those presented in Sec. 3.2.2, without distinction between Bravais and non-Bravais structures. Once the set $\{\mathbf{r}_{im}\}$ of the scatterers' positions is assigned, the method to find the DOS on the $[\alpha, E]$ plane is the same as those presented in details for the AASL in Sec. 3.3.2.

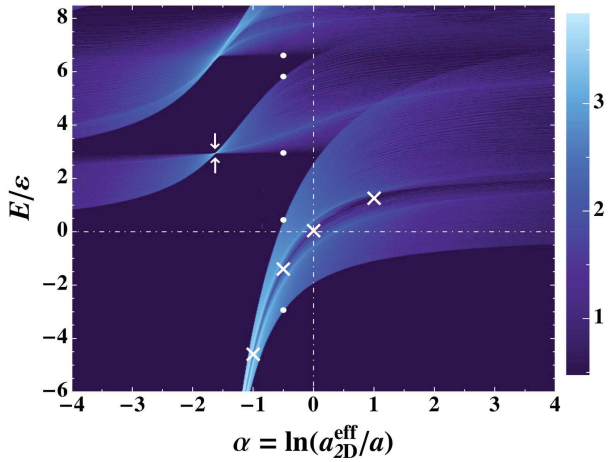

Figure 3.20 : Finite-sized atomic artificial graphene: DOS per scatterer in the plane $[E/\varepsilon, \alpha]$ for a system of $N = 2167$ scatterers arranged in a honeycomb lattice inside a disk of radius $R = 30a$. The same method as for Fig. 3.9 was used, but discretizing the energies with a step of 0.0025ε ($\varepsilon = \hbar^2/ma^2$). In the positive-energy region, we select the quasi-Bloch bulk states imposing $\Gamma < \Gamma_{\max} \simeq 0.2\varepsilon/\hbar$ (i.e., $\Gamma_{\max} \simeq 500$Hz for a matter wave of ^{87}Rb atoms in an honeycomb lattice with $a = 500$nm). The color map is applied to the quantity $\log_{10}(\frac{N_p}{N}\frac{\varepsilon}{\delta\alpha\,\delta E})$, where N_p is the number of selected poles of G within a rectangular bin of area $\delta\alpha\,\delta E$ ($\delta\alpha = 0.0125$ and $\delta E = 0.0125\varepsilon$). White crosses, circles, and arrows indicate, respectively, the positions of Dirac cones, gap boundaries, and the isolated flat band as expected from the analysis of the periodic system (Figs. 3.17 and 3.18).

In Fig. 3.20 we present the DOS as a function of E and α for a set of ~ 2000 scatterers. The features of the infinite system are already well reproduced, as can be inferred from a comparison with Figs. 3.17 and 3.18. The large dark areas, in which no states are allowed, exactly correspond to gaps in the infinite system. The expected boundaries of the gaps for $\alpha = -0.5$ are marked by white circles in Fig. 3.20. The fingerprint of the Dirac cone can be recognized in the thin dark region separating the two lowest bands. The expected positions of the cones, as deduced from the infinite-system results, are marked by white crosses. The existence of a flat band is confirmed in the finite-size system, and its position is in perfect agreement with predictions from the ideal honeycomb lattice, marked by arrows in Fig. 3.20. As a final remark we point out that, in the weak-interaction limit $|\alpha| \gg 1$, no states are allowed for $E < 0$ while the DOS tends to a constant for $E > 0$, as expected for a free MW in 2D. Another comparison between ideal and finite system is presented in Fig. 3.21 (a). Here, we compare the negative-energy DOS of the infinite and finite crystal calculated, in both cases, for $\alpha = -0.5$. The very good agreement between the two quantities shows, once again, the robustness of the Dirac cones with respect to finite-size effects.

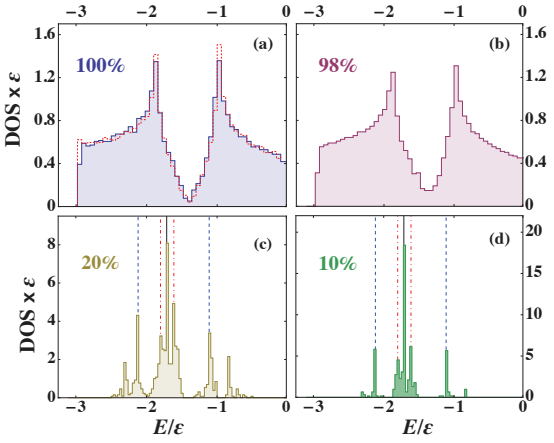

Figure 3.21 : Atomic artificial graphene: negative-energy DOS calculated for $\alpha = -0.5$ for an honeycomb lattice with $N = 3870$ sites, disposed inside a circle of radius $R = 40a$. Different panels refers to different percentages of randomly occupied sites: (a) 100%, (b) 98%, (c) 20%, (d) 10%. Histograms are obtained for a bin size $\delta E = 0.06\varepsilon$ in (a) and (b) and $\delta E = 0.03\varepsilon$ in (c) and (d), with $\varepsilon = \hbar^2/ma^2$. In order to facilitate the comparison, the histograms are normalized as the corresponding DOS of the infinite periodic system [dotted (red) histogram in panel (a)], i.e., to ~ 1.82. Vertical lines in (c) and (d) show the energies of few-body bound states: AB dimer [solid (black) line], AB_2 trimer with B atoms separated by a [dashed (blue) lines] and $a\sqrt{3}$ [dot-dashed (red) lines].

In the field of graphene simulation, a large interest is raised by the realization of disorder and the analysis of its effects [39, 133]. Our scheme for the realization of AAG naturally allows to introduce disorder in the form of randomly distributed empty sites, with the non-unitary filling technique already mentioned in Sec. 3.3.3. In Fig. 3.21 we present the DOS, at negative energies, for different filling factors of an OL of ~ 4000 sites, fixed $\alpha = -0.5$. The case of a fully occupied honeycomb lattice, shown in Fig. 3.21 (a), has been already discussed above. Fig. 3.21 (b) shows the combined effect of a lattice of finite size and of 2% unoccupied sites. The behavior is qualitatively the same as in panel Fig. 3.21 (a), while the central minimum is higher but still clearly visible. It starts disappearing when the fraction of empty sites is further increased. When the filling factor drastically decreases to 20%-10% [Fig. 3.21 (c) and (d)], the systems becomes more and more disordered [124], and few-body effects start playing a crucial role, giving rise to strong peaks in the DOS around the energies of AB dimers and AB_2 trimers. This behavior is analogous to those observed in the case of a square lattice, discussed in Sec. 3.3.3. The close analogy with the case of the low-filling AASL is not surprising: when only few lattice sites are occupied the AAC appears as a sparse distribution of scatterers, independently of the geometry of the generating OL. In conclusion, it is worth stressing that, with respect to one-species realizations of artificial graphene with cold atoms, our model allows to introduce randomness and defects without altering the optical potential. The possibility of having an imperfect filling due to a fraction of empty sites makes our model considerably richer toward the realization of quantum simulators of disordered graphene with cold atoms.

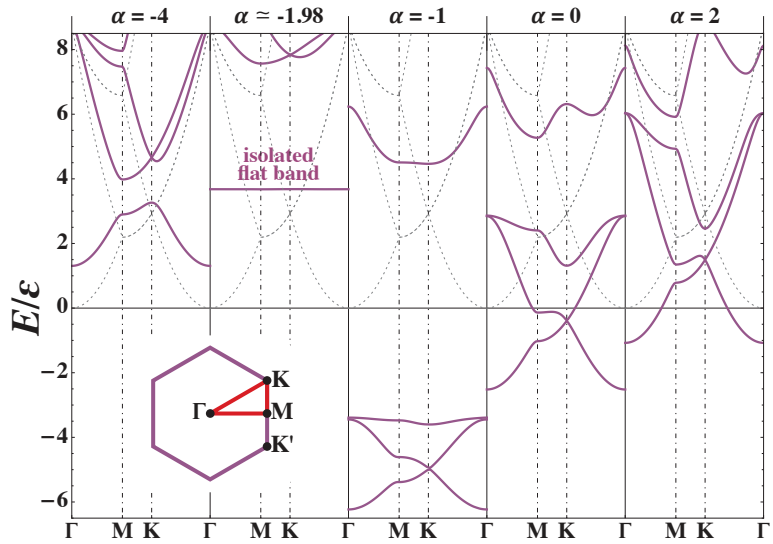

Figure 3.22 : Kagomé lattice: comparison of the band structures of the artificial lattice for different values of α evaluated along the **Γ**–**M**–**K**–**Γ** symmetry path within the FBZ (see inset). The two lowest bands touch in $\mathbf{q} = \mathbf{K}, \mathbf{K}'$, forming a Dirac cone. For $\alpha \simeq -1.98$ the fourth, isolated band is topologically flat. For $\alpha < -1$ the three lowest bands lie entirely at $E < 6.5\varepsilon$ ($\varepsilon = \hbar^2/ma^2$) and are not shown in the plot. Dashed (gray) lines correspond to the energy spectrum of a free matter wave.

3.6 Kagomé lattice

We conclude our overview of AAC giving an example of an $M = 3$ non-Bravais crystal: the kagomé lattice. This choice is motivated by the increasing interest in this peculiar structure in which several phenomena of geometric frustration have been predicted [139, 140]. As for graphene, the kagomé lattice is based on the triangular lattice, but now with *three* atoms per unit cell forming an equilateral triangle, as depicted in Fig. 3.5 (d).

When studying a periodic system, the condition $\det(\mathbb{T}) = 0$ [Eq. (3.2.30)] now translates into looking for solutions of $t_i^o(\mathbf{q}, E) = -\alpha$, with $i = 1, 2, 3$ and t_i^o being the three eigenvalues of the matrix $\mathbb{T}^o$, defined in Eq. (3.5.1). Typical spectra for different values of α are presented in Fig. 3.22. The two lowest bands again present two Dirac cones for $\mathbf{q} = \mathbf{K}, \mathbf{K}'$, but, differently from the case of graphene, in the artificial kagomé lattice the third band moves together with the lowest two. The fourth band is flat and isolated for $\alpha \simeq -2$. We note, again, that for $|\alpha| \gg 1$ the band structure approaches that of the free MW, as expected the $A-B$ interaction being weak in this limit.

The persistence of the spectral features in systems of experimental size have also been investigated. The density of solutions of Eqs. (3.2.13) and (3.2.14) for a system with ∼2000 B scatterers is shown in Fig. 3.23. The agreement with the predictions for an infinite system is extremely good, demonstrating, once again, the robustness of our results against finite-size effects.

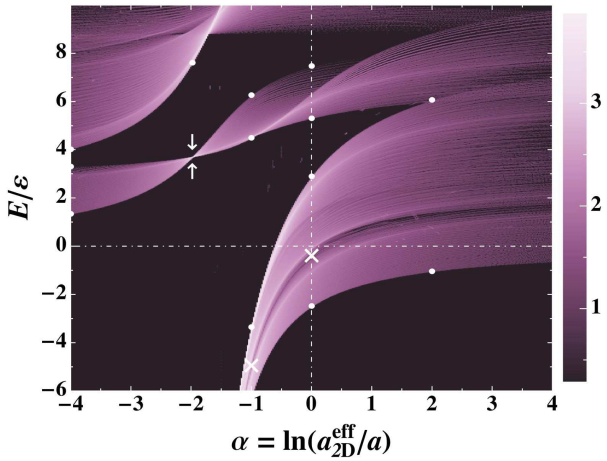

Figure 3.23 : Finite-sized kagomé lattice: DOS per scatterer in the plane $[\alpha, E/\varepsilon]$ for a system of $N = 2083$ scatterers arranged in a kagomé lattice inside a disk of radius $R = 24a$. Results were obtained with the same method as described for Fig. 3.9, discretizing the energies with a step of 0.005ε ($\varepsilon = \hbar^2/ma^2$). Quasi-Bloch bulk states were selected choosing $\Gamma_{\max} \simeq 0.5\varepsilon/\hbar$ (i.e., $\Gamma_{\max} \simeq 1460$Hz for a matter wave of ^{87}Rb atoms for $a = 500$nm). The color-map is applied to the quantity $\log_{10}(\frac{N_p}{N}\frac{\varepsilon}{\delta\alpha\,\delta E})$, where N_p is the number of selected poles of G within a rectangular bin of area $\delta\alpha\,\delta E$ ($\delta\alpha = 0.02$ and $\delta E = 0.025\varepsilon$). White crosses, circles, and arrows indicate, respectively, the positions of Dirac cones, gap boundaries, and the isolated flat band as expected from the analysis of the periodic system (Fig. 3.22).

3.7 Conclusions

We devoted this chapter to the introduction of a new model for the realization of 2D arbitrary atomic artificial crystals (AAC). The system, that is realizable with present experimental techniques, is based on the use of two independently trapped atomic species, one of which forms a 2D structure of point-like scatterers permeated by a matter wave of atoms of the second species (cf. Fig. 3.1). This system revealed itself to be promising as a quantum simulator of bi-dimensional condensed-matter systems. The fundamental difference with respect to preexinting one-species models is that the periodic (or quasi-periodic) potential felt by the matter wave is generated by atoms, and not by an underlying optical potential.

We have discussed how the interplay between scattering length and trappings allows for a wide tuning of the inter-species interaction: a key parameter through which the system features can be manipulated. A general theory for finite [Eq. (3.2.10)] and infinite periodic [Eqs. (3.2.21) and (3.2.30)] systems has been presented, specifying some illustrative examples for both Bravais and non-Bravais lattices. We proved the emergence of single (Figs. 3.7 and 3.13) and multiple (Fig. 3.17) gaps, together with the eventual presence of isolated nondispersive flat bands

(Figs. 3.18 and 3.22). Furthermore, we have pointed out the appearance of Dirac points in atomic artificial graphene and kagomé lattices, investigating the effects of a lattice distortion on their position and existence (Fig. 3.19). The robustness of our results for experimentally realizable systems has been tested against both finite size (Figs. 3.9, 3.15, 3.20, and 3.23) and disorder (Figs. 3.12 and 3.21).

The adaptability of our model makes it suitable for a number of future developments, such as the extension of the theoretical formalism to 1D and 3D artificial crystals. New perspectives can be opened considering also p-wave $A-B$ interaction or $A-A$ interactions. The latter, together with the occurrence of flat bands, would make AACs convenient simulators of 2D strongly correlated systems, in which nontrivial effects due to geometrical frustration may arise. Furthermore, it would be interesting to investigate the dynamics of the B atoms when their tunneling is no more prevented. In this case, the presence of the free species is expected to mediate an effective interaction between the lattice-sensitive atoms [141, 142].

Conclusions

In this Thesis we theoretically investigated two systems in which matter waves of cold atoms propagates in reduced dimensions.

In Chap. 1 we proposed a short and non-comprehensive review on the physics of cold atoms in optical lattices. We began by analyzing the elementary two-body scattering between ultracold particles, examining some mechanisms which allow to tune the interparticle contact interaction via external magnetic fields (Feshbach resonances in Sec. 1.2.2) or by modifying the trapping potentials (confinement and mixed-dimensional resonances in Secs. 1.4.2 and 1.4.3). We also commented, in Sec. 1.5, upon the main features of the dipole-dipole interaction, which allow for the implementation of more general Hamiltonians than those relying on the use of contact interaction only. In Sec. 1.3 we reviewed the behavior of matter waves in optical lattices. We briefly described the Bose-Hubbard and extended Bose-Hubbard model, which respectively describe contact-interacting and long-range-interacting bosons in an optical lattice. We discussed the different quantum phases emerging in these models, stressing the fundamental importance of the mapping between physical quantities and model parameters.

In Chap. 2 we investigated the behavior of a gas of dipolar bosons in a quasi-one-dimensional optical lattice. In Sec. 2.2, we studied the two-body scattering between cold dipoles tightly confined along a tube, i.e. in a quasi-1D geometry. The three-dimensional (3D) system can be mapped into an equivalent 1D one along the tube direction. In this system, the trapping in the transverse directions and the dipole-dipole interaction are taken into account by an effective quasi-1D interaction, whose scattering properties have been numerically investigated in Sec. 2.2.1. The outcomes of this analysis are supported by the results presented in Sec. 2.2.2, where we introduce and study an analytically-solvable toy-model for the quasi-1D dipole-dipole interaction. The main result is the emergence of a single dipolar-induced resonance (DIR) in the scattering amplitude for dipoles polarized perpendicularly to the tube direction [34]. In this configuration two “classical” dipoles would simply repel each other, but in the quantum case the interplay of transverse trapping and interaction anisotropy results in the existence of a dipolar bound state, whose entrance is marked by the DIR.

After studying the general features of the dipole-dipole interaction in the quasi-1D geometry, we made a step toward the optical lattice case by studying its elementary constituent: a single lattice site loaded with two dipoles. Each site is a potential well which, for a deep lattice, can be approximated by a highly elongated cigar-shaped harmonic trap. In Sec. 2.2.3, by diagonalizing the two-body Hamiltonian on a two-channel basis, we numerically solved the relative-motion Schrödinger equation for two dipoles confined in the cigar. In this approach, the two channels correspond to a bi-atomic state and a two-body dipolar bound state. We showed that the ground-state energy has a non-monotonic behavior: it grows for weak dipole moments and bends down for stronger interactions [35]. Eventually, the ground state corresponds to a dipolar dimer whose energy goes below the zero-point of the trapping potential.

When dipoles are allowed to tunnel between adjacent sites, the channels of the single-site model becomes bands of the lattice. To describe this system we introduced in Sec. 2.3 a novel atom-dimer extended Bose-Hubbard model [35]. The corresponding $T = 0$ phase diagram has been investigated by exact diagonalization of the model Hamiltonian on the configurations basis for atoms and dimers in the lattice. As a function of the dipolar strength and of the lattice depth, four phases appear: superfluid, Mott insulator (MI), mass density wave (MDW) and collapse. In particular, in contrast with preexisting models, we predict MI and MDW phases to occur in limited domains. Finally, in Sec. 2.3.3, we interpreted these results in terms of an effective single-band model, describing usefulness and limitations of this approach.

In Chap. 3 we proposed a new scheme for the realization of bidimensional atomic artificial crystals (AACs) of arbitrary geometry [42]. The model is based on the use of two independently trapped atomic species: the first one, subject to a strong in-plane confinement, constitutes a 2D matter wave which interacts *only* with atoms of the second species, deeply trapped around the nodes of a 2D optical lattice. This configuration can be obtained with present experimental techniques employing species selective optical lattices and, with respect to preexisting one-species models, it is easy allows to introduce disorder. The latter, in the form of randomly distributed empty sites, naturally appears if the lattice is loaded with filling factor lower than one.

In Sec. 3.2 we presented the theoretical tools for a completely general model. We briefly discussed the scattering between a matter wave atom and a trapped one in Sec. 3.2.1. This amounts to a 0D-2D mixed-dimensional process, whose effective scattering amplitude can be tuned via the free-free scattering length or modifying the trapping potentials [45]. Then, we derive the criterion for the existence of eigenstates of the matter-wave Hamiltonian in the presence of an arbitrary distribution of a finite number of scatterers (Sec. 3.2.2) as well as for infinite periodic systems (Sec. 3.2.3).

Finally, we applied this formalism to the exemplary cases of the atomic artificial square lattice (Sec. 3.3), triangular lattice (Sec. 3.4), graphene (Sec. 3.5) and kagomé lattice (Sec. 3.6). For all these cases, we presented the band structure of the ideal system, pointing out the appearance of single and multiple gaps, whose amplitude can be tuned acting on the interspecies interaction strength. Similarly, in the non-Bravais crystals (i.e., graphene and kagomé lattice) Dirac cones appear. Their position is shown to depend on the lattice distortion, which can induce them to merge and disappear [41]. In the same crystals there emerge isolated and non-dispersive flat bands, on which every state of the matter wave would be stationary and localized. All these features, obtained for ideal systems, have been tested against finite-size and disorder effects, pointing out the robustness and experimental observability of our predictions.

To conclude, we want to highlight some possible outlooks for the results presented in this Thesis. The increasing attention towards dipolar gases makes the analysis of the dipole-dipole scattering at the two-body level of crucial importance. For this reason, it would be interesting, first of all, to extend the analysis of Chap. 2 to simulate real experimental situations. This can be done by considering the joint effect of dipolar and contact interaction on the DIR and, consequently, on the many-body physics in the lattice. Also the case of attractive bosonic dipoles would for sure deserve some special attention. Moreover, there is a whole range of problems where the DIR is expected to arise and show important effects, but has not been accounted for up to now, among which dipolar gases confined in 2D geometries, disordered systems, and dipolar Fermi mixtures in reduced dimensions. Concerning the AACs introduced in Chap. 3, the general character of the model makes it suitable for several developments, starting from the extension of the theoretical formalism to 1D and 3D crystals. One may investigate the effect of a p-wave interspecies interaction or include intraspecies interactions in the matter wave. The latter would qualify AACs as convenient simulators for strongly correlated systems. In particular, in combination with the occurrence of flat bands, one may expect nontrivial effects of geometrical frustration. Finally, one may imagine to relax the deep-trapping approximation for the scatterers. In this scenario, the free atoms can mediate an effective interaction and affect the phase diagram of the lattice-sensitive species as a function of their density.

APPENDIX A

Quasi-1D Effective DDI

In this appendix we sketch one possible way of obtaining the quasi-1D dipole-dipole interaction (DDI) $V_{\rm dd}^{\rm 1D}$, complete of its contact term and the angle-dependent prefactor, as reported in Eq. (2.2.3) and widely used in Chap. 2.

A.1 Fourier transform of the DDI

As a preliminary calculation, we sketch the derivation of the Fourier transform (FT) of the dipole-dipole potential for polarized particles, following [143]. For two dipoles of mass m and relative position $\mathbf{r}$, the 3D dipolar potential takes the form [Eq. (1.5.2)]

$$V_{\rm dd}(\mathbf{r}) = \frac{\hbar^2 r^*}{m} \frac{1 - 3\cos^2\theta}{r^3}, \tag{A.1.1}$$

where r^* is the dipolar length [Eq. (1.5.3)] and θ the angle between $\mathbf{r}$ and the polarization direction $\hat{\mathbf{e}}$, as sketched in Fig. 1.15. The FT $\widetilde{V}_{\rm dd}(\mathbf{k})$ is defined by the relations

$$\widetilde{V}_{\rm dd}(\mathbf{k}) = \int d^3\mathbf{r}\, V_{\rm dd}(\mathbf{r})\, e^{-i\mathbf{k}\cdot\mathbf{r}}, \tag{A.1.2}$$

$$V_{\rm dd}(\mathbf{r}) = \int \frac{d^3\mathbf{r}}{(2\pi)^3}\, \widetilde{V}_{\rm dd}(\mathbf{k})\, e^{i\mathbf{k}\cdot\mathbf{r}}. \tag{A.1.3}$$

We perform the integration using spherical coordinates, in which the direction of $\mathbf{k}$ fixes the polar axis. Hence, we orient the frame so that $\hat{\mathbf{e}}$ lies on the xz plane, forming an angle α with $\mathbf{k}$ (i.e., with the polar axis). A sketch of this frame of reference is given in Fig. A.1. We stress that the

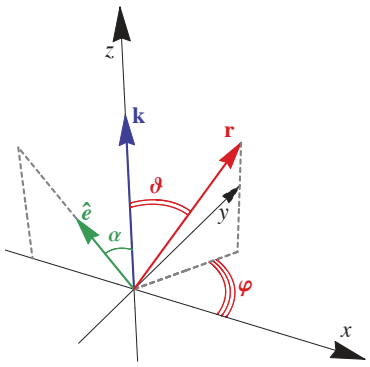

Figure A.1 : Sketch of the useful reference frame for the evaluation of the dipole-dipole interaction Fourier transform $\widetilde{V}_{\rm dd}(\mathbf{k})$. The polarization vector $\hat{\mathbf{e}}$ lies on the xz plane and the z axis is aligned with the vector $\mathbf{k}$.

angle ϑ of this frame of reference is not the angle θ appearing in Eq. (A.1.1). Indeed, in this frame we have

$$\mathbf{r} = \{r\,\sin\vartheta\,\cos\varphi;\; r\,\sin\vartheta\,\sin\varphi;\; r\,\cos\varphi\} \quad \text{and} \quad \hat{\mathbf{e}} = \{\sin\alpha;\; 0;\; \cos\alpha\}, \tag{A.1.4}$$

from which it follows

$$\cos\theta = \frac{\mathbf{r}\cdot\hat{\mathbf{e}}}{r} = \sin\alpha\,\sin\vartheta\,\cos\varphi + \cos\alpha\,\cos\vartheta. \tag{A.1.5}$$

The calculation of the integral (A.1.2) follows straightforwardly:

$$\begin{aligned}
\widetilde{V}_{\rm dd}(\mathbf{k}) &= \frac{\hbar^2 r^*}{m}\int_0^\infty dr\int_0^\pi d\vartheta\int_0^{2\pi} d\varphi\,\frac{\sin\vartheta}{r}\,e^{-ikr\cos\vartheta}\left[1-3\,(\sin\alpha\,\sin\vartheta\,\cos\varphi+\cos\alpha\,\cos\vartheta)^2\right]\\
&= \pi\frac{\hbar^2 r^*}{m}\left(3\cos^2\alpha-1\right)\int_0^\infty dr\int_0^\pi d\vartheta\int_0^{2\pi} d\varphi\,\frac{\sin\vartheta}{r}\,e^{-ikr\cos\vartheta}\left(1-3\cos^2\vartheta\right)\\
&= \cdots = \frac{4\pi}{3}\frac{\hbar^2 r^*}{m}\left(3\cos^2\alpha-1\right).
\end{aligned} \tag{A.1.6}$$

A.2 Effective 1D DDI

Now, we can derive the effective DDI for two particles trapped along a quasi-1D tube, as represented in Fig. 2.2. It is convenient to change frame of reference with respect to the one adopted in the previous section. As depicted in Fig. A.2, the tube axis coincides with the x axis, and on the transverse direction we adopt the polar coordinates $\{\rho,\phi\}$. In particular we arrange the frame so that the polarization vector $\hat{\mathbf{e}}$ lies on the xz plane. The transverse potential is assumed to be harmonic, with frequency $\omega_\perp$ and associated length $l_\perp = (\hbar/m\omega_\perp)^{1/2}$, the corresponding transverse ground state is

$$\psi_\perp(\rho) = \frac{1}{\sqrt{\pi}l_\perp}\,e^{-\rho^2/2l_\perp^2}. \tag{A.2.1}$$

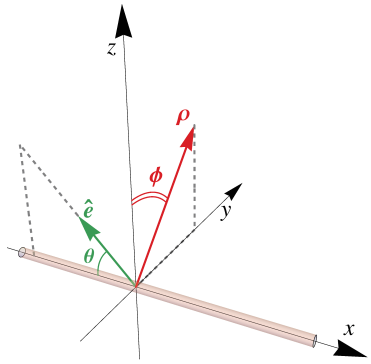

Figure A.2 : Sketch of the useful reference frame for the evaluation of the quasi-1D dipole-dipole interaction $V_{\rm dd}^{\rm 1D}(x)$. The polarization vector $\hat{\mathbf{e}}$ lies on the xz plane and the x axis is aligned with the quasi-1D tube.

The effective quasi-1D DDI is obtained integrating out the transverse degrees of freedom of the two dipoles:

$$V_{\rm dd}^{\rm 1D}(x_1 - x_2) = \int\!\!\int d^2\boldsymbol{\rho}_1\, d^2\boldsymbol{\rho}_2\, \psi_\perp^2(\rho_1)\, \psi_\perp^2(\rho_2)\, V_{\rm dd}(\mathbf{r}_1 - \mathbf{r}_2). \tag{A.2.2}$$

By introducing the center-of-mass and relative-motion coordinates

$$\mathbf{r} = \boldsymbol{\rho} + \hat{\mathbf{i}}\, x = \mathbf{r}_1 - \mathbf{r}_2, \tag{A.2.3}$$

$$\mathbf{R} = \mathbf{P} + \hat{\mathbf{i}}\, X = (\mathbf{r}_1 + \mathbf{r}_2)/2, \tag{A.2.4}$$

where $\hat{\mathbf{i}}$ is the x axis orientation vector, Eq. (A.2.2) becomes

$$\begin{aligned} V_{\rm dd}^{\rm 1D}(x) &= \frac{1}{\pi^2 l_\perp^4} \int d^2\mathbf{P}\, e^{-2\mathrm{P}^2/l_\perp^2} \int d^2\boldsymbol{\rho}\, e^{-\rho^2/2l_\perp^2}\, V_{\rm dd}(\boldsymbol{\rho} + \hat{\mathbf{i}}\, x) \\ &= \frac{1}{(2\pi)^4}\, \frac{1}{l_\perp^2} \int d^2\boldsymbol{\rho}\, e^{-\rho^2/2l_\perp^2} \int d^3\mathbf{k}\, \widetilde{V}_{\rm dd}(\mathbf{k})\, e^{ik_x x}\, e^{i\mathbf{k}_\rho\cdot\boldsymbol{\rho}}. \end{aligned} \tag{A.2.5}$$

In the last step we wrote the DDI in terms of its FT, according to Eq. (A.1.3). Writing explicitly $\widetilde{V}_{\rm dd}(\mathbf{k})$ [Eq. (A.1.6)], the integration in $d^2\boldsymbol{\rho}$ can be easily performed, leading to

$$V_{\rm dd}^{\rm 1D}(x) = \frac{1}{6\pi^2}\, \frac{\hbar^2 r^*}{m} \int d^3\mathbf{k}\, (3\cos^2\alpha - 1)\, e^{ik_x x}\, e^{-k_\rho^2 l_\perp^2/2}. \tag{A.2.6}$$

To perform the integral over $\mathbf{k}$, we consider that, in our frame of reference,

$$\hat{\mathbf{e}} = \{\cos\theta;\, \sin\theta;\, 0\}, \quad \text{and} \quad \mathbf{k} = \{k_x;\, k_\rho\, \cos\phi;\, k_\rho\, \sin\phi\}. \tag{A.2.7}$$

We thus have

$$\cos\alpha = \frac{\mathbf{k}\cdot\hat{\mathbf{e}}}{k} = \frac{k_x\cos\theta + k_\rho \sin\theta\cos\phi}{(k_x^2 + k_\rho^2)^{1/2}}. \tag{A.2.8}$$

In integrating Eq. (A.2.6), one thus needs

$$\int_0^{2\pi} d\phi \left[3(k_x\cos\theta + k_\rho\sin\theta\cos\phi)^2 - (k_x^2 + k_\rho^2)\right] = \pi(1 - 3\cos^2\theta)(k_\rho^2 - 2k_x^2), \tag{A.2.9}$$

and

$$\int_0^\infty dK_\rho\, k_\rho\, \frac{k_\rho^2 - 2k_x^2}{k_\rho^2 + k_x^2}\, e^{-k_\rho^2 l_\perp^2/2} = \frac{1}{l_\perp^2} - \frac{3}{2}\, k_x^2\, \Gamma_0\left[\frac{k_x^2 l_\perp^2}{2}\right] e^{k_x^2 l_\perp^2/2}, \tag{A.2.10}$$

where we introduced the incomplete Gamma function

$$\Gamma_0[z] = \int_0^\infty d\tau\, \frac{e^{-(z+\tau)}}{z+\tau} \quad \text{for} \quad \mathrm{Re}[z] > 0. \tag{A.2.11}$$

Making use of the dimensionless quantities

$$K = k_x\, l_\perp/\sqrt{2} \quad \text{and} \quad \xi = x/l_\perp, \tag{A.2.12}$$

one finds the intermediate result

$$V_{\mathrm{dd}}^{\mathrm{1D}}(x) = \hbar\omega_\perp \frac{r^*}{l_\perp}(1 - 3\cos^2\theta)\frac{\sqrt{2}}{6\pi} \int_{-\infty}^{+\infty} dK \left(1 - 3K^2\Gamma_0[K^2]e^{K^2}\right) e^{i\sqrt{2}K\xi}. \tag{A.2.13}$$

To perform the last integral, we observe that

$$\lim_{K\to\infty} \left(1 - 3K^2\Gamma_0[K^2]e^{K^2}\right) = 2. \tag{A.2.14}$$

It appears convenient to recast the integral in Eq. (A.2.13) as

$$\int_{-\infty}^{+\infty} dK \left[3\left(1 - K^2\Gamma_0[K^2]e^{K^2}\right) - 2\right] e^{i\sqrt{2}K\xi}. \tag{A.2.15}$$

One finds easily that

$$-2\int_{-\infty}^{+\infty} dK\, e^{i\sqrt{2}K\xi} = -\pi\sqrt{2}\,\delta(\xi). \tag{A.2.16}$$

The first term needs, instead, some manipulation to be integrated:

$$\begin{aligned} 3\int_{-\infty}^{+\infty} dK \left(1 - K^2\Gamma_0[K^2]e^{K^2}\right) e^{i\sqrt{2}K\xi} &= \\ &= 3\int_{-\infty}^{+\infty} dK\, e^{i\sqrt{2}K\xi} \int_0^\infty d\tau \left(1 - \frac{K^2}{\tau + K^2}\right) e^{-\tau} \\ &= 3\pi \int_0^\infty d\tau\ \sqrt{\tau}\, e^{-\tau - \sqrt{2\tau\xi^2}} \\ &= \frac{3\pi}{2}\left[\sqrt{\pi}\,(1+\xi^2)\,\exp\left[\frac{\xi^2}{2}\right]\mathrm{erfc}\left[\frac{|\xi|}{\sqrt{2}}\right] - \sqrt{2}\,|\xi|\right]. \end{aligned} \tag{A.2.17}$$

Finally, when Eqs. (A.2.16) and (A.2.17) are used to solve the integral in Eq. (A.2.13), the quasi-1D effective DDI results

$$V_{\mathrm{dd}}^{\mathrm{1D}}(x) = \hbar\omega_\perp \frac{r^*}{l_\perp}(1 - 3\cos^2\theta)\left\{\sqrt{\frac{\pi}{8}}\left(1 + \frac{x^2}{l_\perp^2}\right)\exp\left[\frac{x^2}{2l_\perp^2}\right]\mathrm{erfc}\left[\frac{|x|}{\sqrt{2}l_\perp}\right] - \frac{|x|}{2l_\perp} - \frac{2}{3}\,\delta\left(\frac{x}{l_\perp}\right)\right\}. \tag{A.2.18}$$

APPENDIX B

Limitations of Finite-Basis Approaches

In Sec. 2.2.3 we discussed the emergence of a dipolar-induced resonance in a highly elongated harmonic trap. In this context, we diagonalized the relative-motion Hamiltonian on a finite basis, showing that, to properly describe the emergence of the resonance, one needs to include a bound state wavefunction in the basis. In this appendix we get back on the limitations of a finite-basis approach in the presence of bound states. More specifically, we consider the analytically solvable problem of two contact-interacting particles in 1D. In this case, the exact solution [106] can be directly compared with the finite-basis results.

B.1 Two contact-interacting particles in 1D

Let us consider two cold atoms in a strictly 1D space, subject to a harmonic confinement of frequency ω_0. The non-interacting Hamiltonian of such system is

$$\begin{aligned}\mathcal{H}_0 &= -\frac{\hbar^2}{2m_1}\frac{\partial^2}{\partial x_1^2} + \frac{1}{2}m_1\omega_0^2 x_1^2 - \frac{\hbar^2}{2m_2}\frac{\partial^2}{\partial x_2^2} + \frac{1}{2}m_2\omega_0^2 x_2^2 \\ &= -\frac{\hbar^2}{2M}\frac{\partial^2}{\partial X^2} + \frac{1}{2}M\omega_0^2 X^2 - \frac{\hbar^2}{2\mu}\frac{\partial^2}{\partial x^2} + \frac{1}{2}\mu\omega_0^2 x^2, \end{aligned} \tag{B.1.1}$$

where we introduced the center-of-mass and relative-motion coordinates X and x, the total mass $M = m_1 + m_2$, and the reduced mass $\mu = m_1 m_2/(m_1 + m_2)$. The center-of-mass problem is unaffected by the interatomic interaction, hence we focus on the relative-motion Hamiltonian, which, in the presence of a contact pseudopotential [Eq. (1.4.12)], reads

$$\mathcal{H}_{\text{rel}} = -\frac{\hbar^2}{2\mu}\frac{\partial^2}{\partial x^2} + \frac{1}{2}\mu\omega_0^2 x^2 - \frac{\hbar^2}{\mu}\frac{1}{a_{1\text{D}}}\delta(x). \tag{B.1.2}$$

It is convenient to rewrite the previous expression in terms of dimensionless quantities. Introducing the unit of energy $\hbar\omega_0$ and the unit of length $l_0 = (\hbar/\mu\omega_0)^{1/2}$, the adimensional Hamiltonian to solve is

$$\widetilde{\mathcal{H}}_{\rm rel} = \widetilde{\mathcal{H}}_{\rm ho} - \frac{1}{\alpha}\,\delta(\xi) = -\frac{1}{2}\,\frac{\partial^2}{\partial\xi^2} + \frac{1}{2}\,\xi^2 - \frac{1}{\alpha}\,\delta(\xi), \tag{B.1.3}$$

being $\xi = x/l_0$ and $\alpha = a_{\rm 1D}/l_0$. The eigenfunctions of the harmonic oscillator Hamiltonian $\widetilde{\mathcal{H}}_{\rm ho}$ are the well known wave functions

$$\phi_n(\xi) = \frac{1}{\pi^{1/4}}\,\frac{1}{\sqrt{2^n n!}}\,H_n(\xi)\,e^{-\xi^2/2} \qquad n = 0, 1, 2, \cdots, \tag{B.1.4}$$

with the corresponding eigenvalues $\varepsilon_n = n + 1/2$ and where H_n are Hermite polynomials.

B.1.1 Analytic solution

The eigenenergies of $\widetilde{H}_{\rm rel}$ [Eq. (B.1.3)] can be determined analytically, as described in [106] (also for 2D and 3D systems). Here, we sketch the main steps of the calculation. The relative-motion Schrödinger equation is

$$\widetilde{\mathcal{H}}_{\rm rel}\Psi(\xi) = \varepsilon\,\Psi(\xi). \tag{B.1.5}$$

It is natural to project the wave function $\Psi(\xi)$ on the complete basis $\{\phi_n(\xi)\}$ of harmonic-oscillator eigenfunctions:

$$\Psi(\xi) = \sum_{n=0}^{\infty} c_n\,\phi_n(\xi). \tag{B.1.6}$$

By inserting Eq. (B.1.6) into Eq. (B.1.5), one obtains

$$\sum_{n=0}^{\infty} c_n\,(\varepsilon_n - \varepsilon)\,\phi_n(\xi) = \frac{1}{\alpha}\sum_{n=0}^{\infty} c_n\,\delta(\xi)\,\phi_n(\xi). \tag{B.1.7}$$

Projecting the previous equation on $\phi_m(\xi)$, after some manipulation, we have

$$c_m = \frac{\phi_m(0)}{\varepsilon_m - \varepsilon}\,\frac{1}{\alpha}\sum_{n=0}^{\infty} c_n\,\phi_n(0). \tag{B.1.8}$$

Eq. (B.1.8) suggests to introduce the *Ansatz* $c_n = \mathcal{A}\phi_n(0)/(\varepsilon_m - \varepsilon)$, where $\mathcal{A}$ is a constant fixed by the normalization of $\Psi(\xi)$. This *Ansatz* allows to reduce Eq. (B.1.8) to

$$\alpha = \sum_{n=0}^{\infty} \frac{\phi_n^2(0)}{\varepsilon_n - \varepsilon}. \tag{B.1.9}$$

The infinite sum appearing in Eq. (B.1.9) can be solved analytically, leading to the implicit relation between α and ε:

$$\frac{1}{\alpha} = 2\,\frac{\Gamma\left[\frac{3}{4} - \frac{\varepsilon}{2}\right]}{\Gamma\left[\frac{1}{4} - \frac{\varepsilon}{2}\right]}. \tag{B.1.10}$$

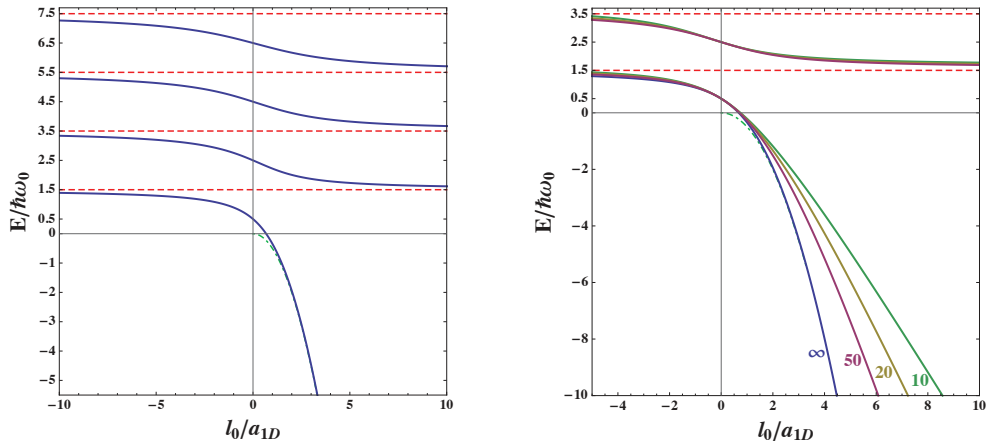

Figure B.1 : Left: Analytic results for the eigenvalues of $\mathcal{H}_{\rm rel}$ [Eq. (B.1.2)] for even [solid (blue) curves] and odd [dashed (red) lines] solutions of the Scrödinger equation (B.1.5), obtained from Eq. (B.1.10). The dot-dashed (green) curve indicates the energy of the contact-potential bound state E_δ (see text). Right: Ground-state energy of $\mathcal{H}_{\rm rel}$ [Eq. (B.1.2)] evaluated for different sizes of the diagonalization basis (solid curves). For finite-sized basis we used Eq. (B.1.13) with $N = 10$ (green), 20 (yellow), and 50 (purple). The $N = \infty$ result (blue) is the analytic solution given in Eq. (B.1.10). Dashed (red) and dot-dashed (green) lines represent the same quantities that in the left panel.

Relation (B.1.10) is shown in Fig. B.1 (left). Odd eigenstates are unaffected by the contact potential, since the corresponding wavefunctions vanish at $\xi = 0$. For even eigenstates, the non-interacting limit is reached for $a_{\rm 1D} \to \infty$, indeed, in this case, the 1D coupling constant of the contact interaction $g_{\rm 1D} = -\hbar^2/\mu a_{\rm 1D} \to 0$. In the strong-interaction regime $|a_{\rm 1D}| \to 0$, the particles become impenetrable and the eigenenergies tend to the values of odd eigenfunctions (a mechanism discussed in Sec. 2.2.2 in the context of the generalized toy model for the effective quasi-1D DDI).

An exception is represented by the system ground state. Its energy, indeed, goes below the zero-point energy of the harmonic-potential, marking the formation of a two-body bound state. For $a_{\rm 1D} \ll l_0$ (i.e., $1/\alpha \gg 1$) the lowest eigenenergy tends to $E_\delta = -\hbar^2/2\mu a_{\rm 1D}^2$, that is the energy of the contact-potential bound state

$$\phi_\delta(x) = \frac{1}{\sqrt{a_{\rm 1D}}}\, e^{-|x|/a_{\rm 1D}}, \tag{B.1.11}$$

solution of the eigenvalue equation

$$-\left[\frac{\hbar^2}{2\mu}\frac{\partial^2}{\partial x^2} + \frac{\hbar^2}{\mu}\frac{1}{a_{\rm 1D}}\,\delta(x)\right]\phi_\delta(x) = E_\delta\,\phi_\delta(x). \tag{B.1.12}$$

B.1.2 Finite-basis approach

In the fortunate case of $\mathcal{H}_{\rm rel}$ [Eq. (B.1.2)], the condition for the eigenenergies of the system (B.1.9) can be evaluated analytically. In the implicit Eq. (B.1.10) all the harmonic-oscillator eigenstates are taken into account. In other circumstances, instead, one needs a numerical approach and, consequently, a finite-sized basis (cf. the quasi-1D efective DDI treated in Sec. 2.2.3). The present case of two contact-interacting particles, for which the analytic solution is known, allows to directly confront the finite-basis result with the exact one.

Using a finite set of harmonic-oscillator eigenstates to diagonalize $\mathcal{H}_{\rm rel}$ is equivalent to truncate the sum in Eq. (B.1.9) to a finite value $n=N$:

$$\alpha = \sum_{n=0}^{N} \frac{\phi_n^2(0)}{\varepsilon_n - \varepsilon}. \tag{B.1.13}$$

The behavior of $E(a_{\rm 1D})$ for the system ground state and the first excited state is presented in Fig. B.1 (right), comparing the results obtained for different values of N. The excited state energy rapidly converges to the exact result. The ground state energy goes below $\hbar\omega_0/2$ and decreases, but, differently from the excited state, the behavior does not converge to the exact solution. In particular the energy decreases linearly in $1/\alpha$ instead of acquiring the correct quadratic character. The origin of this discrepancy is in the shape of the ground-state wave function. The latter, for $1/\alpha \gg 1$, tends to $\phi_\delta(x)$ [Eq. (B.1.12)], whose cusp in $x=0$ cannot be reproduced by any finite set of $\phi_n(x)$ [Eq. (B.1.4)], that are all smooth in zero.

APPENDIX C

The 0D-2D Scattering

In Sec. 3.2.1 we discussed the fundamental role of the 0D-2D scattering process in atomic artificial crystals. In this appendix we investigate a simple situation in which the dependence of the 2D effective scattering length a_{2D}^{eff} on the system parameters can be easily evaluated. We consider the situation depicted in Fig. C.1, in which an atom A, harmonically trapped on a plane, impinges on an atom B, kept in a 3D isotropic trap. We assume the trapping frequency ω_A of the atom A to be much smaller than ω_0, that is the trapping frequency for the B atom. The $A-B$ interaction in free space is modeled by the 3D contact pseudopotential (1.2.6), whose strength depends on the s-wave scattering length a_{3D}.

This complex 3D system, involving different trapping frequencies and a contact interaction, can be mapped into an equivalent 2D system, in which the B scatterer is fixed ($m_B^{\text{eff}} \to \infty$). The A–B interaction is now described by a 2D contact pseudopotential [cf. Eq. (1.4.7)], whose strength de-

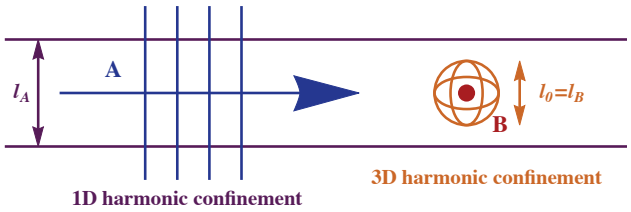

Figure C.1 : Representation of a system in which a mixed-dimension 0D-2D scattering process takes place. The atom A is harmonically confined on a plane with trapping frequency ω_A, defining $l_A = (\hbar/m_A\omega_A)^{1/2}$. The atom B is tightly trapped in an isotropic 3D trap of frequency ω_0, with $l_A \gg l_0 = (\hbar/m_B\omega_0)^{1/2}$.

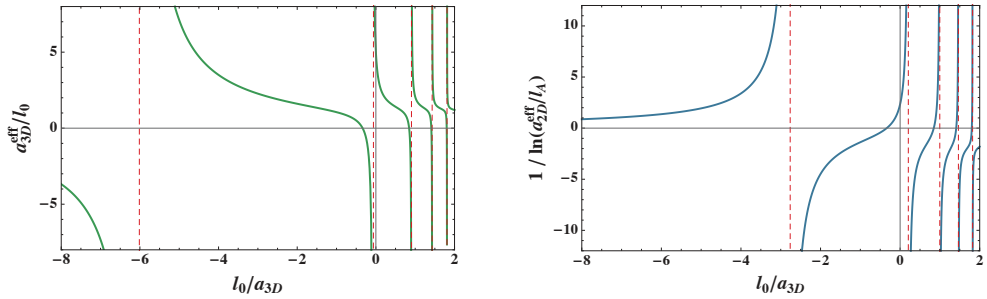

Figure C.2 : Left: Effective 3D scattering length a_{3D}^{eff} for the 0D-3D scattering process as a function of the free-free scattering length a_{3D} and the trap length scale l_0. Results have been obtained following [16] for a masses ratio $m_B/m_A = 0.15$, corresponding to a 0D-trapped ^{6}Li atom and and a 2D-trapped ^{40}K one. Right: Effective 2D interaction strength $1/\ln\left(a_{2D}^{\text{eff}}/l_A\right)$ for the 0D-2D scattering process in the system represented in Fig. C.1. We consider the same atomic species of the left panel and a frequencies ratio $\omega_0/\omega_A = 10$.

pends on an effective 2D scattering length a_{2D}^{eff} determined by the real system parameters, namely, m_A/m_B, ω_0, ω_A, and a_{3D}. In the geometry described in Fig. C.1, one can evaluate a_{2D}^{eff} by combining the results of [16] on the 0D-3D scattering (cf. Sec. 1.4.3) with those on the quasi-2D scattering process of [15, 75] (cf. Sec. 1.4.2).

The assumption $\omega_A \ll \omega_0$, allows to neglect the harmonic confinement of frequency ω_A when A is close to B. Hence, one can model the $A-B$ scattering through an effective contact interaction, ruled by the scattering length $a_{3D}^{\text{eff}}(a_{3D}, \omega_0, m_A/m_B)$ derived in [16] and represented in Fig. C.2 (left). Then, the in-plane confinement reduces this effective 3D system into a quasi-2D one, whose scattering amplitude a_{2D}^{eff}, derived in [15, 75], has been presented in Eq. (1.4.18). Finally, the combined expression is

$$\frac{1}{g_{2D}^{\text{eff}}} \propto \ln\left(\frac{a_{2D}^{\text{eff}}}{l_A}\right) = \beta - \sqrt{\frac{\pi\, m_B \omega_0}{2\, m_A \omega_A}}\, \frac{l_0}{a_{3D}^{\text{eff}}}, \tag{C.0.1}$$

with the introduction of the numerical factor $\beta \simeq 0.733$. The behavior of g_{2D}^{eff} for a given masses ratio of the two atomic species is presented in Fig. C.2 (right). Similarly to the 0D-3D case, the 0D-2D scattering presents an infinite series of mixed-dimension resonances. The effective 2D interaction is, thus, experimentally tunable adjusting the free-space scattering length a_{3D} or the trapping frequencies.

APPENDIX D

Real-to-Reciprocal Space Change

In Sec. 3.2.3 we derived a general formalism to investigate the properties of a 2D matter wave propagating through an infinite, periodic structure of scatterers. In this context we transformed the sums over real-lattice vectors [Eqs. (3.2.19), (3.2.29a), and (3.2.29b)], in sums over reciprocal-lattice vectors [Eqs. (3.2.20), (3.2.31a), and (3.2.31b)]. The latter are easier to implement numerically and rapidly converge.

In this appendix we present in detail the delicate procedure allowing for this transformation. In particular we point out the emergence of a lattice-geometry dependent coefficient, whose value is determined for some relevant case.

D.1 Bravais or diagonal terms

We start by manipulating the left-hand side of Eq. (3.2.19) or, equivalently, a diagonal element of the matrix $\mathbb{T}$ defined in Eq. (3.2.29b). In particular we focus on the sum, rewriting $g_0(\mathbf{R})$, introduced in Eq. (3.2.4), as

$$g_0(\mathbf{R}) = \int \frac{d^2\mathbf{p}}{(2\pi)^2}\, \widetilde{g}_0(\mathbf{p})\, e^{i\mathbf{p}\cdot\mathbf{R}} \tag{D.1.1}$$

in terms of its Fourier transform

$$\widetilde{g}_0(\mathbf{p}) = \frac{2m}{\hbar^2}\left(\mathcal{P}\frac{1}{k^2-p^2} - i\frac{\pi}{2k}\delta(k-p)\right), \tag{D.1.2}$$

where $\mathcal{P}$ denotes Cauchy's principal value. Once sum and integral are exchanged, we obtain

$$\sum_{\mathbf{R}\in L^*} g_0(\mathbf{R})\, e^{i\mathbf{q}\cdot\mathbf{R}} = \int \frac{d^2\mathbf{p}}{(2\pi)^2}\, \widetilde{g}_0(\mathbf{p})\left(\sum_{\mathbf{R}\in L} e^{i(\mathbf{p}+\mathbf{q})\cdot\mathbf{R}} - 1\right), \tag{D.1.3}$$

where, by adding and subtracting the $\mathbf{R}=0$ term, we now have a sum running over the entire set L of real-lattice vectors. For such a summation Poisson's identity holds, stating that

$$\sum_{\mathbf{R}\in L} F(\mathbf{R}) = \frac{1}{\mathcal{A}} \sum_{\mathbf{K}\in RL} \widetilde{F}(\mathbf{K}), \tag{D.1.4}$$

where $\mathcal{A}$ is the unit cell area in real space. In the case of interest $\widetilde{F}(\mathbf{K}) = (2\pi)^2\delta^{(2)}(\mathbf{p}+\mathbf{q}-\mathbf{K})$ is the Fourier transform of $F(\mathbf{R}) = \exp[i(\mathbf{p}+\mathbf{q})\cdot\mathbf{R}]$. By integrating out terms involving δ-functions, we obtain

$$\sum_{\mathbf{R}\in L^*} \frac{\pi\hbar^2}{m}\, g_0(\mathbf{R})\, e^{i\mathbf{q}\cdot\mathbf{R}} = \frac{2\pi}{\mathcal{A}} \sum_{\mathbf{K}\in RL} \frac{1}{k^2-|\mathbf{K}-\mathbf{q}|^2} + i\frac{\pi}{2} - \mathcal{P}\int \frac{d^2\mathbf{p}}{2\pi}\, \frac{1}{k^2-p^2}. \tag{D.1.5}$$

It remains to evaluate the principal-valued integral. For an arbitrary choice of ρ such that $0<\rho<k$, we have

$$\mathcal{P}\int \frac{d^2\mathbf{p}}{2\pi}\, \frac{1}{k^2-p^2} = \mathcal{P}\int_{p>\rho} \frac{d^2\mathbf{p}}{2\pi}\, \frac{1}{k^2-p^2} - \frac{1}{2}\ln\!\left(1-\frac{\rho^2}{k^2}\right), \tag{D.1.6}$$

and the Bravais-element $\mathbb{T}_{nn}$ becomes

$$\begin{aligned}\mathbb{T}_{nn} = {} & \ln\!\left(\frac{e^\gamma}{2}\, k a_{\mathrm{2D}}^{\mathrm{eff}}\right) + \frac{1}{2}\ln\!\left(1-\frac{\rho^2}{k^2}\right) + \frac{2\pi}{\mathcal{A}}\, \frac{1}{k^2-q^2} \\ & + \frac{2\pi}{\mathcal{A}} \sum_{\mathbf{K}\in RL^*} \frac{1}{k^2-|\mathbf{K}-\mathbf{q}|^2} - \mathcal{P}\int_{p>\rho} \frac{d^2\mathbf{p}}{2\pi}\, \frac{1}{k^2-p^2}.\end{aligned} \tag{D.1.7}$$

We now need to introduce two auxiliary quantities,

$$\mathcal{S}_{\rho,\mathrm{uv}} = \frac{2\pi}{\mathcal{A}} \sum_{\mathbf{K}\in RL^*\setminus \mathrm{uv}} \frac{1}{k^2-|\mathbf{K}-\mathbf{q}|^2} - \mathcal{P}\int_{p>\rho\setminus\mathrm{uv}} \frac{d^2\mathbf{p}}{2\pi}\, \frac{1}{k^2-p^2} \tag{D.1.8}$$

and

$$S_{\rho,\mathrm{uv}} = \frac{2\pi}{\mathcal{A}} \sum_{\mathbf{K}\in RL^*\setminus \mathrm{uv}} \frac{1}{K^2} - \int_{p>\rho\setminus\mathrm{uv}} \frac{d^2\mathbf{p}}{2\pi}\, \frac{1}{p^2}, \tag{D.1.9}$$

where an arbitrary ultraviolet cutoff (uv) is added in the domains of sum and integration. Note that the second line of Eq. (D.1.7) is exactly $\mathcal{S}_{\rho,\infty}$, which is $\mathcal{S}_{\rho,\mathrm{uv}}$ in the limit of a cutoff boundary pushed to infinity. From definitions (D.1.8) and (D.1.9) it follows that

$$\mathcal{S}_{\rho,\mathrm{uv}} + S_{\rho,\mathrm{uv}} \xrightarrow[\mathrm{uv}\to\infty]{} -\frac{1}{2}\ln\!\left(\frac{k^2}{\rho^2}-1\right) + \frac{2\pi}{\mathcal{A}} \sum_{\mathbf{K}\in RL^*} \left(\frac{1}{k^2-|\mathbf{K}-\mathbf{q}|^2} + \frac{1}{K^2}\right). \tag{D.1.10}$$

We thus add and subtract $S_{\rho,\infty}$ to Eq. (D.1.7), and after some algebraic manipulation we obtain

$$\mathbb{T}_{nn} = \ln(\rho a) - S_{\rho,\infty} + \ln\!\left(\frac{e^\gamma}{2}\right) + \frac{2\pi}{\mathcal{A}}\, \frac{1}{k^2-q^2} \frac{2\pi}{\mathcal{A}} \sum_{\mathbf{K}\in RL^*} \left(\frac{1}{k^2-|\mathbf{K}-\mathbf{q}|^2} + \frac{1}{K^2}\right) + \alpha, \tag{D.1.11}$$

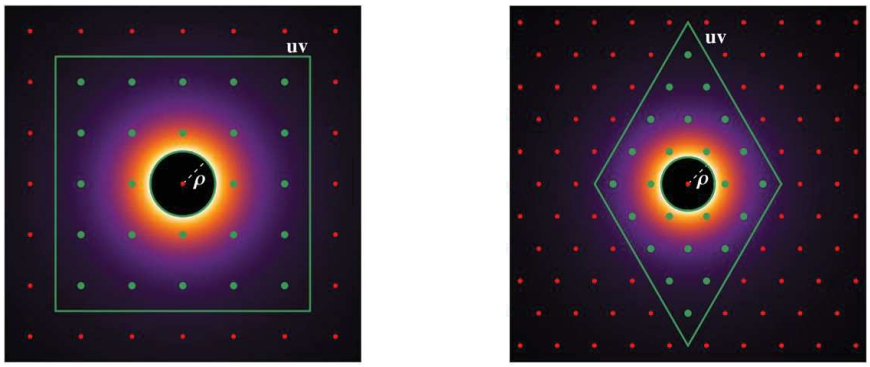

Figure D.1 : Density plots of $1/p^2$. Left: For the square lattice of Fig. 3.3. The (green) boundaries $p^2 = \rho^2$ and $|p_x|, |p_y| = 2\pi(N + 1/2)/a$ delimit the integration domain of Eq. (D.1.14) (here, $\rho = 3/a$ and $N = 2$). The points belong to the reciprocal lattice set *RL*. The larger (green) ones are those accounted by the sum in Eq. (D.1.15). Right: Same as left, but for the triangular lattice of Fig. 3.4. The (green) boundaries $p^2 = \rho^2$ and $\sqrt{3}|p_y| = 4\pi(N + 1/2) - 3|p_x|$ delimit the integration domain of Eq. (D.1.16) (here, $\rho = 3/a$ and $N = 2$). The larger (green) points are those on which runs the sum in Eq. (D.1.18).

where we introduced the parameter $\alpha = \ln(a_{2D}^{\text{eff}}/a)$ and the arbitrary unit of length a. From Eq. (D.1.11), it finally follows the definition of

$$C_\infty = \lim_{\text{uv}\to\infty} C_{\rho,\text{uv}}, \tag{D.1.12}$$

with

$$C_{\rho,\text{uv}} = \ln(\rho a) - S_{\rho,\text{uv}} = \ln(\rho a) + \int_{p>\rho\setminus\text{uv}} \frac{d^2\mathbf{p}}{2\pi}\frac{1}{p^2} - \frac{2\pi}{\mathcal{A}}\sum_{\mathbf{K}\in RL^*\setminus\text{uv}}\frac{1}{K^2}. \tag{D.1.13}$$

D.1.1 Evaluation of the geometrical coefficient

When the cutoff boundary tends to infinity, the coefficient $C_{\rho,\text{uv}}$ defined in Eq. (D.1.13) numerically converges to a ρ-independent quantity determined only by the geometrical properties of the considered Bravais lattice. Here, we present this convergent behavior for the exemplary cases of a square and a triangular lattice.

In the case of a square lattice (cf. Fig. 3.3), it is convenient to define the ultraviolet cutoff by excluding values of $\mathbf{p}$ for which $|p_x|, |p_y| > 2\pi(N + 1/2)/a$, where N is an arbitrary integer larger than one. This means that the integral in Eq. (D.1.13) has to be performed over a pierced square of side $4\pi(N + 1/2)/a$ and hole radius ρ, as represented in Fig. D.1 (left). Similarly, the sum will count only the points of the set *RL* falling in the same area. In this case the integral has an analytic solution:

$$\int_{p>\rho\setminus\text{uv}} \frac{d^2\mathbf{p}}{2\pi}\frac{1}{p^2} = \ln\left[\frac{4\pi}{\rho a}(N + 1/2)\right] - \frac{2C}{\pi}, \tag{D.1.14}$$

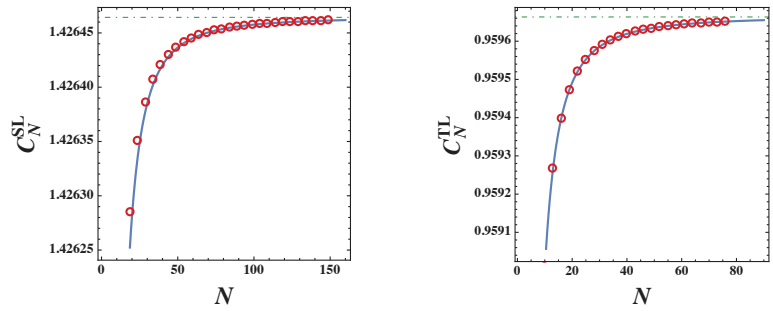

Figure D.2 : Left: For the square lattice. Numerical values of C_N^{SL} [Eq. (D.1.15)] as a function of N. The solid (blue) line fits the large-N behavior and converges to $C_\infty^{\mathrm{SL}} \simeq 1.4265$. Right: Same as left, but for the triangular lattice coefficient C_N^{TL} [Eq. (D.1.18)]. The large-N behavior converges here to $C_\infty^{\mathrm{TL}} \simeq 0.9597$.

where $C \simeq 0.915966$ is the Catalan's constant. By using the previous result in Eq. (D.1.13) and after some algebraic manipulations, one finds

$$C_N^{\mathrm{SL}} = \ln(4\pi) - \frac{2C}{\pi} + \ln(N+1/2) - \frac{2}{\pi}\sum_{n=1}^{N}\sum_{m=0}^{N}\frac{1}{n^2+m^2}, \tag{D.1.15}$$

which shows explicitly that the geometrical coefficient does not depend on the arbitrary parameters a and ρ.

The convergence of C_N^{SL} to C_∞^{SL} for $N \to \infty$ is shown in Fig. D.2 (left). The limit is extrapolated by fitting numerical data (circles in figure) from the interval $[N_{max} - 30, N_{max}]$ with the expression $A + B/N^\lambda$, then increasing N_{max} until A varies less than the required accuracy. With this method we obtained $C_\infty^{\mathrm{SL}} \simeq 1.42646444$ with the precision of 10^{-8} ($N_{max} = 118$, $B \simeq -0.063$, $\lambda = \simeq 1.985$).

In the case of the triangular lattice (cf. Fig. 3.4), we perform the same analysis. The convenient uv cutoff is now defined by $\sqrt{3}|p_y| < 4\pi(N+1/2) - 3|p_x|$. The integral in Eq. (D.1.13) has now to be performed over the pierced rhombus depicted in Fig. D.1 (right). Once again an analytic result exists:

$$\int_{p>\rho\setminus \mathrm{uv}} \frac{d^2\mathbf{p}}{2\pi}\,\frac{1}{p^2} = \ln\left[\frac{1}{\rho a}(N+1/2)\right] - \mathcal{B}. \tag{D.1.16}$$

The numeric constant $\mathcal{B}$ is defined by

$$\mathcal{B} = \ln\left(\frac{4\pi}{\sqrt{3}}\right) - \frac{1}{\pi}\,\mathrm{Im}\left[\mathrm{Li}_2\left(e^{2i\pi/3}\right) - \mathrm{Li}_2\left(e^{5i\pi/3}\right)\right] \simeq 1.443275, \tag{D.1.17}$$

where $\mathrm{Li}_2(z)$ is the polylogarithm function. Consequently, the simplified expression for the triangular-lattice coefficient C_N^{TL} is

$$C_N^{\mathrm{TL}} = \mathcal{B} + \ln(N+1/2) - \frac{\sqrt{3}}{2\pi}\sum_{n=1}^{N}\sum_{m=-N}^{N}\frac{1+\delta_{m0}}{n^2+m^2-nm}, \tag{D.1.18}$$

where δ_{m0} is a Kronecker delta. Fig. D.2 (right) shows the convergent behavior of C_N^{TL} as a function of N. The geometrical coefficient C_∞^{TL} can be extrapolated with the same method described for the square lattice. In this case we obtained $C_\infty^{\mathrm{SL}} \simeq 0.95966334$ with the precision of 10^{-8} ($N_{max} = 104$, $B \simeq -0.066$, $\lambda = \simeq 1.983$).

D.2 Off-diagonal terms

In conclusion, let us consider the transformation of the off-diagonal element of $\mathbb{T}$, introduced in Eq.(3.2.29a). The space change follows straightforwardly by applying the same techniques used for the diagonal element in Sec. D.1. We write again $g_0(\mathbf{R})$ in terms of its Fourier transform $\widetilde{g}_0(\mathbf{p})$, obtaining

$$\begin{aligned}\sum_{\mathbf{R}\in L} g_0(\mathbf{R}+\mathbf{t}_{nm})\, e^{i\mathbf{q}\cdot\mathbf{R}} &= \int \frac{d^2\mathbf{p}}{(2\pi)^2}\, \widetilde{g}_0(\mathbf{p})\, e^{i\mathbf{p}\cdot\mathbf{t}_{nm}} \sum_{\mathbf{R}\in L} e^{i(\mathbf{p}+\mathbf{q})\cdot\mathbf{R}} \\ &= \frac{1}{\mathcal{A}} \sum_{\mathbf{K}\in RL} \widetilde{g}_0(\mathbf{K}-\mathbf{q})\, e^{i(\mathbf{K}-\mathbf{q})\cdot\mathbf{t}_{nm}}, \end{aligned} \tag{D.2.1}$$

where, in the last step, we made use of Poisson's identity as introduced in Eq. (D.1.4). Finally Eq. (3.2.31a) directly follows from Eq. (D.2.1) by writing explicitly $\widetilde{g}_0(\mathbf{K}-\mathbf{q})$.

Bibliography

[1] C. Kittel, *Introduction to Solid State Physics*, 8th ed. (Wiley, 2004).

[2] N. W. Ashcroft and N. D. Mermin, *Solid State Physics* (Cengage Learning, 1976).

[3] R. P. Feynman, *Simulating Physics with Computers*, Int. J. Theor. Phys. **21**, 467 (1982).

[4] V. Bose, *Plancks Gesetz und Lichtquantenhypothese*, Z. Phys. **26**, 178 (1924).

[5] A. Einstein, Sitzber. Kgl. Preuss. Akad. Wiss. , 261 (1924).

[6] A. Einstein, Sitzber. Kgl. Preuss. Akad. Wiss. , 3 (1925).

[7] L. P. Pitaevskii and S. Stringari, *Bose-Einstein Condensation*, International Series of Monographs on Physics (Oxford University Press, 2003).

[8] S. Giorgini, L. P. Pitaevskii, and S. Stringari, *Theory of ultracold atomic Fermi gases*, Rev. Mod. Phys. **80**, 1215 (2008).

[9] M. H. Anderson, J. R. Ensher, M. R. Matthews, C. E. Wieman, and E. A. Cornell, *Observation of Bose-Einstein Condensation in a Dilute Atomic Vapor*, Science **269**, 198 (1995).

[10] C. C. Bradley, C. A. Sackett, J. J. Tollett, and R. G. Hulet, *Evidence of Bose-Einstein Condensation in an Atomic Gas with Attractive Interactions*, Phys. Rev. Lett. **75**, 1687 (1995), **79**, 1170(E) (1997).

[11] K. B. Davis, M. O. Mewes, M. R. Andrews, N. J. van Druten, D. S. Durfee, D. M. Kurn, and W. Ketterle, *Bose-Einstein Condensation in a Gas of Sodium Atoms*, Phys. Rev. Lett. **75**, 3969 (1995).

[12] B. DeMarco and D. S. Jin, *Onset of Fermi Degeneracy in a Trapped Atomic Gas*, Science **285**, 1703 (1999).

[13] C. Chin, R. Grimm, P. Julienne, and E. Tiesinga, *Feshbach resonances in ultracold gases*, Rev. Mod. Phys. **82**, 1225 (2010).

[14] M. Olshanii, *Atomic Scattering and in the Presence of an External Confinement and a Gas of Impenetrable Bosons*, Phys. Rev. Lett. **81**, 938 (1998).

[15] D. S. Petrov, M. Holzmann, and G. V. Shlyapnikov, *Bose-Einstein Condensation in Quasi-2D Trapped Gases*, Phys. Rev. Lett. **84**, 2551 (2000).

[16] P. Massignan and Y. Castin, *Three-dimensional strong localization of matter waves by scattering from atoms in a lattice with a confinement-induced resonance*, Phys. Rev. A **74**, 013616 (2006).

[17] R. Grimm, M. Weidermüller, and Y. B. Ovchinnikov, *Optical dipole traps for neutral atoms*, Adv. At. Mol. Opt. Phys. **42**, 95 (2000).

[18] I. Bloch, *Ultracold quantum gases in optical lattices*, Nat. Phys. **1**, 23 (2005).

[19] I. Bloch, J. Dalibard, and W. Zwerger, *Many-body physics with ultracold gases*, Rev. Mod. Phys. **80**, 885 (2008).

[20] I. Bloch, J. Dalibard, and S. Nascimbène, *Quantum simulations with ultracold quantum gases*, Nature Phys. **8**, 267 (2012).

[21] M. P. A. Fisher, P. B. Weichman, G. Grinstein, and D. S. Fisher, *Boson localization and the superfluid-insulator transition*, Phys. Rev. B **40**, 546 (1989).

[22] R. Pai and R. Pandit, *Superfluid, Mott-insulator, and mass-density-wave phases in the one-dimensional extended Bose-Hubbard model*, Phys. Rev. B **71**, 104508 (2005).

[23] K. Góral, L. Santos, and M. Lewenstein, *Quantum Phases of Dipolar Bosons in Optical Lattices*, Phys. Rev. Lett. **88**, 170406 (2002).

[24] M. Greiner, O. Mandel, T. Esslinger, T. W. Hänsch, and I. Bloch, *Quantum phase transition from a superfluid to a Mott insulator in a gas of ultracold atoms*, Nature **415**, 39 (2002).

[25] T. Lahaye, C. Menotti, L. Santos, M. Lewenstein, and T. Pfau, *The physics of dipolar bosonic quantum gases*, Rep. Prog. Phys. **72**, 126401 (2009).

[26] M. A. Baranov, M. Dalmonte, G. Pupillo, and P. Zoller, *Condensed Matter Theory of Dipolar Quantum Gases*, Chem. Rev. **112**, 5012 (2012).

[27] A. Griesmaier, J. Werner, S. Hensler, J. Stuhler, and T. Pfau, *Bose-Einstein Condensation of Chromium*, Phys. Rev. Lett. **94**, 160401 (2005).

[28] M. Lu, N. Q. Burdick, S. H. Youn, and B. L. Lev, *Strongly Dipolar Bose-Einstein Condensate of Dysprosium*, Phys. Rev. Lett. **107**, 190401 (2011).

[29] K. Aikawa, A. Frisch, M. Mark, S. Baier, A. Rietzler, R. Grimm, and F. Ferlaino, *Bose-Einstein Condensation of Erbium*, Phys. Rev. Lett. **108**, 210401 (2012).

[30] K.-K. Ni, S. Ospelkaus, M. H. G. de Miranda, A. PeÕer, B. Neyenhuis, J. J. Zirbel, S. Kotochigova, P. S. Julienne, D. S. Jin, and J. Ye, *A High Phase-Space-Density Gas of Polar Molecules*, Science **332**, 231 (2008).

[31] C.-H. Wu, J. W. Park, P. Ahmadi, S. Will, and M. W. Zwierlein, *Ultracold Fermionic Feshbach Molecules of $^{23}Na^{40}K$*, Phys. Rev. Lett. **109**, 085301 (2012).

[32] C. Trefzger, C. Menotti, B. Capogrosso-Sansone, and M. Lewenstein, *Ultracold dipolar gases in optical lattices*, J. Phys. B: At. Mol. Opt. Phys. **44**, 193001 (2011).

[33] S. Sinha and L. Santos, *Cold Dipolar Gases in Quasi-One-Dimensional Geometries*, Phys. Rev. Lett. **99**, 140406 (2007).

[34] N. Bartolo, D. J. Papoular, C. Menotti, and A. Recati, *A toy model for the dipolar-induced resonace in quasi-one-dimensional systems*, arXiv:1410:2483 (2014), submitted to EPJ Special Topics, Levico BEC 2014.

[35] N. Bartolo, D. J. Papoular, L. Barbiero, C. Menotti, and A. Recati, *Dipolar-induced resonance for ultracold bosons in a quasi-one-dimensional optical lattice*, Phys. Rev. A **88**, 023603 (2013).

[36] K. S. Novoselov, *Electric Field Effect in Atomically Thin Carbon Films*, Science **306**, 666 (2004).

[37] A. K. Geim and K. S. Novoselov, *The rise of graphene*, Nature Mater. **6**, 183 (2007).

[38] A. H. Castro Neto, F. Guinea, N. M. R. Peres, K. S. Novoselov, and A. K. Geim, *The electronic properties of graphene*, Rev. Mod. Phys. **81**, 109 (2009).

[39] M. Polini, F. Guinea, M. Lewenstein, H. C. Manoharan, and V. Pellegrini, *Artificial honeycomb lattices for electrons, atoms and photons*, Nature Nanotechnol. **8**, 625 (2013).

[40] L. Tarruell, D. Greif, T. Uehlinger, G. Jotzu, and T. Esslinger, *Creating, moving and merging Dirac points with a Fermi gas in a tunable honeycomb lattice*, Nature **483**, 302 (2012).

[41] N. Bartolo and M. Antezza, *Matter waves in atomic artificial graphene*, Europhys. Lett. **107**, 30006 (2014).

[42] N. Bartolo and M. Antezza, *Matter waves in two-dimensional arbitrary atomic crystals*, Phys. Rev. A **90**, 033617 (2014), selected for Phys. Rev. A - Kaleidoscope, Sep. 2014.

[43] G. Lamporesi, J. Catani, G. Barontini, Y. Nishida, M. Inguscio, and F. Minardi, *Scattering in Mixed Dimensions with Ultracold Gases*, Phys. Rev. Lett. **104**, 153202 (2010).

[44] B. Gadway, D. Pertot, J. Reeves, M. Vogt, and D. Schneble, *Glassy Behavior in a Binary Atomic Mixture*, Phys. Rev. Lett. **107**, 145306 (2011).

[45] N. Bartolo and M. Antezza, *Scattering in mixed and reduced dimensions: 0D-2D*, in preparation .

[46] L. de Broglie, *Recherches sur la Théorie des Quanta*, Annales des Physique **10**, III (1925).

[47] F. Schreck, L. Khaykovich, K. L. Corwin, G. Ferrari, T. Bourdel, J. Cubizolles, and C. Salomon, *Quasipure Bose-Einstein Condensate Immersed in a Fermi Sea*, Phys. Rev. Lett. **87**, 080403 (2001).

[48] A. G. Truscott, K. E. Strecker, W. I. McAlexander, and G. B. P. andRandall G. Hulet, *Observation of Fermi Pressure in a Gas of Trapped Atoms*, Science **291**, 2570 (2001).

[49] E. A. Donley, N. R. Claussen, S. L. Cornish, J. L. Roberts, E. A. Cornell, and C. E. Wieman, *Dynamics of collapsing and exploding Bose-Einstein condensates*, Nature **412**, 295 (2001).

[50] J. Bardeen, L. N. Cooper, and J. R. Schrieffer, *Theory of Superconductivity*, Phys. Rev. **108**, 1175 (1957).

[51] L. D. Landau and L. M. Lifshitz, *Quantum Mechanics*, 3rd ed., Vol. 3 (Butterworth-Heinemann, 1976).

[52] H. M. J. M. Boesten, C. C. Tsai, J. R. Gardner, D. J. Heinzen, and B. J. Verhaar, *Observation of a shape resonance in the collision of two cold* ^{87}*Rb atoms*, Phys. Rev. A **55**, 636 (1997).

[53] G. F. Gribakin and V. V. Flambaum, *Calculation of the scattering length in atomic collisions using the semiclassical approximation*, Phys. Rev. A **48**, 546 (1993).

[54] M. Borkowski, P. S. Zuchowski, R. Ciurylo, P. S. Julienne, D. Kędziera, L. Mentel, P. Tecmer, F. Münchow, C. Bruni, and A. Görlitz, *Scattering lengths in isotopologues of the RbYb system*, Phys. Rev. A **88**, 052708 (2013).

[55] H. Feshbach, *Unified theory of nuclear reactions*, Ann. Phys. **5**, 357 (1958).

[56] H. Feshbach, *A Unified and Theory of Nuclear and Reactions. II*, Ann. Phys. **19**, 287 (1962).

[57] U. Fano, *Effects of Configuration and Interaction on Intensities and Phase Shifts*, Phys. Rev. **124**, 1866 (1961).

[58] A. J. Moerdijk, B. J. Verhaar, and A. Axelsson, *Resonances in ultracold collisions of* ^{6}*Li,* ^{7}*Li and* ^{23}*Na*, Phys. Rev. A **51**, 4852 (1995).

[59] S. Inouye, M. R. Andrews, J. Stenger, H.-J. Miesner, D. M. Stamper-Kurn, and W. Ketterle, *Observation of Feshbach resonances in a Bose-Einstein condensate*, Nature **392**, 151 (1998).

[60] P. O. Fedichev, Y. Kagan, G. V. Shlyapnikov, and J. T. M. Walraven, *Influence of Nearly Resonant Light on the Scattering Length in Low-Temperature Atomic Gases*, Phys. Rev. Lett. **77**, 2913 (1996).

[61] M. Theis, G. Thalhammer, K. Winkler, M. Hellwig, G. Ruff, R. Grimm, and J. H. Denschlag, *Tuning the Scattering Length with an Optically Induced Feshbach Resonance*, Phys. Rev. Lett. **93**, 123001 (2004).

[62] J. Dalibard and C. Cohen-Tannoudji, *Laser cooling below the Doppler limit by polarization gradients: simple theoretical models*, J. Opt. Soc. Am. B **6**, 2023 (1989).

[63] P. J. Ungar, D. S. Weiss, E. Riis, and S. Chu, *Optical molasses and multilevel atoms: theory*, J. Opt. Soc. Am. B **6**, 2058 (1989).

[64] P. Verkerk, B. Lounis, C. Salomon, C. Cohen-Tannoudji, J.-Y. Courtois, and G. Grynberg, *Dynamics and Spatial Order of Cold Cesium Atoms in a Periodic Optical Potential*, Phys. Rev. Lett. **68**, 3861 (1992).

[65] P. S. Jessen, C. Gerz, P. D. Lett, D. W. Phillips, S. L. Rolston, R. J. C. Spreeuw, and C. I. Westbrook, *Observation of Quantized Motion of Rb Atoms in an Optical Field*, Phys. Rev. Lett. **69**, 49 (1992).

[66] J. D. Jackson, *Classical Electrodynamics*, 3rd ed. (John Wiley and Sons Inc., 1998).

[67] G. Grynberg and C. Robilliard, *Cold atoms in dissipative optical lattices*, Phys. Rep. **355**, 335 (2001).

[68] W. S. Bakr, A. Peng, M. E. Tai, R. Ma, J. Simon, J. I. Gillen, S. Folling, L. Pollet, and M. Greiner, *Probing the Superfluid-to-Mott Insulator Transition at the Single-Atom Level*, Science **329**, 547 (2010).

[69] F. Nogrette, H. Labuhn, S. Ravets, D. Barredo, L. Béguin, A. Vernier, T. Lahaye, and A. Browaeys, *Single-Atom Trapping in Holographic 2D Arrays of Microtraps with Arbitrary Geometries*, Phys. Rev. X **4**, 021034 (2014).

[70] D. Jaksch, C. Bruder, J. I. Cirac, C. W. Gardiner, and P. Zoller, *Cold Bosonic Atoms in Optical Lattices*, Phys. Rev. Lett. **15**, 3108 (1998).

[71] O. Dutta, M. Gajda, P. Hauke, M. Lewenstein, D.-S. Lühmann, B. A. Malomed, T. Sowiński, and J. Zakrzewski, *Non-standard Hubbard models in optical lattices*, arXiv:1406.0181 (2014).

[72] D. Rossini and R. Fazio, *Phase diagram of the extended Bose-Hubbard and model*, New J. Phys. **14**, 065012 (2012).

[73] E. G. Dalla Torre, E. Berg, and E. Altman, *Hidden Order in 1D Bose Insulators*, Phys. Rev. Lett. **97**, 260401 (2006).

[74] B. Capogrosso-Sansone, C. Trefzger, M. Lewenstein, P. Zoller, and G. Pupillo, *Quantum Phases of Cold Polar Molecules in 2D Optical Lattices*, Phys. Rev. Lett. **104**, 125301 (2010).

[75] D. S. Petrov and G. V. Shlyapnikov, *Interatomic collisions in a tightly confined Bose gas*, Phys. Rev. A **64**, 012706 (2001).

[76] B. Verhaar, L. P. H. de Goey, J. P. H. W. van den Eijnde, and E. J. D. Vredenbregt, *Scattering length and effective range for scattering in a plane and in higher dimensions*, Phys. Rev. A **32**, 1424 (1985).

[77] M. Olshanii and L. Pricoupenko, *Rigorous Approach to the Problem of Ultraviolet Divergencies in Dilute Bose Gases*, Phys. Rev. Lett. **88**, 010402 (2001).

[78] L. Pricoupenko and M. Olshanii, *Stability of two-dimensional Bose gases in the resonant regime*, J. Phys. B: At. Mol. Opt. Phys. **40**, 2065 (2007).

[79] G. Astrakharchik and Y. Lozovik, *Super-Tonks-Girardeau regime in trapped one-dimensional dipolar gases*, Phys. Rev. A **77**, 013404 (2008).

[80] T. Bergeman, M. Moore, and M. Olshanii, *Atom-Atom Scattering under Cylindrical Harmonic Confinement: Numerical and Analytic Studies of the Confinement Induced Resonance*, Phys. Rev. Lett. **91**, 163201 (2003).

[81] E. Haller, M. Gustavsson, M. J. Mark, J. G. Danzl, R. Hart, G. Pupillo, and H.-C. Nagerl, *Realization of an Excited, Strongly Correlated Quantum Gas Phase*, Science **325**, 1224 (2009).

[82] E. Haller, M. J. Mark, R. Hart, J. G. Danzl, L. Reichsöllner, V. Melezhik, P. Schmelcher, and H.-C. Nägerl, *Confinement-Induced Resonances in Low-Dimensional Quantum Systems*, Phys. Rev. Lett. **104**, 153203 (2010).

[83] J. Catani, G. Barontini, G. Lamporesi, F. Rabatti, G. Thalhammer, F. Minardi, S. Stringari, and M. Inguscio, *Entropy Exchange in a Mixture of Ultracold Atoms*, Phys. Rev. Lett. **103**, 140401 (2009).

[84] Y. Nishida and S. Tan, *Universal Fermi Gases in Mixed Dimensions*, Phys. Rev. Lett. **101**, 170401 (2008).

[85] Y. Nishida and S. Tan, *Confinement-induced p-wave resonances from s-wave interactions*, Phys. Rev. A **82**, 062713 (2010).

[86] M. Fattori, G. Roati, B. Deissler, C. D'Errico, M. Zaccanti, M. Jona-Lasinio, L. Santos, M. Inguscio, and G. Modugno, *Magnetic Dipolar Interaction in a Bose-Einstein Condensate Atomic Interferometer*, Phys. Rev. Lett. **101**, 190405 (2008).

[87] S. Giovanazzi, A. Görlitz, and T. Pfau, *Tuning the Dipolar Interaction in Quantum Gases*, Phys. Rev. Lett. **89**, 130401 (2002).

[88] J. Stuhler, A. Griesmaier, T. Koch, M. Fattori, T. Pfau, S. Giovanazzi, P. Pedri, and L. Santos, *Observation of Dipole-Dipole Interaction in a Degenerate Quantum Gas*, Phys. Rev. Lett. **95**, 150406 (2005).

[89] M. R. Andrews, C. G. Townsend, H.-J. Miesner, D. S. Durfee, D. M. Kurn, and W. Ketterle, *Observation of Interference Between Two Bose Condensates*, Science **275**, 637 (1997).

[90] S. Ronen, D. Bortolotti, and J. Bohn, *Radial and Angular Rotons in Trapped Dipolar Gases*, Phys. Rev. Lett. **98**, 030406 (2007).

[91] T. Koch, T. Lahaye, and J. Metz, *Stabilizing a purely dipolar quantum gas against collapse*, Nat. Phys. **4**, 218 (2008).

[92] T. Lahaye, J. Metz, B. Fröhlich, T. Koch, M. Meister, A. Griesmaier, T. Pfau, H. Saito, Y. Kawaguchi, and M. Ueda, *d-Wave Collapse and Explosion of a Dipolar Bose-Einstein Condensate*, Phys. Rev. Lett. **101**, 080401 (2008).

[93] K. Aikawa, S. Baier, A. Frisch, M. Mark, C. Ravensbergen, and F. Ferlaino, *Observation of Fermi surface deformation in a dipolar quantum gas*, Science **345**, 1484 (2014).

[94] B. Pasquiou, G. Bismut, E. Maréchal, P. Pedri, L. Vernac, O. Gorceix, and B. Laburthe-Tolra, *Spin Relaxation and Band Excitation of a Dipolar Bose-Einstein Condensate in 2D Optical Lattices*, Phys. Rev. Lett. **106**, 015301 (2011).

[95] A. Chotia, B. Neyenhuis, S. A. Moses, B. Yan, J. P. Covey, M. Foss-Feig, A. M. Rey, D. S. Jin, and J. Ye, *Long-Lived Dipolar Molecules and Feshbach Molecules in a 3D Optical Lattice*, Phys. Rev. Lett. **108**, 080405 (2012).

[96] B. Yan, S. A. Moses, B. Gadway, J. P. Covey, K. R. A. Hazzard, A. M. Rey, D. S. Jin, and J. Ye, *Observation of dipolar spin-exchange interactions with lattice-confined polar molecules*, Nature **501**, 521 (2013).

[97] A. Maluckov, G. Gligorić G., L. Hadžievski, B. A. Malomed, and T. Pfau, *Stable Periodic Density Waves in Dipolar Bose-Einstein Condensates Trapped in Optical Lattices*, Phys. Rev. Lett. **108**, 140402 (2012).

[98] M. Marinescu and L. You, *Controlling Atom-Atom Interaction at Ultralow Temperatures by dc Electric Fields*, Phys. Rev. Lett. **81**, 4596 (1998).

[99] P. Giannakeas, V. S. Melezhik, and P. Schmelcher, *Dipolar Confinement-Induced Resonances of Ultracold Gases in Waveguides*, Phys. Rev. Lett. **111**, 183201 (2013).

[100] F. Deuretzbacher, J. C. Cremon, and S. M. Reimann, *Ground-state properties of few dipolar bosons in a quasi-one-dimensional harmonic trap*, Phys. Rev. A **81**, 063616 (2010), **87**, 039903(E) (2013).

[101] B. E. Granger and D. Blume, *Tuning the Interactions of Spin-Polarized Fermions Using Quasi-One-Dimensional Confinement*, Phys. Rev. Lett. **92**, 133202 (2004).

[102] D. S. Petrov, G. V. Shlyapnikov, and J. T. M. Walraven, *Regimes of Quantum Degeneracy in Trapped 1D Gases*, Phys. Rev. Lett. **85**, 3745 (2000).

[103] M. Girardeau, *Relationship between Systems of Impenetrable Bosons and Fermions in One Dimension*, J. Math. Phys. **1**, 516 (1960).

[104] G. E. Astrakharchik, D. Blume, S. Giorgini, and B. E. Granger, *Quasi-One-Dimensional Bose Gases with a Large Scattering Length*, Phys. Rev. Lett. **92**, 030402 (2004).

[105] G. E. Astrakharchik, J. Boronat, J. Casulleras, and S. Giorgini, *Beyond the Tonks-Girardeau Gas: Strongly Correlated Regime in Quasi-One-Dimensional Bose Gases*, Phys. Rev. Lett. **95**, 190407 (2005).

[106] T. Busch, B.-G. Englert, K. Rzazewski, and M. Wilkens, *Two Cold Atoms in a Harmonic Trap*, Found. Phys. **28**, 549 (1998).

[107] J. Hecker-Denschlag, J. E. Simsarian, H. Häffner, C. McKenzie, A. Browaeys, D. Cho, K. Helmerson, S. L. Rolston, and W. D. Phillips, *A Bose-Einstein condensate in an optical lattice*, J. Phys. B: At. Mol. Opt. Phys. **35**, 3095 (2002).

[108] F. Gerbier, A. Widera, S. Fölling, O. Mandel, T. Gericke, and I. Bloch, *Interference pattern and visibility of a Mott insulator*, Phys. Rev. A **72**, 053606 (2005), we point out a typo in the formula for t/E_r in footnote 2, where the factor (a/λ_L) should not be present.

[109] F. J. Burnell, M. M. Parish, N. R. Cooper, and S. L. Sondhi, *Devil's staircases and supersolids in a one-dimensional dipolar Bose gas*, Phys. Rev. B **80**, 174519 (2009).

[110] M. Endres, M. Cheneau, T. Fukuhara, C. Weitenberg, P. Schauss, C. Gross, L. Mazza, M. C. Bañuls, L. Pollet, I. Bloch, and et al., *Observation of Correlated Particle-Hole Pairs and String Order in Low-Dimensional Mott Insulators*, Science **334**, 200 (2011).

[111] G. Astrakharchik, G. Morigi, G. De Chiara, and J. Boronat, *Ground state of low-dimensional dipolar gases: Linear and zigzag chains*, Phys. Rev. A **78**, 063622 (2008).

[112] S. Greschner, L. Santos, and T. Vekua, *Ultracold bosons in zig-zag optical lattices*, Phys. Rev. A **87**, 033609 (2013).

[113] S. Gammelmark and N. T. Zinner, *Dipoles on a two-leg ladder*, Phys. Rev. B **88**, 245135 (2013).

[114] X. Deng, R. Citro, E. Orignac, A. Minguzzi, and L. Santos, *Polar bosons in one-dimensional disordered optical lattices*, Phys. Rev. B **87**, 195101 (2013).

[115] M. Larcher, C. Menotti, B. Tanatar, and P. Vignolo, *Metal-insulator transition induced by random dipoles*, Phys. Rev. A **88**, 013632 (2013).

[116] F. Deuretzbacher, G. M. Bruun, C. J. Pethick, M. Jona-Lasinio, S. M. Reimann, and L. Santos, *Self-bound many-body states of quasi-one-dimensional dipolar Fermi gases: Exploiting Bose-Fermi mappings for generalized contact interactions*, Phys. Rev. A **88**, 033611 (2013).

[117] S. Ejima and S. Nishimoto, *Phase Diagram of the One-Dimensional Half-Filled Extended Hubbard Model*, Phys. Rev. Lett. **99**, 216403 (2007).

[118] M. Nakamura, *Tricritical behavior in the extended Hubbard chains*, Phys. Rev. B **61**, 16377 (2000).

[119] S. G. Bhongale, L. Mathey, S.-W. Tsai, C. W. Clark, and E. Zhao, *Bond Order Solid of Two-Dimensional Dipolar Fermions*, Phys. Rev. Lett. **108**, 145301 (2012).

[120] M. D. Dio, L. Barbiero, A. Recati, and M. Dalmonte, *Spontaneous Peierls dimerization and emergent bond order in one-dimensional dipolar gases*, arXiv:1304.5200 .

[121] P. Vignolo, A. Z., and M. P. Tosi, *The transmittivity of a Bose-Einstein condensate on a lattice: interference from period doubling and the effect of disorder*, J. Phys. B: At. Mol. Opt. Phys. **36**, 4535 (2003).

[122] U. Gavish and Y. Castin, *Matter-Wave Localization in Disordered Cold Atom Lattices*, Phys. Rev. Lett. **95**, 020401 (2005).

[123] J.-F. Schaff, Z. Akdeniz, and P. Vignolo, *Localization-delocalization transition in the random dimer model*, Phys. Rev. A **81**, 041604 (2010).

[124] M. Antezza, Y. Castin, and D. A. W. Hutchinson, *Quantitative study of two- and three-dimensional strong localization of matter waves by atomic scatterers*, Phys. Rev. A **82**, 043602 (2010), we point out a misprint in Eq. (47), where the factor 8 is missing in front of δ^2.

[125] Z.-Y. Shi, R. Qi, and H. Zhai, *s-wave-scattering resonances induced by dipolar interactions of polar molecules*, Phys. Rev. A **85**, 020702(R) (2012).

[126] I. Carusotto, M. Antezza, F. Bariani, S. De Liberato, and C. Ciuti, *Optical properties of atomic Mott insulators: From slow light to dynamical Casimir effects*, Phys. Rev. A **77**, 063621 (2008).

[127] M. Antezza and Y. Castin, *Spectrum of Light in a Quantum Fluctuating Periodic Structure*, Phys. Rev. Lett. **103**, 123903 (2009).

[128] M. Antezza and Y. Castin, *Fano-Hopfield model and photonic band gaps for an arbitrary atomic lattice*, Phys. Rev. A **80**, 013816 (2009).

[129] M. Antezza and Y. Castin, *Photonic band gap in an imperfect atomic diamond lattice: Penetration depth and effects of finite size and vacancies*, Phys. Rev. A **88**, 033844 (2013).

[130] A. Singha, M. Gibertini, B. Karmakar, S. Yuan, M. Polini, G. Vignale, M. I. Katsnelson, A. Pinczuk, L. N. Pfeiffer, K. W. West, and et al., *Two-Dimensional Mott-Hubbard Electrons in an Artificial Honeycomb Lattice*, Science **332**, 1176 (2011).

[131] T. Jacqmin, I. Carusotto, I. Sagnes, M. Abbarchi, D. D. Solnyshkov, G. Malpuech, E. Galopin, A. Lemaître, J. Bloch, and A. Amo, *Direct Observation of Dirac Cones and a Flatband in a Honeycomb Lattice for Polaritons*, Phys. Rev. Lett. **112**, 116402 (2014).

[132] K. K. Gomes, W. Mar, W. Ko, F. Guinea, and H. C. Manoharan, *Designer Dirac fermions and topological phases in molecular graphene*, Nature **483**, 306 (2012).

[133] M. Bellec, U. Kuhl, G. Montambaux, and F. Mortessagne, *Topological Transition of Dirac Points in a Microwave Experiment*, Phys. Rev. Lett. **110**, 033902 (2013).

[134] S.-L. Zhu, B. Wang, and L.-M. Duan, *Simulation and Detection of Dirac Fermions with Cold Atoms in an Optical Lattice*, Phys. Rev. Lett. **98**, 260402 (2007).

[135] P. Dietl, F. Piéchon, and G. Montambaux, *New Magnetic Field Dependence of Landau Levels in a Graphenelike Structure*, Phys. Rev. Lett. **100**, 236405 (2008).

[136] L.-K. Lim, J.-N. Fuchs, and G. Montambaux, *Bloch-Zener Oscillations across a Merging Transition of Dirac Points*, Phys. Rev. Lett. **108**, 175303 (2012).

[137] C. Wu, D. Bergman, L. Balents, and S. Das Sarma, *Flat Bands and Wigner Crystallization in the Honeycomb Optical Lattice*, Phys. Rev. Lett. **99**, 070401 (2007).

[138] C. Wu and S. Das Sarma, *$p_{x,y}$-orbital counterpart of graphene: Cold atoms in the honeycomb optical lattice*, Phys. Rev. B **77**, 235107 (2008).

[139] L. Santos, M. A. Baranov, J. I. Cirac, H.-U. Everts, H. Fehrmann, and M. Lewenstein, *Atomic Quantum Gases in Kagomé Lattices*, Phys. Rev. Lett. **93**, 030601 (2004).

[140] G.-B. Jo, J. Guzman, C. K. Thomas, P. Hosur, A. Vishwanath, and D. M. Stamper-Kurn, *Ultracold Atoms in a Tunable Optical Kagome Lattice*, Phys. Rev. Lett. **108**, 045305 (2012).

[141] D. S. Petrov, G. E. Astrakharchik, D. J. Papoular, C. Salomon, and G. V. Shlyapnikov, *Crystalline Phase of Strongly Interacting Fermi Mixtures*, Phys. Rev. Lett. **99**, 130407 (2007).

[142] Z. Lan and C. Lobo, *Optical lattices with large scattering length: Using few-body physics to simulate an electron-phonon system*, Phys. Rev. A **90**, 033627 (2014).

[143] K. Góral and L. Santos, *Ground state and elementary excitations of single and binary Bose-Einstein condensates of trapped dipolar gases*, Phys. Rev. A **66**, 023613 (2002).